Università degli Studi di Napoli Federico II
Ph.D. Program in
Information Technology and Electrical Engineering
XXXV Cycle

Thesis for the Degree of Doctor of Philosophy

Advanced Target Localization Strategies for Multiplatform Radar Systems via Constrained Optimization

by
Angela Marino

Supervisor: Prof. Augusto Aubry

Co-supervisor: Dr. Paolo Braca
NATO Centre for Maritime Research & Experimentation

Scuola Politecnica e delle Scienze di Base
Dipartimento di Ingegneria Elettrica e delle Tecnologie dell'Informazione

To my family

Advanced Target Localization Strategies for Multiplatform Radar Systems via Constrained Optimization

Ph.D. Thesis presented
for the fulfillment of the Degree of Doctor of Philosophy
in Information Technology and Electrical Engineering
by

Angela Marino

October 2022

Approved as to style and content by

Prof. Augusto Aubry, Supervisor

Dr. Paolo Braca, Co-supervisor
NATO Centre for Maritime Research & Experimentation

Università degli Studi di Napoli Federico II
Ph.D. Program in Information Technology and Electrical Engineering
XXXV cycle - Chairman: Prof. Stefano Russo

itee PhD
enformation technology
electrical engineering

http://itee.dieti.unina.it

Candidate's declaration

I hereby declare that this thesis submitted to obtain the academic degree of Philosophiæ Doctor (Ph.D.) in Information Technology and Electrical Engineering is my own unaided work, that I have not used other than the sources indicated, and that all direct and indirect sources are acknowledged as references.
Parts of this dissertation have been published in international journals and/or conference articles (see list of the author's publications at the end of the thesis).

Napoli, December 20, 2022

____

Angela Marino

Abstract

Nowadays, the ability to locate targets is crucial for a huge number of applications which demand an ever increasing accuracy. For this reason, the design of advanced sensing systems has attracted a lot of attention in both academic and industrial contexts.

The main aim of this thesis is the development of innovative localization algorithms for some sensing systems of practical relevance. Specifically, three novel techniques have been devised.

The first strategy, referred to as Angular and Active Constrained Least Square (AACLS), is an algorithm for 2D Passive Bistatic Radar (PBR) localization via joint exploitation of multiple illuminators of opportunity and measurements gathered by a co-located active radar, thus representing a basic version of a Multiplatform Radar Network (MPRN). This technique exploits angular and range constraints resulting from prior knowledge of the PBR beam extent and uncertainty of active radar data.

The second algorithm, denoted as Angular and Range Constrained Estimator (ARCE), is a 3D localization technique for MPRNs, comprising one transmitter and multiple receivers. In particular, ARCE leverages ad-hoc constraints in order to capitalize on the information embedded into the monostatic sensor radiation pattern features.

The third technique is obtained combining ARCE and the Sum-Product Algorithm (SPA)-based Multitarget Tracking (MTT) technique. Specifically, the latter is enhanced through a bespoke particles generation process exploiting the ARCE position estimate.

Keywords: Multiplatform Radar Network (MPRN), Active Radar, Passive Bistatic Radar (PBR), Bistatic and Monostatic Measurements, Constrained Least Squares Estimation, Non-Convex Optimization.

Sintesi in lingua italiana

Al giorno d'oggi, la capacità di localizzare bersagli è fondamentale per un gran numero di applicazioni, le quali richiedono un'accuratezza sempre maggiore. Per questo motivo, la progettazione di sistemi di *sensing* avanzati ha attirato molta attenzione in ambito sia accademico sia industriale.

Questa tesi tratta lo sviluppo di algoritmi di localizzazione innovativi per alcuni sistemi di *sensing* di notevole rilevanza. In particolare, si propongono tre nuove stragie per il posizionamento dei bersagli.

La prima strategia, denominata Angular and Active Constrained Least Square (AACLS), è un algoritmo per la localizzazione 2D in sistemi radar passivi bistatici che sfruttino le misure ottenute da molteplici trasmettitori d'opportunità e un radar attivo co-locato, rappresentando così una versione base di un sistema multipiattaforma. Questa tecnica porta in conto i vincoli angolari e di range che derivano dalla conoscenza dell'estensione del fascio del radar passivo bistatico e dall'incertezza dei dati del radar attivo.

La seconda tecnica, denominata Angular and Range Constrained Estimator (ARCE), consiste in un algoritmo per la localizzazione 3D in sistemi multipiattaforma, comprendenti un trasmettitore e più ricevitori (di cui uno co-locato con il trasmettitore). Attraverso ARCE, il processo di localizzazione è in grado di capitalizzare le informazioni derivanti dalle caratteristiche del diagramma di radiazione del sensore monostatico.

Il terzo algoritmo è ottenuto combinando ARCE e la tecnica Multitarget Tracking (MTT) basata su Sum-Product Algorithm (SPA). Precisamente, quest'ultima viene potenziata attraverso un processo di generazione di particles *ad hoc* che sfrutta la stima della posizione fornita da ARCE a partire dalle misure associate ad uno specifico bersaglio.

Parole chiave: Rete Radar Multipiattaforma, Radar Attivo, Radar Passivo Bistatico, Misure Bistatiche e Monostatiche, Stima dei Minimi Quadrati Vincolata, Ottimizzazione Non-Convessa.

Contents

Acknowledgements

Angela Marino's work has been supported by the NATO Science and Technology Organization Centre for Maritime Research and Experimentation (CMRE). Part of the work of this thesis has been carried out in a research period at NATO CMRE in La Spezia, Italy, from July to December 2021.

List of Acronyms

The following acronyms are used throughout the thesis.

AACLS Angular and Active Constrained Least Square

ACLS Angular Constrained Least Square

AOA Angle Of Arrival

ARCE Angular and Range Constrained Estimator

CMRE Centre for Maritime Research and Experimentation

CRLB Cramer Rao Lower Bound

DMPAR Deployable Multiband Passive/Active Radar

FDOA Frequency Difference Of Arrival

FOA Frequency Of Arrival

GOSPA Generalized Optimal Sub-Pattern Assignment

ICBMs Intercontinental Ballistic Missiles

KKT Karush-Kuhn-Tucker

LS Least Squares

MGOSPA	Mean GOSPA
MIMO	Multi-Input Multi-Output
ML	Maximum Likelihood
MOU	Measurement-Origin Uncertainty
MPRN	Multiplatform Radar Network
MTT	Multitarget Tracking
PBR	Passive Bistatic Radar
RAMSE	Root Average MSA
RCRLB	Root Cramer Rao Lower Bound
RF	Radio Frequency
RMSE	Root Mean Square Error
ROCE	Range-Only Constrained Estimator
RSS	Received Signal Strength
SI	Spherical Interpolation
SINR	Signal-to-Interference-plus-Noise Ratio
SNR	Signal to Noise Ratio
SPA	Sum-Product Algorithm
SX	Spherical Intersection
TDOA	Time Difference Of Arrival
TOA	Time Of Arrival

TSE	Two-Step Estimation
WLS	Weighted Least Squares

List of Figures

List of Tables

List of Symbols and Notations

The following symbols are used within the thesis.

$\bar{\phi}$	Half-side antenna beamwidth in the $x - z$ plane
$\bar{\theta}$	Half-side antenna beamwidth in the $x - y$ plane
$\boldsymbol{p}$	Target position
$\boldsymbol{p}_{r_0}$	Radar position
$\boldsymbol{p}_{r_i}$	i-th receiver position
$\boldsymbol{p}_{t_i}$	i-th transmitter position
$\mathcal{P}$	Problem
ϵ	Desired accuracy level
ϵ_0	Maximum size of the initial bisection search interval
$\hat{\boldsymbol{p}}$	Estimated target position
$\hat{\theta}^a$	Target azimuth estimate computed by the active radar
$\hat{R}^a$	Target range estimate computed by the active radar
ϕ_p	Elevation angle of the target

ρ_θ^a	Uncertainty on target azimuth estimate computed by the active radar
ρ_R^a	Uncertainty on target range estimate computed by the active radar
σ_i^2	variance of the i-th statistically independent zero-mean random variable
σ_θ^a	Standard deviation of the active radar estimation error in azimuth
σ_R^a	Standard deviations of the active radar estimation error in range
τ_i	i-th noisy delay measurement
θ_p	Azimuth angle of the target
$\tilde{\tau}_i$	i-th noise-free delay measurement
B	Frequency bandwidth of the transmitted signal
c	Speed of light in a vacuum
c_θ	Azimuth accuracy degradation factor
c_R	Range accuracy degradation factor
n_i	i-th statistically independent zero-mean random variable
λ	Eigenvalue
ω	Angular absolute value velocity
θ	Radar pointing direction
θ^p	PBR pointing direction
L_i	i-th baseline
n	Number of bisection iterations

t	Time
v	Range absolute value velocity

Notations

The following notations are adopted in the thesis.

Vectors and matrices are in boldface, respectively lower case ($\boldsymbol{a}$) and upper case ($\boldsymbol{A}$).

The n-th element of $\boldsymbol{a}$ and the (m, n)-th entry of $\boldsymbol{A}$ are denoted by a_n and $\boldsymbol{A}_{m,n}$, respectively.

The symbol $(\cdot)^T$ indicates the transpose operator.

$\lceil \cdot \rceil$ denotes the operation of rounding up to the nearest integer.

$\boldsymbol{A}^\dagger$ represents the Moore-Penrose inverse of the matrix $\boldsymbol{A}$.

$\boldsymbol{I}$ and $\mathbf{0}$ denote, respectively, the identity matrix and the matrix with zero entries (their size is determined from the context).

$\mathbf{1}_N$ and $\mathbf{0}_N$ are N-length vectors of ones and zeros, respectively.

$\mathbb{R}^N$, $\mathbb{R}^{N,M}$, and $\mathbb{S}^N$ are, respectively, the sets of N-dimensional vectors of real numbers, of $N \times M$ real matrices, and of $N \times N$ symmetric matrices.

$\mathbf{diag}\,(\boldsymbol{a})$ indicates the diagonal matrix whose i-th diagonal element is the i-th entry of $\boldsymbol{a}$.

The symbol $\succeq$ (and its strict form $\succ$) is used to indicate generalized matrix inequality: for any $\boldsymbol{A} \in \mathbb{S}^N$, $\boldsymbol{A} \succeq \mathbf{0}$ means that $\boldsymbol{A}$ is a positive semi-definite matrix ($\boldsymbol{A} \succ \mathbf{0}$ for positive definiteness).

$\lambda_1(\boldsymbol{X}), \ldots, \lambda_N(\boldsymbol{X})$, with $\lambda_1(\boldsymbol{X}) \geq \ldots \geq \lambda_N(\boldsymbol{X})$, denote the eigenvalues of $\boldsymbol{X} \in \mathbb{S}^N$, arranged in decreasing order.

Given $\boldsymbol{B} \succ \boldsymbol{0}$ and $\boldsymbol{A} \in \mathbb{S}^N$, the generalized eigenvalues of the matrix pair $(\boldsymbol{A}, \boldsymbol{B})$ are given by $\lambda_i(\boldsymbol{A}, \boldsymbol{B}) = \lambda_i(\boldsymbol{B}^{-1/2}\boldsymbol{A}\boldsymbol{B}^{-1/2})$, $i = 1, \dots, N$. The Euclidean norm of the vector $\boldsymbol{x} \in \mathbb{R}^N$ is denoted as $\|\boldsymbol{x}\|$.

Chapter 1

Introduction

Localization is defined as the process of estimating the position of a target or multiple targets, including aircrafts, missiles, lost humans, protected wildlife, users of location-based services, just to list a few. Specifically, the basic idea of localization is to exploit the characteristics of the signals captured by the receivers to determine the position of an object that emits or reflects such signals.

Localization is essential for a wide range of applications, including autonomous vehicles [1], industrial/environmental surveillance and control [2], public safety [3], as well as assistive healthcare [4] and social networks [5]. Emergency response is one of the most significant applications for localization. Indeed, during emergencies like building fires, real-time location estimations of trapped occupants (and first responders) are needed when planning the search and rescue routes. The success of these applications clearly depends on the precision and reliability in positioning the target of interest; consequently, many efforts have been devoted to the development of strategies and techniques capable of improving localization accuracy.

In general, target localization can be accomplished following two different paradigms: direct positioning and two-step positioning [6]. In direct positioning, the overall received signals are jointly processed, so as to exploit all the available information regarding the unknown position in order to determine it. In the two-step positioning scheme, the first stage is designed for extracting position-related parameters;

then, these measurements are usually sent to a central fusion node, which jointly process them, and a specific data fusion localization algorithm is employed to determine the target location.

This thesis focuses on the latter paradigm, which is of great interest; indeed, the two-step scheme can have a significantly lower complexity than the direct approach due to decreased storage and communication requirements [7], while the performance of the two methods is usually quite close for sufficiently high Signal to Noise Ratio (SNR) value and/or signal bandwidths [8]. Furthermore, it is remarkably less costly to send to a central unit the position-related parameters estimates rather than the entire received signals.

Notably, there are many types of location-related measurements. Among them, it is worth mentioning time-based information such as Time Of Arrival (TOA) [9, 10] and Time Difference Of Arrival (TDOA) [11, 12], amplitude-based information, i.e., Received Signal Strength (RSS) [13], spatial-based information, i.e., Angle Of Arrival (AOA) [14], frequency-based information, i.e., Frequency Difference Of Arrival (FDOA) [15], or a combination of them [16–18]. All the (possible heterogeneous) measurements collected by the available sensors are then jointly processed to find target position.

TOA refers to the time instant at which the transmitted signal impinges on the receiver. TOA-based localization algorithms require the receiving sensors and transmitter to be synchronized, usually by sharing the same reference clock; moreover, the receivers know the start transmission time of the transmitter. Note that such a type of measurements can be performed exploiting signals of different nature, including Radio Frequency (RF), acoustic, infrared, and ultrasound. However, in many applications the synchronization requirement cannot be satisfied. Thus, without knowing the actual signal transmission time at the transmitter, the receiver is unable to determine the signal propagation time. One way to tackle this problem and duly address target localization is to exploit TDOA measurements. TDOA is the difference between the arrival time of the transmitted signal to a receiver and that to a reference node. In order to obtain the TDOA at a specific station, one method is to first estimate the TOAs at the station and at the reference node and then subtract one from the other. This approach requires an accurate knowledge of the transmitted signal by the receivers. In practice, the most commonly used method is to apply the generalized cross-correlation between the signal collected by the receiver of interest and the signal received at the reference node. The location of the peak of the cross-correlation function gives the TDOA estimate. Noteworthy, this approach just requires synchronization among receivers.

RSS is a measure of the power of the detected radio signal at a receiver. Target localization exploiting this type of measurements can be classified in two categories: map-based and model-based strategies [19]. The former consists in building a database of RSS measurements associated with their corresponding locations. When a target has to be localized, the RSS measurements collected from the receivers are matched against the ones stored in the map, in order to find the closest correspondence. Map-based algorithms require a burdensome data collection phase where a large number of signal strength measurements must be recorded along with the corresponding locations. Model-based techniques, instead, aim at establishing a mathematical model capturing the variation of the RSS as a function of the distance, thus requiring knowledge of the transmitted signal's power.

As to AOA information, it provides knowledge about the line connecting the source and the receiver, with respect to a reference system. AOA is measured via antenna arrays or scanning antenna. AOA estimation via antenna arrays (for which the geometry is assumed known) determines, in general, the angles information analyzing the differences in signal arrival times at different antenna elements. Alternatively, AOA estimate (for a two dimensional sensing scenario) can be obtained through scanning antenna exploiting the centroid method.

If there is relative motion between the receivers and the target, the differences in received Doppler frequency shifts can be used for target localization. This type of measurement is named FDOA and is mostly used together with TDOA. However, if the bandwidths of the received signals are very narrow, TDOA accuracy is relatively low [20]. In such cases, localization techniques relying only on FDOA can be exploited. The cross ambiguity function approach is usually employed to measure TDOA and FDOA.

Before proceeding further, it is worth pointing out that, from a practical point of view, it is very important to account for the trade-off between localization accuracy and computational demand as well as cost, for the selection of the appropriate sensing system. For example, the localization systems based on TOA or TDOA provide high estimation accuracy, but require timing and synchronization thus making the localization cost-expensive [21]. As to RSS-based methods, they demand very low-cost (possibly inexpensive) hardware and less processing and communication resources [22], thus making them attractive low-cost solutions to accomplish localization. Nonetheless, they usually provide worse localization accuracy than alternatives. AOA localization does not require time synchronization, but it demands extra hardware at the receiver to estimate angles [22] and its positioning accuracy is generally worse than that provided by TOA or TDOA. Finally, FDOA requires a quite demanding measurement process and the achievable precision is generally lower than TDOA-based strategies. However, FDOAs information can improve localization performance when used in combination with other type of measurements and it can be used alone profitably for narrow bandwidth signals [23].

Noteworthy, most of the localization systems are based on range-related measurements and, for this reason, this thesis focuses on such systems. In the following a brief description on some sensing architectures and processing strategies relying on range measurements to accomplish the localization task is provided.

Overview of the localization techniques relying on range-related measurements. The most well known localization systems based on range-related measurements are the active radar and the Passive Bistatic Radar (PBR). Active radars [24] require transmitters which emit bespoke signals. Their standard implementation relies on a receiver that is co-located with the transmitter (monostatic radar) and gather the environment echo in order to detect and localize targets. In this respect, note that monostatic radars also exploit beam pointing direction to position the target. PBR [25, 26], also known as "Green Radar" [27], uses bistatic target range measurements obtained collecting the target echoes resulting from the signals transmitted by multiple illuminators of opportunity [28] [[29], Chap. 11]. To this end, PBR receivers are equipped with two receiving channels per transmitter to acquire both the signal transmitted by the emitter and the signal backscattered by the target. Then, leveraging these measurements the target localization process determines an ellipsoid (ellipse in a 2D geometry) for each illuminator-receiver pair and, substantially, the intersection of multiple ellipsoids identifies the target position [28, 30]. As a result, the PBR problem falls within the elliptical class [31–33]. Some interesting and technically sound localization algorithms for PBR can be found in [29, 34–36].

In the last decades, due to technology advances and new requirements in terms of performance and operating environments, great interest has been focused on the development of novel and more advanced networks, able to achieve better accuracy and reliability than monostatic and bistatic radars. In this context, MPRNs (see Fig. 1.1) are envisioned as next-generation sensing systems [37]. Among them, hybrid active-passive systems assume an important role and have been extensively addressed in the scientific panorama [38]. Indeed, combining passive and active radars in various deployment configurations can provide geometric, signal, and scattering diversity to reach an enhanced situation awareness [39, 40].

Target localization via the joint use of passive/active radars is of particular interest for instance in the case of harbour surveillance where an active rotating radar is complemented with a PBR. In fact, the antenna scanning velocity is typically about 6 seconds per rotation, and it could be necessary to employ the PBR for acquiring further measurements and correctly localize fast possibly manoeuvring threats targets.

In [39, 41–44] some attempts to exploit PBR capitalizing information gathered by an active radar have been pursued to boost detection and localization capabilities.

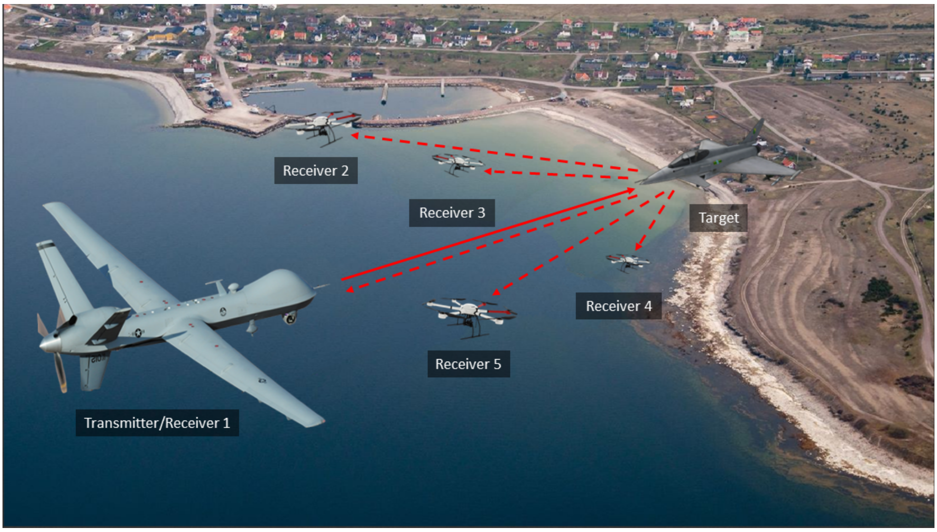

Figure 1.1. A MPRN with one transmitting-receiving node and four receiving nodes.

Specifically, reference [39] addresses the exploitation of active and passive radars that are present in the surveillance area aimed at maximizing the Signal-to-Interference-plus-Noise Ratio (SINR). Reference [41], instead, focuses on the implications of having different surveillance system configurations, i.e., co-located or dislocated passive and active radars, also in terms of sensors infrastructure survivability.

In [42], a hybrid active-passive radar network for Air Defense employing decentralized data fusion processing is introduced, i.e., the Deployable Multiband Passive/Active Radar (DMPAR). The effectiveness of DMPAR systems is assessed in [43, 44] for co-located and distributed net of sensors and proved via experimental results. Remarkably, these studies show that performance improvement and robustness with respect to the stand-alone system using only the passive or the active radar can be achieved via the hybrid active-passive radar system.

More applied research in the context of hybrid passive/active sensing is conducted by NATO SET-242 RTG and SET-258 [45] where the focus is on deployment and assessment in military scenarios of ground based multiband passive/active radars [46].

MPRNs which are currently attracting even higher interest are systems employing a constellation of multiple deployable platforms. Such systems allow to enlarge the surveillance area, to improve data reliability and accuracy, and endow a better resistance to electronic countermeasures [47]. Furthermore, such multistatic configurations reduce effects of shadowing and, exploiting spatial diversity, improve target detectability, especially against low-observable and stealth targets [48, 49].

Finally, a great advantage of MPRNs relies on the possibility for the units to collaborate and change their configuration dynamically [50].

Target localization with a multistatic radar is addressed in [51], where two methods for calculating the Cartesian positions are presented resorting to Spherical Interpolation (SI) and Spherical Intersection (SX). A localization scheme exploiting both TOA from the transmitter to a specific receiver and AOA is proposed in [52], that applies the Weighted Least Squares (WLS) method to estimate the target location and shows that the RMSE decreases as the number of multistatic radar receivers increases under the assumption of Gaussian measurement errors.

An improved method for moving target localization with a noncoherent Multi-Input Multi-Output (MIMO) radar system having widely separated antennas is proposed in [53]. Specifically, the proposed method is based on the Two-Stage WLS, and a closed-form solution is derived [53]. In [54], for the same problem of moving target localization, the authors propose two methods, in which the parameters used are a combination of AOA, Frequency Of Arrival (FOA), and TOA.

Contributions and Dissertation Outline. This thesis deals with the design of innovative range-based localization algorithms for some sensing systems of practical interest. The thesis contribution is threefold.

The first contribution concerns a novel approach for elliptic localization in a PBR aided with side-information provided by an active radar, thus representing a basic version of MPRN. Precisely, angular and range constraints are forced on the target position to capitalize target state gleaned by the active radar and the *a priori* knowledge of the PBR main-beam width size. The positioning problem is formulated as a constrained Least Squares (LS) estimation. The resulting non-convex optimization is solved in closed-form, exploiting a smart partition of the feasible set as well as the regularity of its points. At the analysis stage, some illustrative case studies are provided to show the effectiveness of the developed localization method, referred to as AACLS, also in comparison with some counterparts available in the open literature. The proposed algorithm is tested in a dynamic scenario where the target of interest is approaching the surveillance system, so as to further highlight the accuracy improvement provided by AACLS with respect to alternatives.

The second contribution is an innovative approach for 3D localization in MPRNs comprising one transmitter and multiple receivers. The monostatic radiation pattern features have been wisely exploited in the positioning process restricting the angular location of any illuminated target. Therefore, the localization is cast as a non-convex optimization problem and a quasi-closed-form global optimal solution is computed by means of an *ad hoc* partition of the feasible set. The proposed localization method, indicated as ARCE, is tested in different illustrative examples and is proved to ensure interesting accuracy gains over some counterparts.

Last, a localization-enhanced MTT technique for MPRNs is proposed, which capitalizes past information via a sequential estimation process, often referred to as filtering, and manages missed detections, false alarms, and Measurement-Origin Uncertainty (MOU). This algorithm is obtained through a combination of ARCE with a MTT method based on the SPA [55, 56]. Precisely, a particles enrichment process is introduced within the SPA-based MTT that exploits the ARCE estimate to achieve a more effective sampling of the target state space. Angular constraints are forced such that the localization process exploits the available information about both the antenna beamwidth of the transmitter and the virtual beamwidth obtained from the target predicted uncertainty. Hence, the particle enrichment process replaces a subset of predicted particles with a new set of particles drawn from a distribution whose parameters depend on the ARCE location estimate. This novel technique is analyzed, showing its benefits in comparison with the conventional baseline SPA-based MTT and the stand-alone ARCE localization.

The above contributions have been subject of some of the author's publications listed at the end of this thesis. Specifically:

- The novel approach for elliptic localization in a PBR aided with an active radar has been presented in the author's publications [P3] and [P4];

  The technique proposed in [P3] ranked third to the Student Contest of the 1st International Virtual School on Radar Signal Processing, held at University of Electronic Science and Technology of China (UESTC), 22-23 December 2020.

- The 3D localization algorithm in MPRNs comprising one transmitter and multiple has been presented in publications [P6], [P7], and [P8].

  For contribution [P6], the author received the first prize at the Young Scientist Contest Award of the Signal Processing Symposium (SPSympo), Lodz, Poland, 21-23 September 2021.

The localization-enhanced MTT technique for MPRNs will be presented in future work.

The rest of the thesis is organized as follows.

Chapter 2 focuses on 2D target localization for a PBR co-located with an active radar.

In Chapter 3, 3D target localization with an MPRN comprising an active sensor and multiple synchronized receivers is addressed.

Chapter 4 deals with MTT for MPRNs through a sequential estimation process taking advantage of past information and knowledge of both the antenna beamwidth of the transmitter and the virtual beamwidth obtained from the target predicted uncertainty.

Finally, in Chapter 5 some conclusions are drawn and possible future research avenues highlighted.

Chapter 2

2D Localization for PBR Augmented with Active Radar Measurements

In this chapter, the model for a system consisting of a 2D PBR exploiting multiple illuminators of opportunity and a co-located active radar is presented. At the estimation design stage, *ad hoc* constraints accounting for both a-priori information related to the PBR receive antenna main-beam size and to the uncertainty characterizing active radar data are derived. Hence, the estimation task is cast as an elliptic positioning problem, according to the constrained LS framework, and a new 2D localization algorithm [57, 58] is devised for solving the positioning problem.

Finally, the algorithm performance are analyzed with respect to some counterparts from literature, in terms of RMSE, for both a static and a dynamic scenario.

2.1 System Model

A 2D PBR system, aided by a co-located active radar that capitalizes the signals emitted by N illuminators of opportunity (Fig. 2.1) is considered. Let be:

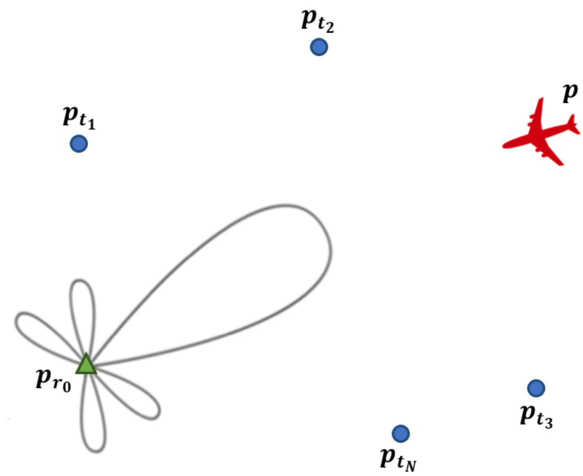

Figure 2.1. Pictorical representation of a surveillance system including a 2D PBR co-located with an active radar and N transmitters of opportunity.

- $\boldsymbol{p} = [x_p, y_p]^T \in \mathbb{R}^2$ the target position;
- $\boldsymbol{p}_{r_0} = [x_0, y_0]^T \in \mathbb{R}^2$ the PBR position (without loss of generality, it is assumed located at the origin of the reference system, i.e., $\boldsymbol{p}_{r_0} = [0, 0]^T$);
- $\boldsymbol{p}_{t_i} = [x_{t_i}, y_{t_i}]^T \in \mathbb{R}^2$ the position of the i-th illuminator of opportunity, $i = 1, \ldots, N$;
- $L_i = \|\boldsymbol{p}_{t_i} - \boldsymbol{p}_{r_0}\| \in \mathbb{R}$ the i-th baseline, $i = 1, \ldots, N$, i.e., the distance between the i-th transmitter and the receiver.

Thus, indicating by

$$\tilde{\tau}_i = \frac{1}{c}\left(\|\boldsymbol{p}\| + \|\boldsymbol{p} - \boldsymbol{p}_{t_i}\| - L_i\right), \quad i = 1, \ldots, N, \tag{2.1}$$

the noise-free output of the classic PBR cross-correlation based processing [59] (with c the speed of light), the following N noisy delay measurements are available at the receiver

$$\tau_i = \tilde{\tau}_i + n_i, \qquad i = 1, \ldots, N. \tag{2.2}$$

In (2.2), $n_1, \ldots, n_N$ are statistically independent (it is assumed that each transmitter of opportunity operates on different frequencies, i.e., there is no interference between multiple channels) zero-mean (usually Gaussian distributed) random variables with variance $\sigma_1^2, \ldots, \sigma_N^2$. These variances are modeled according to the Cramer Rao Lower Bound (CRLB) of the delay estimation as [60]

$$\sigma_i = \frac{1}{B_i\sqrt{2\mathrm{SNR}_i}}, \qquad i = 1, \ldots, N, \tag{2.3}$$

where B_i represents the frequency bandwidth of the i-th transmitter of opportunity, and SNR_i denotes the SNR of the i-th bistatic pair (i.e., receiver/i-th illuminator) computed via the bistatic radar range equation [60, 61]. It is worth pointing out that the SNR of each bistatic pair is dependent on the distance between the target and the specific receiver/i-th illuminator pair and from the radar cross section of the target, which is unknown. As a result, the quality of each measurement depends on the specific bistatic pair, due to both the spatial (geometric configuration) and the spectral (signal bandwidth) diversities induced by the transmitters of opportunity. To proceed further, let us manipulate equations (2.1) to obtain an equivalent representation of the noise-free model equations. To this end, denoting by

$$b_i = c\tilde{\tau}_i + L_i, \qquad i = 1, \ldots, N,$$

equations (2.1) can be cast as

$$b_i - \|\boldsymbol{p}\| = \|\boldsymbol{p} - \boldsymbol{p}_{t_i}\|, \qquad i = 1, \ldots, N,$$

or equivalently as

$$\begin{cases} b_i^2 + r^2 - 2b_i r = r^2 + r_i^2 - 2x_{t_i}x_p - 2y_{t_i}y_p \\ r \leq b_i, & i = 1, \dots, N, \\ r = \|\boldsymbol{p}\| \end{cases} \tag{2.4}$$

with $r_i = \|\boldsymbol{p}_{t_i}\|$, $i = 1, \dots, N$. Finally, the relationships in (2.4) can be cast in a more compact matrix form as

$$\begin{cases} \boldsymbol{H}\bar{\boldsymbol{p}} - \boldsymbol{g} = \boldsymbol{0} \\ \bar{\boldsymbol{p}}^T \boldsymbol{B} \bar{\boldsymbol{p}} = 0 \\ \bar{p}_3 \leq b_i, i = 1, \dots, N \end{cases} \tag{2.5}$$

where

$$\bar{\boldsymbol{p}} = [\boldsymbol{p}^T, r]^T \in \mathbb{R}^3,$$

$$\boldsymbol{H}^T = [\boldsymbol{h}_1, \boldsymbol{h}_2, \dots, \boldsymbol{h}_N] \in \mathbb{R}^{3,N},$$

with

$$\boldsymbol{h}_i = [-2x_{t_i}, -2y_{t_i}, 2b_i]^T \in \mathbb{R}^3\,,\ i = 1, \dots, N$$

and

$$\boldsymbol{g} = \left[g_1, \dots, g_N\right]^T \in \mathbb{R}^N,$$

with

$$g_i = b_i^2 - r_i^2\,,\ i = 1, \dots, N,$$

and

$$\boldsymbol{B} = \mathbf{diag}\,\{[1, 1, -1]\} \in \mathbb{R}^{3,3}.$$

2.1.1 Target State Constraints via Active-Radar Measurements & Sensing-System Features

This study is focused on a bi-sensor surveillance system where an active radar is complemented by a co-located gap-filler PBR which capitalizes actively-gathered target information to boost its localization performance. This is for instance the case where a passive system equipped with a circular array can exploit the target state estimates provided at each scanning period by a co-located active rotating radar.

In this context, it is possible to adapt the surveillance system measurement rate in a specific search sector of tactical interest staring the passive radar in that spatial portion, thus overcoming the intrinsic fixed-acquisition-rate limitations of the active rotating platform. This is a very important feature especially in the presence of fast and manoeuvring targets like the next generation threats, such as Intercontinental Ballistic Missiles (ICBMs) and cruise missiles.

Furthermore, an additional valuable knowledge related to the collected passive measurements (2.2) is represented by the 2D PBR beamwidth size. Thus, in the following, a specific framework to exploit, via appropriate constraints, the side-information provided by an active radar and the PBR antenna characteristics, is formalized, which is fundamental for the proposed estimation algorithm (from now on referred to as AACLS).

To this end, let us denote by:

- $\theta_p = \text{atan2}(y_p, x_p)$ the target angle of arrival;
- $\hat{R}^a$ and $\hat{\theta}^a$ the target range and azimuth estimates computed by the co-located active radar, whose uncertainties (related to measurement precisions as well as the estimation time) are indicated[1] by ρ_R^a and ρ_θ^a, respectively.

Hence, the target state, ruling the passive measurements (2.2), must comply with

$$R_1^a \leq r \leq R_2^a \tag{2.6}$$

and

$$\theta_1^a \leq \theta_p \leq \theta_2^a, \tag{2.7}$$

where

$$R_1^a = \hat{R}^a - \rho_R^a > 0,$$

[1] A reasonable choice is to select $\rho_R^a = c_R 3\sigma_R^a$ and $\rho_\theta^a = c_\theta 3\sigma_\theta^a$, where σ_R^a and σ_θ^a denote the standard deviations of the active radar estimation errors in range and azimuth, respectively, while $c_R \geq 1$ and $c_\theta \geq 1$ are accuracy degradation factors accounting for the elapsing time between measurements acquisition and their exploitation.

$$R_2^a = \hat{R}^a + \rho_R^a,$$

$$\theta_1^a = \hat{\theta}^a - \rho_\theta^a,$$

and

$$\theta_2^a = \hat{\theta}^a + \rho_\theta^a,$$

provided that an appropriate angular reference system is employed, for instance if $x > 0$ belongs to the cone identified by the azimuth estimate uncertainty then the angular reference system is $[-\pi, \pi[$. Furthermore, denoting by:

- θ^p the pointing direction of the PBR system;
- $\bar{\theta}^p$ the receiving (half-side) antenna beamwidth of the PBR system;

the beam extent forces the additional angular constraint (in the apposite angular reference system) [62]

$$\theta_1^p \leq \theta_p \leq \theta_2^p, \tag{2.8}$$

where

$$\theta_1^p = \theta^p - \bar{\theta}^p$$

and

$$\theta_2^p = \theta^p + \bar{\theta}^p.$$

Now, to jointly capitalize on the angular constraints (2.7)-(2.8) and proceed further into the localization problem formulation, two key assumptions are made. First, it is supposed that $\hat{\theta}^a, \theta^p \in [-\pi/2, \pi/2]$ and $0 < \rho_\theta^a, \bar{\theta}^p < \pi/2$ which is tantamount to requiring that the two sensors point in the same half space as well as that the angular reference system to adopt is $[-\pi, \pi[$. Second, it is assumed that the angular constraints are consistent, i.e., the intersection between (2.7)

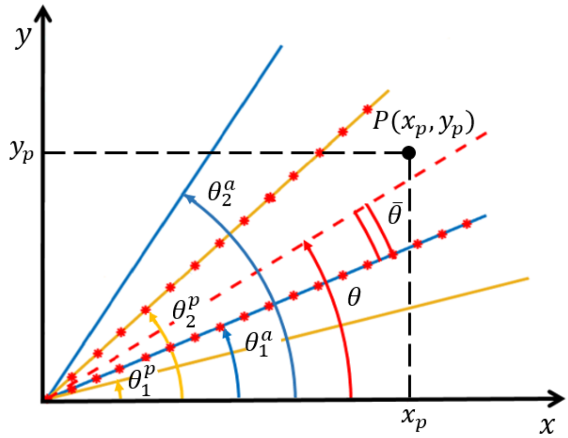

Figure 2.2. Notional representation of the angular constraint involved in the localization process: blue solid lines refer to active-radar restrictions, yellow solid lines concern PBR beam extent limitations, and red $*$-marked lines define the resulting angular constraint.

and (2.8) is not empty. Leveraging the above hypotheses, it follows that (see Fig. 2.2)

$$\theta - \bar{\theta} \leq \theta_p \leq \bar{\theta} + \theta, \tag{2.9}$$

where

$$\bar{\theta} = \frac{\min\{\theta_2^a, \theta_2^p\} - \max\{\theta_1^a, \theta_1^p\}}{2}$$

and

$$\theta = \frac{\min\{\theta_2^a, \theta_2^p\} + \max\{\theta_1^a, \theta_1^p\}}{2}.$$

Inequalities (2.9) can be cast as:

$$-\bar{\theta} \leq \theta_p - \theta \leq \bar{\theta},$$

or equivalently as:

$$-\tan(\bar{\theta}) \leq \tan(\theta_p - \theta) \leq \tan(\bar{\theta}), \tag{2.10}$$

being $0 \leq \bar{\theta} < \pi/2$.

As shown in [62], the following relationships on the tangent function hold:

$$\begin{aligned} \tan(\theta_p - \theta) &= \frac{\sin(\theta_p - \theta)}{\cos(\theta_p - \theta)} \\ &= \frac{\sin(\theta_p)\cos(\theta) - \cos(\theta_p)\sin(\theta)}{\cos(\theta_p)\cos(\theta) + \sin(\theta_p)\sin(\theta)} \\ &= \frac{y_p \cos(\theta) - x_p \sin(\theta)}{x_p \cos(\theta) + y_p \sin(\theta)}, \end{aligned} \tag{2.11}$$

where the last equality stems from $\sin(\theta_p) = \frac{y_p}{\sqrt{x_p^2+y_p^2}}$ and $\cos(\theta_p) = \frac{x_p}{\sqrt{x_p^2+y_p^2}}$.

Hence, exploiting equation (2.11), inequalities (2.10) become

$$-\tan(\bar{\theta}) \leq \frac{y_p \cos(\theta) - x_p \sin(\theta)}{x_p \cos(\theta) + y_p \sin(\theta)} \leq \tan(\bar{\theta}). \tag{2.12}$$

Again, following [62], the previous inequalities can be manipulated by introducing a new reference system, namely (x_1, y_1), obtained rotating the actual one (i.e., the (x, y)-coordinates system) such that the x_1-axis is aligned with the receiving antenna boresight. This is obtained through the rotation matrix

$$\bar{\boldsymbol{R}}(\theta) = \begin{bmatrix} \cos(\theta) & \sin(\theta) \\ -\sin(\theta) & \cos(\theta) \end{bmatrix} \tag{2.13}$$

by means of the following transformation

$$\begin{bmatrix} x_1 \\ y_1 \end{bmatrix} = \bar{\boldsymbol{R}}(\theta) \begin{bmatrix} x \\ y \end{bmatrix} = \begin{bmatrix} x\cos(\theta) + y\sin(\theta) \\ -x\sin(\theta) + y\cos(\theta) \end{bmatrix}.$$

As a consequence, inequalities (2.12) become

$$-\tan(\bar{\theta}) \leq \frac{p_2^\theta}{p_1^\theta} \leq \tan(\bar{\theta})$$

where $\boldsymbol{p}^\theta = [p_1^\theta, p_2^\theta]^T$ are the new coordinates associated with $\boldsymbol{p}$ according to

$$\boldsymbol{p}^\theta = \bar{\boldsymbol{R}}(\theta)\boldsymbol{p}.$$

Additionally, from the relationship

$$|\mathrm{atan2}(p_2^\theta, p_1^\theta)| = |\mathrm{atan2}(x_p, y_p) - \theta| < \frac{\pi}{2},$$

it directly follows that $p_1^\theta > 0$. Hence, the additional constraints to consider at the estimator design development as induced by the antenna beamwidth are given by:

$$\begin{cases} -p_1^\theta \tan(\bar{\theta}) \le p_2^\theta \le p_1^\theta \tan(\bar{\theta}) \\ p_1^\theta > 0 \end{cases}.$$

Finally, defining $\gamma = \tan(\bar{\theta})$ and since (2.13) is a unitary matrix, the constraints in (2.6), (2.7), and (2.8) can be expressed as

$$\begin{cases} R_1^a \le r \le R_2^a \\ -p_1^\theta \gamma \le p_2^\theta \le p_1^\theta \gamma \\ p_1^\theta \ge 0 \\ \boldsymbol{p}^\theta = \bar{\boldsymbol{R}}(\theta)\boldsymbol{p} \end{cases}. \tag{2.14}$$

2.2 Target Localization: Problem Formulation & Algorithm Design

In this section, the PBR localization problem with side-information is formalized and a solution technique to obtain a closed form target position estimate developed.

As to the problem formalization, the idea is to jointly account for PBR model relationships (2.5) and the constraints (2.14) induced by the available side-information. In this respect, note that, due to measurement errors impairing the matrix $\boldsymbol{H}$ and the vector $\boldsymbol{g}$, the first equation in (2.5) is only approximately true. Hence, a viable mean to circumvent this drawback is to resort to the constrained LS framework so as to satisfy as better as possible (in the LS sense) the first equation in (2.5) while satisfying all the remaining constraints. The target position estimation problem is thus formalized as:[2]

$$\begin{cases} \min_{\bar{\boldsymbol{p}}} & \|\boldsymbol{H}\bar{\boldsymbol{p}} - \boldsymbol{g}\|^2 \\ \text{s.t.} & \bar{\boldsymbol{p}}^T \boldsymbol{B} \bar{\boldsymbol{p}} = 0 \\ & \bar{p}_3 \leq b_i, \;\; i = 1, \ldots, N \\ & R_1^a \leq r \leq R_2^a \\ & -p_1^\theta \gamma \leq p_2^\theta \leq p_1^\theta \gamma \\ & p_1^\theta \geq 0 \\ & \boldsymbol{p}^\theta = \bar{\boldsymbol{R}}(\theta) \boldsymbol{p} \end{cases} \tag{2.15}$$

Now, introducing the unitary matrix

$$\boldsymbol{U} = \begin{bmatrix} \bar{\boldsymbol{R}}(\theta) & 0 \\ 0 & 1 \end{bmatrix},$$

performing the change of variable $\tilde{\boldsymbol{p}} = \boldsymbol{U}\bar{\boldsymbol{p}}$, (2.15) is formulated as

$$\begin{cases} \min_{\tilde{\boldsymbol{p}}} & \|\boldsymbol{H}\boldsymbol{U}^T \tilde{\boldsymbol{p}} - \boldsymbol{g}\|^2 \\ \text{s.t.} & \tilde{\boldsymbol{p}}^T \boldsymbol{U}\boldsymbol{B}\boldsymbol{U}^T \tilde{\boldsymbol{p}} = 0 \\ & R_1^a \leq \tilde{p}_3 \leq c_1 \\ & -\tilde{p}_1 \gamma \leq \tilde{p}_2 \leq \tilde{p}_1 \gamma \\ & \tilde{p}_1 \geq 0 \end{cases} \tag{2.16}$$

Finally, introducing $\tilde{\boldsymbol{H}} = \boldsymbol{H}\boldsymbol{U}^T$ and since $\boldsymbol{U}\boldsymbol{B}\boldsymbol{U}^T = \boldsymbol{B}$, (2.16) becomes:

[2] With a slight abuse of notation, the model parameters in (2.5), i.e., $\boldsymbol{H}$, $\boldsymbol{g}$, and $b_i, i = 1, \ldots, N$, are computed exploiting the actual measurements $\tau_i, i = 1, \ldots, N$, in place of $\tilde{\tau}_i, i = 1, \ldots, N$.

$$\mathcal{P}\begin{cases}\min\limits_{\tilde{\boldsymbol{p}}} \|\tilde{\boldsymbol{H}}\tilde{\boldsymbol{p}}-\boldsymbol{g}\|^2 & \\ \text{s.t. } \tilde{\boldsymbol{p}}^T\boldsymbol{B}\tilde{\boldsymbol{p}}=0 & (2.17a)\\ \quad R_1^a \le \tilde{p}_3 \le c_1 & (2.17b)\\ \quad -\tilde{p}_1\gamma \le \tilde{p}_2 \le \tilde{p}_1\gamma & (2.17c)\\ \quad \tilde{p}_1 \ge 0 & (2.17d)\end{cases}$$

where $c_1 = \min\{\min\limits_{i=1,\ldots,N}\{b_i\}, R_2^a\}$.

Problem $\mathcal{P}$ is a non-convex optimization problem due to the constraint (2.17a). Nevertheless, exploiting the Karush-Kuhn-Tucker (KKT) optimality conditions, an optimal solution to $\mathcal{P}$ can be obtained. The procedure providing a closed-form global minimizer to the localization Problem $\mathcal{P}$ is summarized in the following Proposition. Therein $\tilde{\boldsymbol{H}} = \left[\tilde{\boldsymbol{H}}_1, \tilde{\boldsymbol{h}}_3\right]$, with $\tilde{\boldsymbol{h}}_3 \in \mathbb{R}^3$.

Proposition 2.2.1. *An optimal solution to $\mathcal{P}$ belongs to the following finite set of feasible points (whose cardinality is at most fourteen):*

1. $\tilde{\boldsymbol{x}}^*(\eta_h) = \left(\tilde{\boldsymbol{H}}^T\tilde{\boldsymbol{H}} + \eta_h\boldsymbol{B}\right)^{-1}\tilde{\boldsymbol{H}}^T\boldsymbol{g}$, $h \in I_1 \subseteq \{1,\ldots,4\}$, *with η_h the real-valued solutions to the fourth-order equation*

$$\tilde{\boldsymbol{x}}^*(\eta)^T\boldsymbol{B}\tilde{\boldsymbol{x}}^*(\eta) = 0 \qquad (2.18)$$

with

$$\eta \in \left(-\frac{1}{\lambda_2\left(\boldsymbol{B},\tilde{\boldsymbol{H}}^T\tilde{\boldsymbol{H}}\right)}, +\infty\right) - \left\{-\frac{1}{\lambda_1\left(\boldsymbol{B},\tilde{\boldsymbol{H}}^T\tilde{\boldsymbol{H}}\right)}, -\frac{1}{\lambda_3\left(\boldsymbol{B},\tilde{\boldsymbol{H}}^T\tilde{\boldsymbol{H}}\right)}\right\} \qquad (2.19)$$

such that

$$\begin{cases} R_1^a < \tilde{x}_3^*(\eta_h) < c_1 \\ -\gamma\tilde{x}_1^*(\eta_h) < \tilde{x}_2^*(\eta_h) < \gamma\tilde{x}_1^*(\eta_h) \\ \tilde{x}_1^*(\eta_h) > 0 \end{cases} . \qquad (2.20)$$

2. $\tilde{\boldsymbol{x}}^*(\beta_h) = \left[\left(\boldsymbol{g} - \tilde{\boldsymbol{h}}_3 c_1\right)^T \tilde{\boldsymbol{H}}_1 \left(\tilde{\boldsymbol{H}}_1^T \tilde{\boldsymbol{H}}_1 + \beta_h \boldsymbol{I}\right)^{-1}, c_1\right]^T$, $h \in I_2 \subseteq \{1, \ldots, 4\}$, *with* β_h *the real-valued solutions to the fourth-order equation*

$$\left|\left(\tilde{\boldsymbol{H}}_1^T \tilde{\boldsymbol{H}}_1 + \beta_h \boldsymbol{I}\right)^{-1} \tilde{\boldsymbol{H}}_1^T \left(\boldsymbol{g} - \tilde{\boldsymbol{h}}_3 c_1\right)\right|^2 = c_1^2 \tag{2.21}$$

such that

$$\begin{cases} \beta_h \in \left(-\lambda_{max}\left(\tilde{\boldsymbol{H}}_1^T \tilde{\boldsymbol{H}}_1\right), +\infty\right) - \left\{-\lambda_{min}\left(\tilde{\boldsymbol{H}}_1^T \tilde{\boldsymbol{H}}_1\right)\right\} \\ -\gamma \tilde{x}_1^*(\beta_h) < \tilde{x}_2^*(\beta_h) < \gamma \tilde{x}_1^*(\beta_h) \\ \tilde{x}_1^*(\beta_h) > 0 \end{cases} . \tag{2.22}$$

3. $\tilde{\boldsymbol{x}}^*(\zeta_h) = \left[\left(\boldsymbol{g} - \tilde{\boldsymbol{h}}_3 R_1^a\right)^T \tilde{\boldsymbol{H}}_1 \left(\tilde{\boldsymbol{H}}_1^T \tilde{\boldsymbol{H}}_1 + \zeta_h \boldsymbol{I}\right)^{-1}, R_1^a\right]^T$, $h \in I_3 \subseteq \{1, \ldots, 4\}$, *with* ζ_h *the real-valued solutions to the fourth-order equation*

$$\left|\left(\tilde{\boldsymbol{H}}_1^T \tilde{\boldsymbol{H}}_1 + \zeta_h \boldsymbol{I}\right)^{-1} \tilde{\boldsymbol{H}}_1^T \left(\boldsymbol{g} - \tilde{\boldsymbol{H}}_3 R_1^a\right)\right|^2 = R_1^{a\,2} \tag{2.23}$$

such that

$$\begin{cases} \zeta_h \in \left(-\lambda_{max}\left(\tilde{\boldsymbol{H}}_1^T \tilde{\boldsymbol{H}}_1\right), +\infty\right) - \left\{-\lambda_{min}\left(\tilde{\boldsymbol{H}}_1^T \tilde{\boldsymbol{H}}_1\right)\right\} \\ -\gamma \tilde{x}_1^*(\zeta_h) < \tilde{x}_2^*(\zeta_h) < \gamma \tilde{x}_1^*(\zeta_h) \\ \tilde{x}_1^*(\zeta_h) > 0 \end{cases} . \tag{2.24}$$

4. $\boldsymbol{x}_{4_i}^* = \alpha_i^* \left[1,\, (-1)^{i+1}\gamma,\, \sqrt{1+\gamma^2}\right]^T$, $i = 1, 2$, *with*

$$\alpha_i^* = \min\left(\max\left(\frac{R_1^a}{\sqrt{1+\gamma^2}}, \frac{\boldsymbol{v}_i^T \boldsymbol{g}}{||\boldsymbol{v}_i||^2}\right), \frac{c_1}{\sqrt{1+\gamma^2}}\right)$$

and

$$\boldsymbol{v}_i = \tilde{\boldsymbol{H}}\left[1, (-1)^{i+1}\gamma, \sqrt{1+\gamma^2}\right]^T.$$

Proof. See Appendix A.1 □

A notional presentation of the proposed localization procedure is reported in Fig. 2.3. A more detailed and formal description of

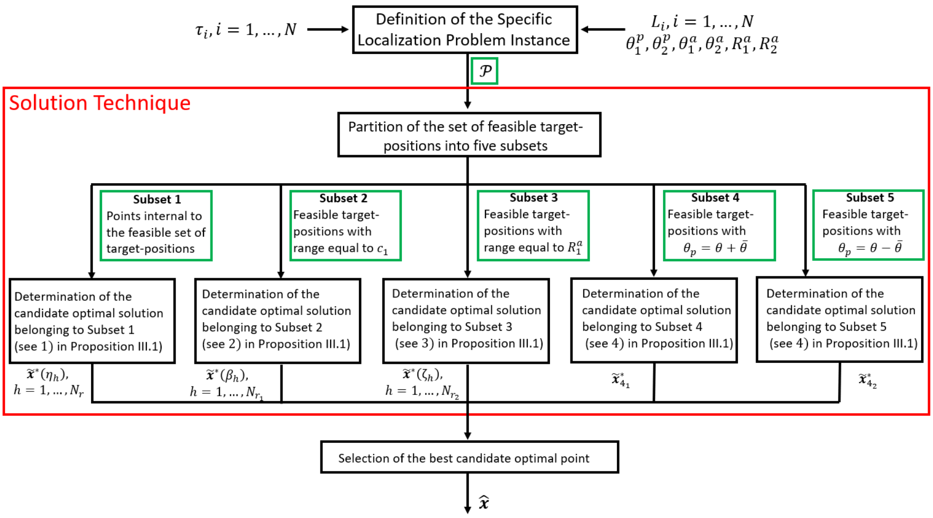

Figure 2.3. AACLS solution technique scheme.

the global optimum search technique, in the following referred to as AACLS method, is reported in **Algorithm 1**.

Before concluding this section, some useful considerations are in order.

Firstly, AACLS does not need any knowledge about measurement accuracies; this is very important from a practical standpoint as the foregoing parameters are functionally dependent on the actual target location (which is of course unknown during the system operation).

Secondly, the envisaged procedure allows for target position estimate in closed-form just using elementary functions, blackwith a global computational complexity given by $\mathcal{O}(N^2)$, where N is the number of bistatic range measurements.

The main steps in the implementation of **Algorthm 1** are:

1. Computation of the roots of the fourth order equations in (2.18), (2.21) and (2.23). For each equation, the sought solutions are available in closed-form via the evaluation of the elementary functions involved in Cardano-Tartaglia's formula [63] (i.e., with

a complexity $\mathscr{O}(1)$) given the equation coefficients; the latters are still available in closed-form since the eigenvalues and eigenvectors of a 3×3 real matrix $\boldsymbol{C}$, can be computed through elementary functions of its entries $C_{i,h}, (i,h) \in \{1,2,3\}^2$, [64]. The underlying matrix $\boldsymbol{C}$, given by $\tilde{\boldsymbol{H}}^T \tilde{\boldsymbol{H}}$ and $\tilde{\boldsymbol{H}}_1^T \tilde{\boldsymbol{H}}_1$ for the cases 1) and 2) or 3), respectively, is computed with a computational complexity of $\mathscr{O}(N^2)$;

2. Evaluation of $\tilde{\boldsymbol{x}}^*(\eta_h),\ h \in I_1 \subseteq \{1,\ldots,4\}, \tilde{\boldsymbol{x}}^*(\beta_h),\ h \in I_2 \subseteq \{1,\ldots,4\}$, and $\tilde{\boldsymbol{x}}^*(\zeta_h),\ h \in I_3 \subseteq \{1,\ldots,4\}$; for each candidate optimal solution, the most demanding operation is the computation of the inverse of a specific 3×3 matrix which entails a computational complexity of $\mathscr{O}(1)$, being available in closed form;. Construction of $\tilde{\boldsymbol{x}}^*_{4_1}$ and $\tilde{\boldsymbol{x}}^*_{4_2}$, that are available in closed-form, i.e., $\mathscr{O}(1)$;

3. Selection of the point achieving the lowest objective value; it requires the evaluation of the objective function value, involving a computational burden of $\mathscr{O}(N)$, for at most fourteen points so as to pick up the best solution.

Algorithm 1 AACLS algorithm.

Input: τ_i, L_i, $\boldsymbol{p}_{t_i}$, $i = 1, \ldots, N$, θ_1^p, θ_2^p, θ_1^a, θ_2^a, R_1^a, R_2^a;

Output: Target location estimate $[\hat{x}_p, \hat{y}_p]^T$;

Parameter setup

- Compute $\boldsymbol{U}$, $\bar{\boldsymbol{R}}(\theta)$, $\tilde{\boldsymbol{H}}$, $\tilde{\boldsymbol{H}}_1$, $\boldsymbol{B}$, $\tilde{\boldsymbol{h}}_3$, $\boldsymbol{v}_i, i = 1, 2$, c_1, θ, $\bar{\theta}$, γ, and $\alpha_i^*, i = 1, 2$

1. **Roots computation**
   - Find the roots η_h, $h \in I_1 \subseteq \{1, \ldots, 4\}$ of equation (2.18) belonging to the interval (2.19);
   - Find the roots β_h, $h \in I_2 \subseteq \{1, \ldots, 4\}$ of equation (2.21) belonging to the interval in the first relationship of (2.22);
   - Find the roots ζ_h, $h \in I_3 \subseteq \{1, \ldots, 4\}$ of equation (2.23) belonging to the interval in the first relationship of (2.24).
2. **Candidate points evaluation**
   - Compute $\tilde{\boldsymbol{x}}^*(\eta_h)$, satisfying the inequalities in (2.20);
   - Compute $\tilde{\boldsymbol{x}}^*(\beta_h)$, fulfilling the last two relationships in (2.22);
   - Compute $\tilde{\boldsymbol{x}}^*(\zeta_h)$, fulfilling the last two relationships in (2.24);
   - Compute $\tilde{\boldsymbol{x}}_{4_i}^*$, $i = 1, 2$.
3. **Optimal solution selection**
   - Compute
     - $v_j = \|\tilde{\boldsymbol{H}}\tilde{\boldsymbol{x}}^*(\eta_i) - \boldsymbol{g}\|^2$, $j = 1, \ldots, |I_1|$,
     - $v_{|I_1|+j} = \|\tilde{\boldsymbol{H}}\tilde{\boldsymbol{x}}^*(\beta_i) - \boldsymbol{g}\|^2$, $j = 1, \ldots, |I_2|$,
     - $v_{|I_1|+|I_2|+j} = \|\tilde{\boldsymbol{H}}\tilde{\boldsymbol{x}}^*(\zeta_i) - \boldsymbol{g}\|^2$, $j = 1, \ldots, |I_3|$,
     - $v_{|I_1|+|I_2|+|I_3|+j} = \|\tilde{\boldsymbol{H}}\tilde{\boldsymbol{x}}_{4_i}^* - \boldsymbol{g}\|^2$, $j = 1, 2$.
   - Determine $j^* = \arg\min_j v_j$ and pick up the corresponding solution, i.e.,

$$\tilde{\boldsymbol{x}}^* = \begin{cases} \tilde{\boldsymbol{x}}^*(\eta_{j^*}) & \text{if } 1 \leq j^* \leq |I_1| \\ \tilde{\boldsymbol{x}}^*(\beta_{j^*}) & \text{if } |I_1| + 1 \leq j^* \leq |I_1| + |I_2| \\ \tilde{\boldsymbol{x}}^*(\zeta_{j^*}) & \text{if } |I_1| + |I_2| + 1 \leq j^* \leq |I_1| + |I_2| + |I_3| \\ \tilde{\boldsymbol{x}}_{4_{j^*}}^* & \text{if } |I_1| + |I_2| + |I_3| + 1 \leq j^* \leq |I_1| + |I_2| + |I_3| + 2, \end{cases}$$

Output $[\hat{x}_p, \hat{y}_p]^T = \bar{\boldsymbol{R}}(\theta)^T [\tilde{x}_1^*, \tilde{x}_2^*]^T$.

2.3 Other Localization Algorithms

For comparison purposes, also the performance of some counterparts available in the open literature, e.g., LS [64], Two-Step Estimation (TSE) [30], and Angular Constrained Least Square (ACLS) algorithms [62] are illustrated. The observation model for the specific surveillance system can be expressed, without constraints, as

$$\tilde{\boldsymbol{H}}\tilde{\boldsymbol{p}} - \boldsymbol{g} = \boldsymbol{0}. \tag{2.25}$$

Starting from equation (2.25) and assuming $\tilde{\boldsymbol{H}}$ full-rank, the aforementioned techniques are derived as in the following.

- The LS approach [64] determines the target location estimate $\hat{\boldsymbol{p}}_{LS}$ as the first two components of the optimal solution to Problem $\mathcal{P}$ when no constraints are forced, i.e.,

$$[\hat{\boldsymbol{p}}_{LS}, \hat{r}]^T = \arg\min_{\tilde{\boldsymbol{p}} \in \mathbb{R}^3} \|\tilde{\boldsymbol{H}}\tilde{\boldsymbol{p}} - \boldsymbol{g}\|^2 = (\tilde{\boldsymbol{H}}^T\tilde{\boldsymbol{H}})^{-1}\tilde{\boldsymbol{H}}^T\boldsymbol{g}.$$

- The TSE procedure [30] provides an approximated Maximum Likelihood (ML) position estimate, assuming a simplified statistical signal model of the observations.

  To this end, a two step procedure is developed. The first step determines an initial estimate, not accounting for the functional dependency among the involved unknowns. In the second step an appropriate refinement is performed to overcome the above limitation:
  A) four well conditioned location estimates are computed;
  B) the position estimate is thus obtained selecting among the four candidates the one providing the best matching with the range measurements.

- The ACLS algorithm [62] corresponds to a simplified version of the AACLS strategy, where the constraints induced by the active-radar information are no longer forced. Unlike AACLS, for the ACLS the target feasible positions describe a convex set. Remarkably, ACLS estimate can be obtained via Algorithm 1, with θ and $\bar{\theta}$ equal to the squint angle and the receiving (half-side) antenna beamwidth of the PBR antenna boresight, respectively, as well as $R_1^a = 0$, and $c_1 = \min_{i=1,\dots,N}\{b_i\}$.

2.4 Performance Analysis

In this section, the performance assessment of the proposed AACLS localization algorithm is addressed for a PBR capitalizing echoes induced by multiple illuminators of opportunity. To this end, $N = 3$ omni-directional transmitters of opportunity are supposed available in the analyzed localization scenario.

The simulation setup is depicted in Fig. 2.4. The transmitters are located at the vertices of an equilateral triangle whose barycenter coincides with the origin of the reference system, where the receiver is located. The triangle side is assumed equal to $20\cos(\pi/6)$ km, which corresponds to a distance of 10 km between any transmitter and the receiver, i.e., $L_i = 10$ km, $i = 1, 2, 3$. As to the side-information provided by an active surveillance system, a precision for the range and azimuth measurements given by 116 m and 0.5° respectively, is assumed. Otherwise stated: $\rho_R^a = 116$ m and $\rho_\theta^a = 0.5°$.

Remarkably, this situation is representative of the measurements precision/quality provided for instance by the AN/SPS-49A(V)1 radar [65], which is a two-dimensional, long range radar that measures bearing and range contacts. The AN/SPS-49A(V)1 operates in the L-band and has a range of 256 nautical miles (474 km), with a narrow 3.3 deg-beam. Moreover it can rotate at either 6 or 12 rpm, to provide more frequent scans against incoming threats.

In the following, the measurements errors are modeled according to equations (2.3), where the SNR of the $N = 3$ bistatic pairs (receiver-transmitter of opportunity) is set as in [61]:

$$\mathrm{SNR}_i = \mathrm{SNR}_0 \frac{\|\boldsymbol{q}_0\|^2}{\|\boldsymbol{p}\|^2} \frac{\|\boldsymbol{q}_0 - \boldsymbol{p}_{t_1}\|^2}{\|\boldsymbol{p} - \boldsymbol{p}_{t_i}\|^2}, \quad i = 1, 2, 3,$$

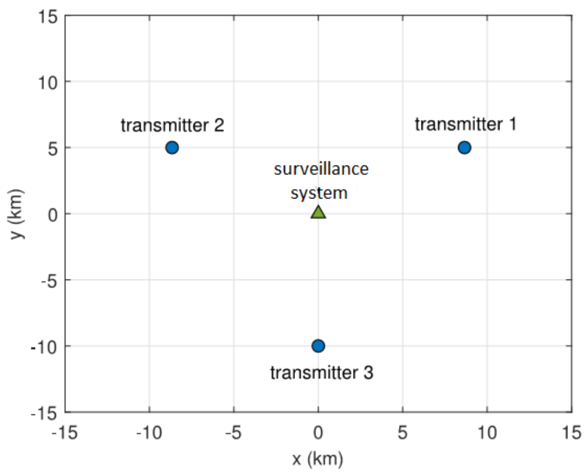

Figure 2.4. Surveillance system geometric configuration: a receiver deployed at the origin of the reference system and $N = 3$ transmitters of opportunity located at the vertices of an equilateral triangle ($L_i = 10$ km, $i = 1, 2, 3$).

where SNR_0 is a reference SNR value associated with a reference bistatic triad $\boldsymbol{p}_{t_1} - \boldsymbol{q}_0 - \mathbf{0}$; specifically, SNR_0 is computed resorting to the bistatic radar range equation [60, 61], related to a reference point $\boldsymbol{q}_0 = [x, y]^T$, and the transmitter at $\boldsymbol{p}_{t_1}$.

The performance of the devised localization algorithm is analyzed in terms of the target position estimate RMSE. In this respect, due to the lack of a closed-form expression for the RMSE, Monte Carlo simulation method is exploited, assuming 1000 independent trials. For comparison purposes, also the performance of some counterparts available in the open literature, e.g., LS [64], TSE [30], and ACLS algorithms [66] are illustrated.

In the following subsections two different case studies are analyzed. The former assumes a static target situation, where the target is located in a fixed position; the latter considers a dynamic target scenario, in which the target follows a given trajectory, and PBR is aided just in some time-instants by active radar-based information.

2.4.1 Fixed target scenario

This subsection deals with the performance analysis of the AACLS considering a stationary target. To this end, the target is assumed located at $[r\cos\theta_p, r\sin\theta_p]^T$ with $r = 40$ km; as to θ_p, to assess the estimator behaviour for different localization scenarios, diverse values of the target azimuth are considered, namely, $\theta_p = 0°, 7°$, and $9.7403°$, as illustrated in Figs. 2.5 (b)-(d)-(f). Therein, it is also reported the position of the available active measure exploited in the localization process. Moreover, the receiving antenna is assumed steered at $\theta = 0°$ with a main-beam width of $\bar{\theta} = 10°$.

The results show that AACLS outperforms counterparts, e.g., LS, TSE, and ACLS algorithms, in the entire range of SNR values and for all the considered scenarios, clearly highlighting the capabilities of the proposed strategy to capitalize a-priori information to boost localization performance. In order to provide increased visibility of the performance especially at high SNR values, Fig. 2.6 shows the estimation performance for $\theta_p = 0°$ in logarithmic scale.

The results also reveal that, as the SNR increases, all the considered localization techniques, e.g., AACLS, ACLS, unconstrained LS, and TSE, achieve better performance providing lower and lower RMSE values.

Finally, it is worth observing that AACLS for $\theta_p = 0°$ performs almost the same as for $\theta_p = 7°$ whereas ACLS improves its estimation capabilities. This behaviour is not surprising and can be justified observing that for the ACLS the closer the target to the PBR main-lobe boundary the more valuable the beampattern extent constraint. On the other side, the AACLS is totally blind to the PBR angular extent constraint as long as the state-space limitation induced by active radar side-information is the most stringent, as for the case studies of Figs. 2.5(a) and 2.5(c).

To corroborate these insights, it can be observed that in Fig. 2.5(e) both AACLS and ACLS improve their estimation capabilities; in fact in such a scenario the PBR angular constraint effectively contributes to the definition of the target state-space feasible set even in the presence of the active radar induced limitations.

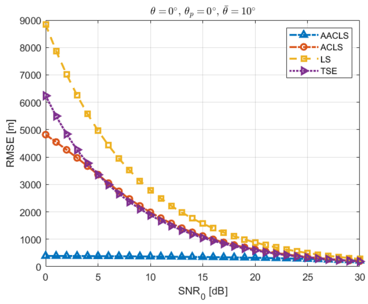

(a) $\theta_p = 0^\circ$.

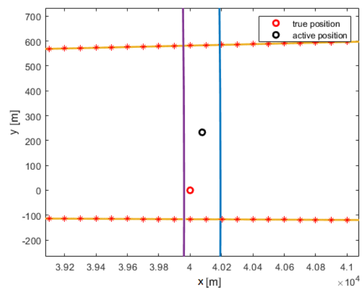

(b) Target and active measure.

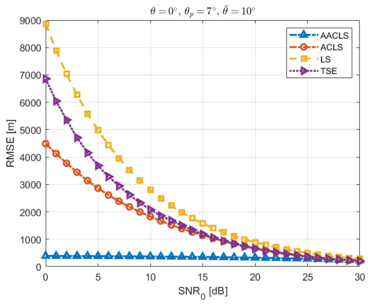

(c) $\theta_p = 7^\circ$.

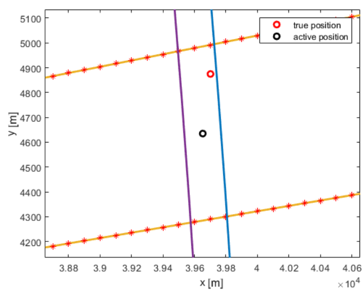

(d) Target and active measure.

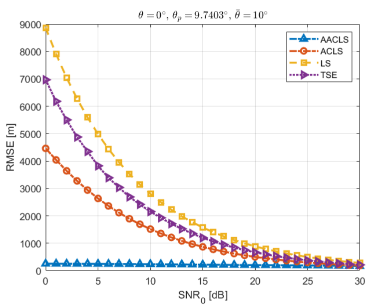

(e) $\theta_p = 9.7403^\circ$.

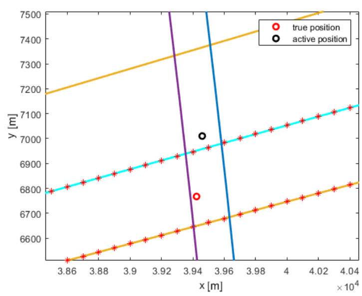

(f) Target and active measure.

Figure 2.5. Estimation capabilities of different localization algorithms: (a)-(c)-(e) report RMSE verus SNR_0 for the setup depicted in (b)-(d)-(f). Therein blue and violet lines correspond to the range constraint, while the red $*$-marked lines indicate the angular constraint (the yellow and the cyan curves are related to the active-radar and the PBR beam-width angular limitations, respectively).

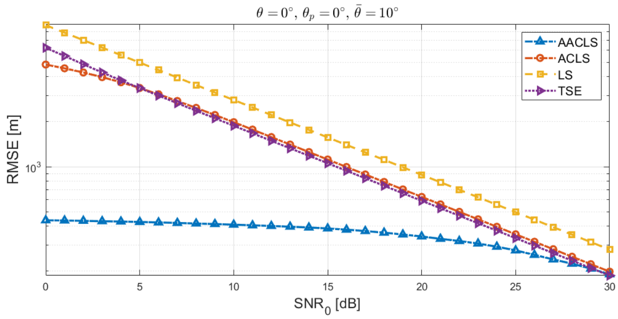

Figure 2.6. Estimation capabilities of different localization algorithms in logarithmic scale, when $\theta_p = 0°$.

2.4.2 Moving target scenario

In this subsection, the AACLS estimation capabilities are assessed for a dynamic scenario where the target of interest is approaching the surveillance system, composed of an active radar and a passive system. The former is assumed equipped with a vertical fan-shaped-beam rotating antenna that scans the surveillance area every 10 s, e.g., it rotates at a rate of 6 rpm. The latter exploits a circular array steered in the direction triggered by the active radar with a halfside beamwidth of 10°, to collect target reflections from emitters of opportunity (the same scenario as in Fig. 2.4 is considered).

In the following, it is supposed that the PBR radar acquires target information each second. As a result, assuming, without loss of generality, that at $t_0 = 0$ the first active measurement is gathered, in all the time instants that are not multiple of 10 s, no active side-information is available and a prediction of the active system-based constraints is required. To this end, provided that the PBR system possesses an a-priori knowledge about the maximum radial and angular velocities of the target, upper and lower bounds to the target range and angular locations can be forced in any time instant capitalizing the previous active measurement. Specifically, denoting by v_{max} and w_{max} the upper bounds to the range and angular absolute value velocities, respectively, at a time instant t such that

$k10 \leq t < (k+1)10,\ k = 0, 1, \ldots, N_0$ (with $10N_0$ the overall target observation interval), the constraints:

$$\begin{cases} R_1^a(t) = \hat{R}_k^a - (\rho_R^a + (t - k10)v_{max}) \\ R_2^a(t) = \hat{R}_k^a + (\rho_R^a + (t - k10)v_{max}) \\ \theta_1^a(t) = \hat{\theta}_k^a - (\rho_\theta^a + (t - k10)\omega_{max}) \\ \theta_2^a(t) = \hat{\theta}_k^a + (\rho_\theta^a + (t - k10)\omega_{max}) \end{cases}$$

can be forced, where $\hat{R}_k^a$ and $\hat{\theta}_k^a$ denote the range and angle estimates provided by the active surveillance system at the time instant $k10$ s. In the following, $\hat{R}_k^a$ and $\hat{\theta}_k^a$ are modeled[3] as independent Gaussian random variables with mean equals to the target range r and the target azimuth angle θ_p at the time instant $k10$, and variance ρ_R^a and ρ_θ^a, respectively.
In the reported case studies, it is assumed that the SNR of the i-th bistatic pair, $i = 1, 2, 3$, at a time instant t, is given by:

$$\mathrm{SNR}_i(t) = \mathrm{SNR}_0 \frac{\|\boldsymbol{q}_0\|^2}{\|\boldsymbol{p}(t)\|^2} \frac{\|\boldsymbol{q}_0 - \boldsymbol{p}_{t_1}\|^2}{\|\boldsymbol{p}(t) - \boldsymbol{p}_{t_i}\|^2}, \quad i = 1, 2, 3,$$

where $p(t) \in \mathbb{R}^2$ is the target position at the time instant t and SNR_0 is the SNR of the reference bistatic pair, i.e., of the triad $\boldsymbol{p}_{t_1} - \boldsymbol{q}_0 - \boldsymbol{0}$, where $\boldsymbol{q}_0$ is the initial target position with reference to the scenarios of Fig. 2.7. Moreover, a target moving with a uniform radial velocity v_0 (equals to either 150 or 190 m/s) and initial position $\boldsymbol{p}_0 = [r\cos\theta_p, r\sin\theta_p]^T$ with $r = 20$ km and θ_p given by either $5°$ or $9.6667°$, is considered. Finally, it is supposed that the pointing direction of the PBR system is at $\theta = 0$, $N_0 = 20$, $v_{max} = 200$ m/s and $\omega_{max} = 0.0025$ rad/s.

The last two assumptions are representative of a harbour surveillance environment, where possible hostile targets are anti-ship missiles such as the sea-skimming ones (whose maximum velocity can be larger than 175 m/s). In this respect, note that a maximum angular velocity of 0.0025 rad/s at 20 km is tantamount to assuming a maximum

[3] Only the active-based constraints are considered, if Problem $\mathcal{P}$ results infeasible.

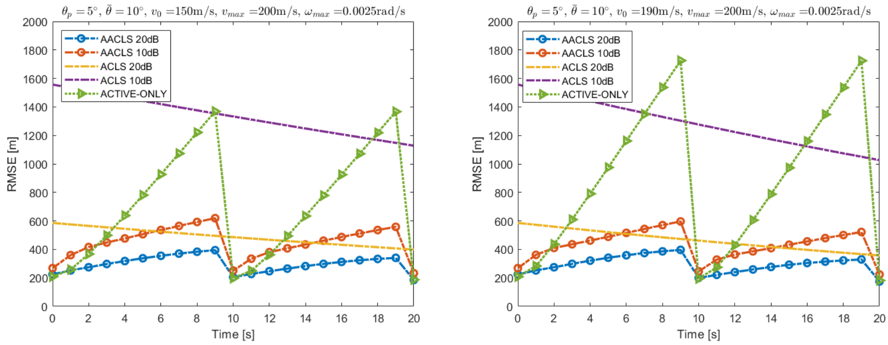

(a) $v_0 = 150$ m/s.

(b) $v_0 = 190$ m/s.

Figure 2.7. RMSE versus time, assuming $\theta_p = 5°$, for target approaching the surveillance system: (a) and (b) refer to $v_0 = 150$ and 190 m/s, respectively.

cross-range velocity of 50 m/s, i.e., 97 knots, to possibly accommodate maneuvers and a not exactly radial trajectory.

Figs. 2.7 display the RMSE versus the observation time provided by the different localization algorithms, assuming $\theta_p = 5°$. Specifically, the performance of AACLS, ACLS, and active-based localizer[4] are reported. Fig. 2.7(a) and Fig. 2.7(b) refer to $v_0 = 150$ and $v_0 = 190$ m/s, respectively, and SNR_0 equals to either 10 or 20 dB is considered. Inspection of Figs. 2.7 reveals that AACLS strategy outperforms ACLS and that both the algorithms improve their localization capabilities as SNR_0 increases. Interestingly, the larger the observation time the better the ACLS performance, due to a higher effective target SNR (the target is closer and closer to the receiver).

This trend is also partially true for the AACLS technique, where improvements can be observed among the time instants characterized by the same accuracy level of active-based constraints, namely with the same time-lag from the acquisition of the active measurements. Otherwise stated, for the AACLS the SNR increase may compete

[4] It only relies on active measurements and assumes the target does not move in the time instants where measurements are not available. It is referred to as Active-Only in the following.

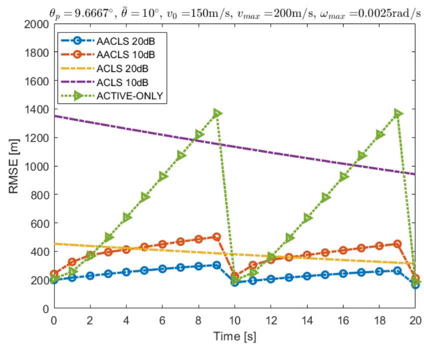

(a) $v_0 = 150$ m/s.

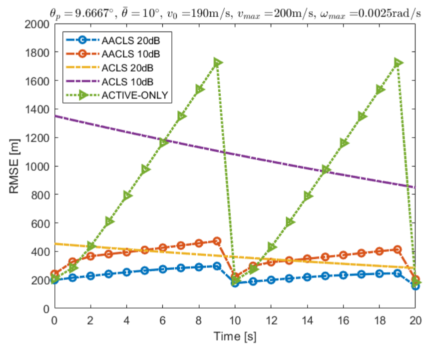

(b) $v_0 = 190$ m/s.

Figure 2.8. RMSE versus time, assuming $\theta_p = 9.6667°$, for target approaching the surveillance system: (a) and (b) refer to $v_0 = 150$ and 190 m/s, respectively.

with less accurate constraints, depending on the specific time instant, i.e., a trade-off between a reduced distance from the receiver and a larger delay from the temporally closest active measure is present.

The results also show that AACLS exhibits better estimation capabilities than the active-based localizer as long as the latter relies on old measurements, clearly highlighting the effectiveness of the proposed localization algorithm. In addition, as expected, AACLS achieves its best performance (substantially overlapped with that of the active-based predictor) in the time instants where active measurements are available. Finally, comparing Figs. 2.7(a) and 2.7(b) it is evident that the performance of AACLS and ACLS does not change significantly[5] with v_0, while the active-based localizer experiences a considerable degradation. This is not surprising, being the assumption of target stationarity less and less accurate as the velocity increases.

To shed light on the impact of the angular constraint induced by the PBR, in Figs. 2.8 the performance for a target at $\theta_p = 9.6667°$ is illustrated. The preceding remarks substantially hold true also for this case study. In addition, the results confirm the insights of Fig. 2.5(e), namely the PBR constraint can boost the localization performance

[5]Some gains of Fig. 2.7(b) are reasonably due to a larger effective SNR.

as long as it is effectively involved in the estimation process.

Chapter 3

3D Localization for Deployable Multiplatform Radar Networks

In this chapter, the model for a MPRN, comprising one transmitter and multiple receivers, is presented. At the estimation design stage, *ad hoc* constraints accounting for the information embedded into the monostatic sensor radiation pattern features are derived. Hence, the positioning problem is formulated as a constrained LS problem, and a new algorithm for 3D localization [67–69] is proposed.

The performance of the new algorithm is assessed in terms of RMSE in comparison with the benchmark Root Cramer Rao Lower Bound (RCRLB) and some competitors from the open literature, for different numbers of sensors and for the scenario where the radar antenna pointing direction rotates in the $x-y$ plane.

3.1 System Model

Let us consider a multistatic radar network with an active sensor and N synchronized receivers, as illustrated in Fig. 3.1, and denote by:

- $\boldsymbol{p} = [x_p, y_p, z_p]^T \in \mathbb{R}^3$ the target position;
- $\boldsymbol{p}_{r_0} = [x_0, y_0, z_0]^T \in \mathbb{R}^3$ the active radar position (without loss

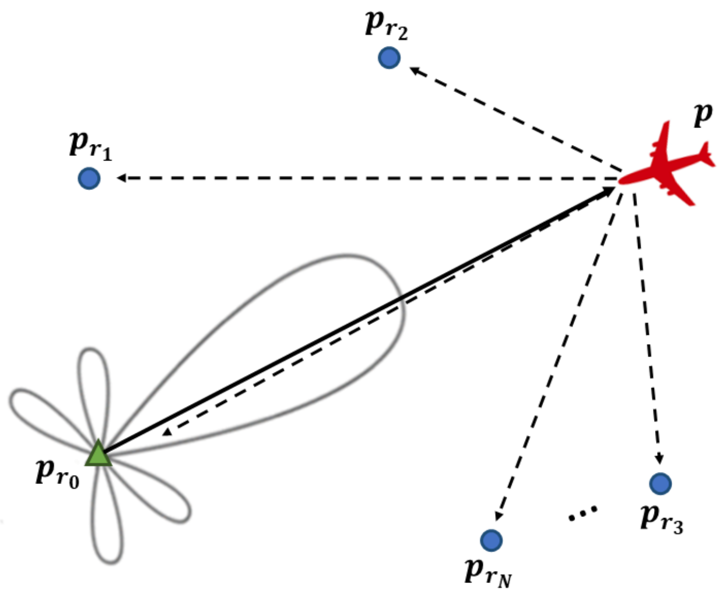

Figure 3.1. Pictorical representation of a surveillance system including a monostatic radar and N receiver nodes.

of generality, it is assumed coinciding with the reference system origin, i.e., $\boldsymbol{p}_{r_0} = [0, 0, 0]^T$);

- $\boldsymbol{p}_{r_i} = [x_{r_i}, y_{r_i}, z_{r_i}]^T \in \mathbb{R}^3$ the position of the i-th receiver, $i = 1, \ldots, N$.

Letting

$$\tilde{\tau}_i = \frac{1}{c}\left(\|\boldsymbol{p}\| + \|\boldsymbol{p} - \boldsymbol{p}_{r_i}\|\right), \qquad i = 0, \ldots, N \tag{3.1}$$

the noise-free propagation delay (with c the speed of light) associated with the i-th bistatic (or monostatic, if $i = 0$) pair, the following $N + 1$ noisy delay measurements are available at the i-th receiver, e.g., leveraging cross-correlation based processing,

$$\tau_i = \tilde{\tau}_i + n_i, \qquad i = 0, \ldots, N. \tag{3.2}$$

They are sent to the active radar that plays the role of a fusion node, to determine an estimate of the target position. In equations (3.2), $n_0, \ldots, n_N$ are statistically independent zero-mean (usually Gaussian distributed) random variables with variance $\sigma_0^2, \ldots, \sigma_N^2$ given by [60]

$$\sigma_i = \frac{1}{B\sqrt{2\mathrm{SNR}_i}}, \qquad i = 0, \ldots, N, \tag{3.3}$$

where B represents the frequency bandwidth of the active sensor transmitted waveform and SNR_i denotes the SNR of the i-th bistatic pair (i.e., radar/i-th receiver) or, if $i = 0$, of the monostatic radar, computed via the bistatic and monostatic radar range equation [61,70], respectively. It is worth pointing out that SNR_i depends on the distance between the target and the specific bistatic pair or monostatic radar and from the radar cross section of the target, which is unknown. Now, elaborating on equations (3.1), it is possible to get an equivalent form which is fundamental for the development of the proposed estimation algorithm. To this end, let

$$b_i = c\tilde{\tau}_i - \frac{c\tilde{\tau}_0}{2}, \qquad i = 1, \ldots, N,$$

and, for $i = 0$,

$$b_0 = \frac{c\tilde{\tau}_0}{2}.$$

Equation (3.1) can be recast as:

$$\begin{aligned} &\|\boldsymbol{p}\|^2 - 2x_p x_{r_i} - 2y_p y_{r_i} + \\ &- 2z_p z_{r_i} + \|\boldsymbol{p}_{r_i}\|^2 = b_i^2, \qquad i = 0, \ldots, N, \end{aligned}$$

which is equivalent to

$$\begin{cases} -2x_p x_{r_i} - 2y_p y_{r_i} - 2z_p z_{r_i} - g_i = 0 \\ g_i = b_i^2 - b_0^2 - x_{r_i}^2 - y_{r_i}^2 - z_{r_i}^2, \qquad i = 1, \ldots, N, \\ b_0 = \sqrt{x_p^2 + y_p^2 + z_p^2} \end{cases} \tag{3.4}$$

where it is assumed $b_i \geq 0$, $i = 1, \ldots, N$. All the relationships described in (3.4) can be grouped in a more compact matrix form as

$$\begin{cases} \boldsymbol{H}\boldsymbol{p} - \boldsymbol{g} = \boldsymbol{0} \\ \boldsymbol{p}^T\boldsymbol{p} = b_0^2 \end{cases} \tag{3.5}$$

where

$$\boldsymbol{H}^T = [\boldsymbol{h}_1, \boldsymbol{h}_2, \dots, \boldsymbol{h}_N] \in \mathbb{R}^{3,N},$$

with

$$\boldsymbol{h}_i = [-2x_{r_i}, -2y_{r_i}, -2z_{r_i}]^T \in \mathbb{R}^3, \; i = 1, \dots, N$$

and

$$\boldsymbol{g} = \left[g_1, \dots, g_N\right]^T \in \mathbb{R}^N,$$

with

$$g_i = b_i^2 - b_0^2 - x_{r_i}^2 - y_{r_i}^2 - z_{r_i}^2, \; i = 1, \dots, N.$$

3.1.1 Monostatic Acquisition System and Target Position Constraints

To perform the measurement process, the active radar employs an antenna characterized by a specific transmit/receive beampattern with a given main-lobe width and pointing direction, without loss of generality, coincident with the x-axis of the reference system. In this subsection, some constraints able to capitalize such *a priori* information are formalized with the goal of improving target positioning reliability. To this end, let us denote by:

- $\bar{\theta}$ and $\bar{\phi}$ the (half-side) antenna beamwidths in the $x-y$ and $x-z$ plane, respectively, as shown in Fig. 3.2;

- $\theta_p = \text{atan2}(y_p, x_p)$ and $\phi_p = \text{atan2}(z_p, x_p)$ the azimuth (in the $x-y$ plane) and elevation (in the $x-z$ plane) target angular coordinates, respectively.

Hence, let us observe that the limited main-lobe extension of the active radar demands the angular location of any illuminated target to comply with

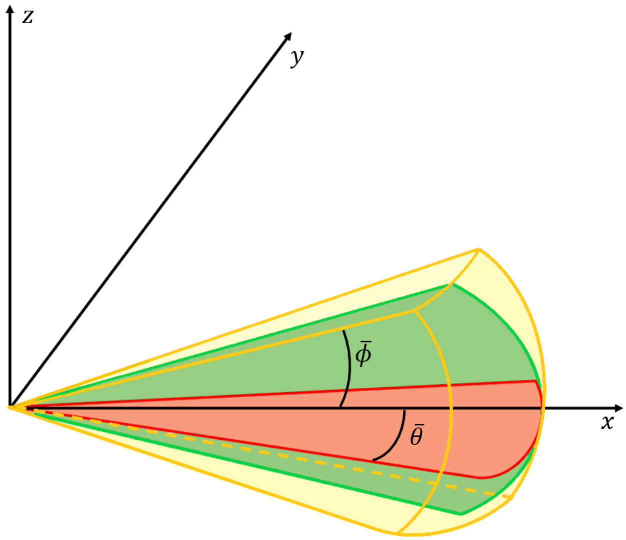

Figure 3.2. Representation of the antenna beamwidth.

$$\begin{cases} -\bar{\theta} \le \theta_p \le \bar{\theta} \\ -\bar{\phi} \le \phi_p \le \bar{\phi} \end{cases} . \tag{3.6}$$

The relationship (3.6) coupled with the assumptions $0 \le \bar{\theta} < \frac{\pi}{2}$ and $0 \le \bar{\phi} < \frac{\pi}{2}$, can be equivalently rewritten as

$$\begin{cases} -\tan\bar{\theta} \le \tan(\theta_p) \le \tan\bar{\theta} \\ -\tan\bar{\phi} \le \tan(\phi_p) \le \tan\bar{\phi} \end{cases} ,$$

which boils down to

$$\begin{cases} -x_p\gamma_a \le y_p \le x_p\gamma_a \\ -x_p\gamma_e \le z_p \le x_p\gamma_e \\ x_p \ge 0 \end{cases} , \tag{3.7}$$

where $\gamma_a = \tan\bar{\theta}$ and $\gamma_e = \tan\bar{\phi}$. It is worth pointing out that, with reference to a 2D problem, angular constraints have been also used in [62] for target localization with a passive radar and in [57, 66] to realize a passive radar positioning aided by some *a priori* information provided by an active radar sensing system.

3.2 Problem Formulation and 3D Localization Algorithm

This section deals with the formalization of the localization problem and the development of the resulting estimation technique. To this end, both model equations (3.5) and constraints (3.7), induced by the monostatic acquisition system[1], are exploited. In this respect, it is important to highlight that the vector $\boldsymbol{g}$ and the target range b_0 are corrupted by noise, and, consequently, the relationships in (3.5) are not exactly satisfied. This issue is handled resorting to the constrained LS framework by forcing the target range to be the projection of the noisy range measurement within the detected range-bin, and looking for the best fitting of the model to observations according to a squared norm cost function. Specifically, indicating the mentioned projection by $\bar{b}_0 = \max(\min(b_0, r_U), r_L)$, with r_L and r_U the extremes of the detected range-bin, the target positioning process can be formalized as the following non-convex optimization problem

$$\mathcal{P}\begin{cases} \min_{\boldsymbol{p}} \|\boldsymbol{H}\boldsymbol{p} - \boldsymbol{g}\|^2 & \\ \text{s.t.} \|\boldsymbol{p}\|^2 = \bar{b}_0^2 & \text{(3.8a)} \\ \quad -x_p\gamma_a \leq y_p \leq x_p\gamma_a & \text{(3.8b)} \\ \quad -x_p\gamma_e \leq z_p \leq x_p\gamma_e & \text{(3.8c)} \\ \quad x_p \geq 0 & \text{(3.8d)} \end{cases}$$

Although $\mathcal{P}$ is difficult to solve, through the use of optimization techniques based on KKT optimality [71] conditions, a quasi-closed-form (i.e., whose computation involves only elementary functions

[1] To lighten the notation, with a slight abuse of notation, the same symbols as in (3.5), where the quantities are noise-free, are used.

and roots of polynomial equations) optimal solution can be derived. Indeed, the following proposition holds true.

Proposition 3.2.1. *An optimal solution to $\mathcal{P}$ belongs to the following finite set of feasible points (whose cardinality is at most twenty-six):*

1. $\boldsymbol{x}^*(\bar{\lambda}_h) = \left(\boldsymbol{H}^T\boldsymbol{H} + \bar{\lambda}_h\boldsymbol{I}\right)^{-1}\boldsymbol{H}^T\boldsymbol{g}$, $h \in I_1 \subseteq \{1,\ldots,6\}$, *with* $\bar{\lambda}_h$ *the real-valued solutions to the sixth-order equation*

$$\boldsymbol{x}^*(\bar{\lambda})^T\boldsymbol{x}^*(\bar{\lambda}) = \bar{b}_0^2 \tag{3.9}$$

such that

$$\begin{cases} -\gamma_a x_p^*(\bar{\lambda}_h) < y_p^*(\bar{\lambda}_h) < \gamma_a x_p^*(\bar{\lambda}_h) \\ -\gamma_e x_p^*(\bar{\lambda}_h) < z_p^*(\bar{\lambda}_h) < \gamma_e x_p^*(\bar{\lambda}_h) \\ x_p^*(\bar{\lambda}_h) > 0 \end{cases} . \tag{3.10}$$

2. $\boldsymbol{x}^*(\beta_h^i) = [q_1^*(\beta_h^i), (-1)^{i+1}\gamma_a q_1^*(\beta_h^i), q_2^*(\beta_h^i)]^T, i = 1, 2$ *with*

$$\boldsymbol{q}^*(\beta_h^i) = \left(\boldsymbol{H}_i^{aT}\boldsymbol{H}_i^a + \beta_h^i\boldsymbol{B}^a\right)^{-1}\boldsymbol{H}_i^{aT}\boldsymbol{g}$$

where

$$\boldsymbol{H}_i^a = \boldsymbol{H}\begin{bmatrix} 1 & 0 \\ (-1)^{i+1}\gamma_a & 0 \\ 0 & 1 \end{bmatrix}, i = 1, 2,$$

$$\boldsymbol{B}^a = \begin{bmatrix} 1+\gamma_a^2 & 0 \\ 0 & 1 \end{bmatrix},$$

and β_h^i, $h \in I_2^i \subseteq \{1,\ldots,4\}$ *the real-valued solutions to the fourth-order equation*

$$\boldsymbol{q}^{*T}(\beta^i)\boldsymbol{B}^a\boldsymbol{q}^*(\beta^i) = \bar{b}_0^2 \tag{3.11}$$

such that

$$\begin{cases} -\gamma_e q_1^*(\beta_h^i) < q_2^*(\beta_h^i) < \gamma_e q_1^*(\beta_h^i) \\ q_1^*(\beta_h^i) > 0 \end{cases} . \tag{3.12}$$

3. $\boldsymbol{x}^*(\eta_h^i) = [p_1^*(\eta_h^i), p_2^*(\eta_h^i), (-1)^{i+1}\gamma_e p_1^*(\eta_h^i)]^T, i = 1, 2$ *with*

$$\boldsymbol{p}^*(\eta_h^i) = \left(\boldsymbol{H}_i^{eT}\boldsymbol{H}_i^e + \eta_h^i \boldsymbol{B}^e\right)^{-1} \boldsymbol{H}_i^{eT}\boldsymbol{g}$$

where

$$\boldsymbol{H}_i^e = \boldsymbol{H}\begin{bmatrix} 1 & 0 \\ 0 & 1 \\ (-1)^{i+1}\gamma_e & 0 \end{bmatrix}, i = 1, 2,$$

$$\boldsymbol{B}^e = \begin{bmatrix} 1+\gamma_e^2 & 0 \\ 0 & 1 \end{bmatrix},$$

and η_h^i, $h \in I_3^i \subseteq \{1, \ldots, 4\}$ *the real-valued solutions to the fourth-order equation*

$$\boldsymbol{p}^{*T}(\eta^i)\boldsymbol{B}^e\boldsymbol{p}^*(\eta^i) = \bar{b}_0^2 \tag{3.13}$$

such that

$$\begin{cases} -\gamma_a p_1^*(\eta_h^i) < p_2^*(\eta_h^i) < \gamma_a p_1^*(\eta_h^i) \\ p_1^*(\eta_h^i) > 0 \end{cases} . \tag{3.14}$$

4. $\boldsymbol{x}_{4_{i,j}}^* = \alpha\left[1, (-1)^{1+i}\gamma_a, (-1)^{1+j}\gamma_e\right]^T, (i, j) \in \{1, 2\}^2$, *with*

$$\alpha = \frac{\bar{b}_0}{\sqrt{1+\gamma_a^2+\gamma_e^2}}.$$

Proof. See Appendix B.1 □

In a nutshell, Proposition 3.2.1 defines the optimal candidate solutions to Problem $\mathcal{P}$. Precisely, each subset of solutions refers to a specific portion of the feasible target locations. A complete description of the global optimum search procedure is reported in Algorithm 2. It is worth observing that the determination of each subset of candidates requires the evaluation of the roots of a specific polynomial equation, whose efficient computation is discussed in the following subsection.

3.2.1 Evaluation of the Roots and Algorithm Computational Complexity

Algorithm 2 involves the solution of equations (3.9), (3.11), and (3.13). Guidelines and insights to the rooting process are now provided with reference to equation[2] (3.9). As shown in Appendix B.2 (the interested reader may refer to it for technical details and parameters definitions) solving equation (3.9) is tantamount to finding the real-valued roots[3] of

$$\sum_{j=1}^{3} \frac{|z_j|^2}{(\bar{\lambda}+\lambda_j)^2} - \bar{b}_0^2. \tag{3.15}$$

Evidently, each root of (3.15) must belong to one of the four subsets $\mathscr{I}_1 = (-\infty, -\lambda_3)$, $\mathscr{I}_2 = (-\lambda_3, -\lambda_2)$, $\mathscr{I}_3 = (-\lambda_2, -\lambda_1)$, and $\mathscr{I}_4 = (-\lambda_1, +\infty)$.

Now, being (3.15) strictly increasing (decreasing) over $\mathscr{I}_1$ ($\mathscr{I}_4$) with a range $(-\bar{b}_0^2, +\infty)$, a unique root exists within $\mathscr{I}_1$ ($\mathscr{I}_4$) and it can be found through the standard bisection method, as also depicted in [72].

In $\mathscr{I}_2$ ($\mathscr{I}_3$), instead, zero, one, or even two roots can exist, depending on the range of (3.15) over $\mathscr{I}_2$ ($\mathscr{I}_3$). Leveraging the strict convexity of (3.15), these points can be determined according to a

[2] Analogous considerations hold true for equations (3.11) and (3.13).
[3] In Appendix B.2, a normalized version of (3.15) is analyzed.

novel and *ad hoc* two-stage process involving at most three bisection loops each of them applied to either (3.15) or its derivative[4].

As discussed in Appendix B.2, the parameters of (3.15) can be computed via elementary functions applied to the entries of $(\boldsymbol{H}^T\boldsymbol{H})$, whose evaluation involves $\mathscr{O}(N^2)$ operations. Now, denoting by ϵ_0 the maximum size (among the different bisections) of the initial search interval (see Appendix B.2 for their determination) and by ϵ the desired accuracy level of any root, the number n of bisection iterations, in each search process, is upper bounded by:

$$n = \lceil \log_2 \left(\frac{\epsilon_0}{\epsilon} \right) \rceil.$$

Finally, each bisection cycle is performed with a computational complexity of $\mathscr{O}(1)$, being involved just elementary functions and comparisons. Hence, for a given accuracy ϵ, the roots search process entails $\mathscr{O}(1)$ operations, given $(\boldsymbol{H}^T\boldsymbol{H})$. It is worth pointing out that similar conclusions apply to the solution of equations (3.11) and (3.13).

Let us now deal with the computational complexity of **Algorithm 1**. Given the solutions to equations (3.9), (3.11), and (3.13), it mainly entails:

a) the evaluation of the resulting candidate optimal solutions, and

b) the computation of the corresponding objective values.

The former can be accomplished with a computational burden of $\mathscr{O}(1)$, being embroiled (as the most demanding operations) the evaluation of the inverse of the matrices $(\boldsymbol{H}^T\boldsymbol{H})$, $(\boldsymbol{H}_i^{aT}\boldsymbol{H}_i^a)$, and $(\boldsymbol{H}_i^{eT}\boldsymbol{H}_i^e)$, which are already calculated in the bisection processes.

The latter requires $\mathscr{O}(N)$ operations to evaluate the squared norms. As a result, the overall computational complexity of Algorithm 2 is $\mathscr{O}(N^2)$.

[4]It is worth observing that this novel strategy can be exploited by the procedure in [72] (in place of standard root search routines) to determine the possible roots belonging to the involved bounded intervals.

Algorithm 2 ARCE algorithm.

Input: $\bar{\theta}, \bar{\phi}, \tau_i, \boldsymbol{p}_{r_i}, \ i = 0, \ldots, N, \epsilon.$

Output: Target position estimate $[\hat{x}_p, \hat{y}_p, \hat{z}_p]^T$;

Parameter setup:

- Compute $\boldsymbol{H}, \boldsymbol{B}^a, \boldsymbol{B}^e, \boldsymbol{H}_i^a, \boldsymbol{H}_i^e, \ i = 1, 2, \ \bar{b}_0, \ \gamma_a, \gamma_e, \alpha.$

1. **Roots computation**
   - Find the roots (with the accuracy ϵ) $\bar{\lambda}_h, h \in I_1 \subseteq \{1, 2, \ldots, 6\}$ of equation (3.9) satisfying (3.10);
   - Find the roots (with the accuracy ϵ) $\beta_h^i, h \in I_2^i \subseteq \{1, 2, 3, 4\}, \ i = 1, 2$ of equation (3.11) satisfying (3.12);
   - Find the roots (with the accuracy ϵ) $\eta_h^i, h \in I_3^i \subseteq \{1, 2, 3, 4\}, \ i = 1, 2$ of equation (3.13) satisfying (3.14).
2. **Candidate points evaluation**
   - Compute $\boldsymbol{x}^*(\bar{\lambda}_h), \ \boldsymbol{x}^*(\beta_h^i), \ \boldsymbol{x}^*(\eta_h^i), \ \boldsymbol{x}^*_{4_{i,j}}, (i, j) \in \{1, 2\}^2.$
3. **Optimal solution selection**
   - Compute:
     - $v_j = \|\boldsymbol{H}\boldsymbol{x}^*(\bar{\lambda}_j) - \boldsymbol{g}\|, \ j = 1, \ldots, |I_1|$
     - $v_{|I_1|+j} = \|\boldsymbol{H}\boldsymbol{x}^*(\beta_j^1) - \boldsymbol{g}\|, \ j = 1, \ldots, |I_2^1|$
     - $v_{|I_1|+|I_2^1|+j} = \|\boldsymbol{H}\boldsymbol{x}^*(\beta_j^2) - \boldsymbol{g}\|, \ j = 1, \ldots, |I_2^2|$
     - $v_{|I_1|+|I_2^1|+|I_2^2|+j} = \|\boldsymbol{H}\boldsymbol{x}^*(\eta_j^1) - \boldsymbol{g}\|, \ j = 1, \ldots, |I_3^1|$
     - $v_{|I_1|+|I_2^1|+|I_2^2|+|I_3^1|+j} = \|\boldsymbol{H}\boldsymbol{x}^*(\eta_j^2) - \boldsymbol{g}\|, \ j = 1, \ldots, |I_3^2|$
     - $v_{|I_1|+|I_2^1|+|I_2^2|+|I_3^1|+|I_3^2|+j} = \|\boldsymbol{H}\boldsymbol{x}^*_{4_{j,1}} - \boldsymbol{g}\|, \ j = 1, 2$
     - $v_{|I_1|+|I_2^1|+|I_2^2|+|I_3^1|+|I_3^2|+2+j} = \|\boldsymbol{H}\boldsymbol{x}^*_{4_{j,2}} - \boldsymbol{g}\|, \ j = 1, 2.$
   - Determine $j^* = \arg\min_j v_j$ and pick up the corresponding solution, i.e.,

$$
\tilde{\boldsymbol{x}}^* = \begin{cases}
\boldsymbol{x}^*(\bar{\lambda}_{j^*}) & \text{if } 1 \leq j^* \leq |I_1| \\
\boldsymbol{x}^*(\beta^1_{j^*}) & \text{if } |I_1| + 1 \leq j^* \leq |I_1| + |I_2^1| \\
\boldsymbol{x}^*(\beta^2_{j^*}) & \text{if } |I_1| + |I_2^1| + 1 \leq j^* \leq |I_1| + |I_2^1| + |I_2^2| \\
\boldsymbol{x}^*(\eta^1_{j^*}) & \text{if } |I_1| + |I_2^1| + |I_2^2| + 1 \leq j^* \leq |I_1| + |I_2^1| + |I_2^2| + |I_3^1| \\
\boldsymbol{x}^*(\eta^2_{j^*}) & \text{if } |I_1| + |I_2^1| + |I_2^2| + |I_3^1| + 1 \leq j^* \leq |I_1| + |I_2^1| + |I_2^2| + |I_3^1| + |I_3^2| \\
\boldsymbol{x}^*_{4_{j^*,1}} & \text{if } |I_1| + |I_2^1| + |I_2^2| + |I_3^1| + |I_3^2| + 1 \leq j^* \leq |I_1| + |I_2^1| + |I_2^2| + |I_3^1| + |I_3^2| + 2 \\
\boldsymbol{x}^*_{4_{j^*,2}} & \text{otherwise}
\end{cases}
$$

Output: $[\hat{x}_p, \hat{y}_p, \hat{z}_p]^T = [\bar{x}_1^*, \bar{x}_2^*, \bar{x}_3^*]^T.$

3.3 Performance Analysis

Radiolocation systems composed of $N = 4$ and $N = 5$ receive-only sensors and one active radar are considered. Focusing first on the $N = 4$ case, the receiving nodes are located at $\boldsymbol{p}_{r_1} = [916, 941, 95]^T$ m, $\boldsymbol{p}_{r_2} = [973, 541, 764]^T$ m, $\boldsymbol{p}_{r_3} = [955, 483, 191]^T$ m, and $\boldsymbol{p}_{r_4} = [936, 350, 477]^T$ m.

Moreover, the measurement errors are modeled as zero-mean independent Gaussian random variables with standard deviations given in equations (3.3). Therein, the SNR of the $N = 4$ bistatic pairs (transmitter-receiver) and of the active radar are calculated as

$$\mathrm{SNR}_i = \frac{\overline{\mathrm{SNR}}_0}{\mathrm{LF}_i} \frac{\|\boldsymbol{q}_0\|^2}{\|\boldsymbol{p}\|^2} \frac{\|\boldsymbol{q}_0\|^2}{\|\boldsymbol{p} - \boldsymbol{p}_{r_i}\|^2}, i = 0, 1, \ldots, 4$$

where $\overline{\mathrm{SNR}}_0$ is a reference SNR computed via the monostatic radar range equation [61] at the nominal point $\boldsymbol{q}_0 = [20, 0, 0]^T$ km and $\mathrm{LF}_i, i = 0, \ldots, 4$, accounts for a loss factor due to different receive gains of the active sensor and the receive-only units. In particular, $\mathrm{LF}_0 = 0$ dB, while $\mathrm{LF}_i = 6$ dB, $i = 1, \ldots, 4$.

The performance of the developed localization algorithm is evaluated considering as a figure of merit the RMSE of the target position estimate, formally defined as $\sqrt{\mathbb{E}[\|\hat{\boldsymbol{p}} - \boldsymbol{p}\|^2]}$, where $\hat{\boldsymbol{p}}$ is the estimated position.

Since the RMSE does not present a closed-form expression, Monte Carlo simulation with 1000 independent trials is exploited. Additionally, the RCRLB[5], defined as $\sqrt{\mathrm{tr}(\mathrm{FIM}^{-1})}$, where FIM denotes the Fisher Information Matrix associated with the unknown parameters [74], is provided as performance benchmark. For comparison purposes, also the performance of some counterparts are illustrated.

Specifically, the performance of the procedures developed[6] in [30] and [75], denoted hereafter as TSE-1 and TSE-2, respectively, is

[5]Note that, based on [73, Lemma 4], for the estimation problem at hand the unconstrained CRLB coincides with the constrained CRLB, being $\gamma_a > 0$ and $\gamma_e > 0$.

[6]Their implementation for the 3D case with a transmitter co-located with one of the receivers at a known location is considered.

reported, along with two alternative methods for target positioning relying on model (3.5). The additional strategies are:

- U-TDOA-Like Estimator Unconstrained U-TDOA resorts to a standard LS framework and, assuming $\boldsymbol{H}$ full-rank, gives the following position estimate

$$\hat{\boldsymbol{p}}_{TDOA} = \arg\min_{\boldsymbol{p}\in\mathbb{R}^3} \|\boldsymbol{H}\boldsymbol{p} - \boldsymbol{g}\|^2 = \left(\boldsymbol{H}^T\boldsymbol{H}\right)^{-1}\boldsymbol{H}^T\boldsymbol{g}.$$

- Range-Only Constrained Estimator (ROCE) Giving up the main-lobe constraint, the estimation problem can be framed as

$$\mathcal{P}\begin{cases}\min\limits_{\boldsymbol{p}} \|\boldsymbol{H}\boldsymbol{p} - \boldsymbol{g}\|^2 \\ \text{s.t.} \|\boldsymbol{p}\|^2 = \bar{b}_0^2\end{cases}$$

  and the resulting position can be retrieved as

$$\hat{\boldsymbol{x}} = \arg\min_{i\in I_1} \|\boldsymbol{H}\boldsymbol{x}_i^* - \boldsymbol{g}\|^2$$

  where

$$\begin{aligned}&\boldsymbol{x}_i^* = \boldsymbol{x}^*(\bar{\zeta}_i) = \left(\boldsymbol{H}^T\boldsymbol{H} + \bar{\zeta}_i\boldsymbol{I}\right)^{-1}\boldsymbol{H}^T\boldsymbol{g},\\ &i \in I_1 \subseteq \{1,\dots,6\},\end{aligned}$$

  with $\bar{\zeta}_i$ the real-valued solutions to the sixth-order equation

$$\boldsymbol{x}^*(\bar{\zeta})^T\boldsymbol{x}^*(\bar{\zeta}) = \bar{b}_0^2.$$

Notably, the computational complexity of all the considered competitors is substantially $\mathcal{O}(N^2)$. In the considered numerical analysis, the target is positioned at $[r\cos\theta_p\cos\phi_p, r\sin\theta_p\cos\phi_p, r\sin\phi_p]^T$, with $r = 20$ km and different values of θ_p and ϕ_p are considered, i.e., $(\theta_p, \phi_p) \in \{(0°, 0°), (4°, 0°), (6.9°, 4.9°)\}$. Furthermore, the main-beam width in azimuth and elevation for the monostatic radar are $\bar{\theta} = 7°$ and $\bar{\phi} = 5°$, respectively. Finally, the transmit signal bandwidth is equal to $B = 2$ MHz. The considered target positions along with the

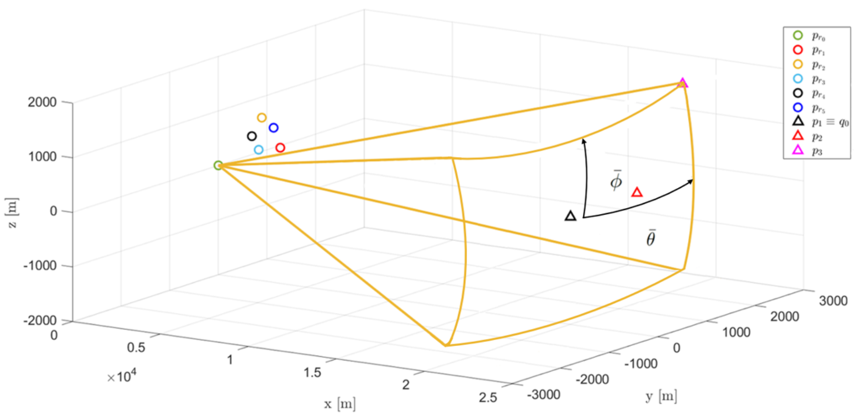

Figure 3.3. Geometric configuration of the radiolocation system and target location scenarios. In the figure legend, $\boldsymbol{p}_1$, $\boldsymbol{p}_2$, and $\boldsymbol{p}_3$ are the considered target positions, located at range $r = 20$ km and with azimuth-elevation $(0°, 0°)$, $(4°, 0°)$, and $(6.9°, 4.9°)$, respectively.

radiolocation system and the radar main-lobe radiation pattern are displayed in Fig. 3.3.

In Fig. 3.4, the RMSE versus $\overline{\mathrm{SNR}}_0$ is illustrated, where each subfigure refers to a specific scenario for the target position. Inspection of Fig. 3.4 shows that the devised estimator achieves some performance gains in comparison with the counterparts, for $\overline{\mathrm{SNR}}_0$ ranging from 0 to 20 dB, clearly revealing the effectiveness of the new procedure to capitalize on the available *a priori* knowledge about the beampattern features. Fig. 3.5 shows the estimation behaviour of the different localization algorithms when $(\theta_p, \phi_p) = (0°, 0°)$ in logarithmic scale, in order to provide increased visibility of the performance. In this respect, it is also worth highlighting that the RMSE levels achieved by ARCE are very close to the RCRLB and at low $\overline{\mathrm{SNR}}_0$ even smaller values than the benchmark are observed, indicating that the proposed estimator exhibits a bias under this SNR regime.

From the results displayed in Figs. 3.4(a)-(b)-(c) it is also evident that ROCE, TSE-1, and TSE-2 (which are the major competitors for ARCE) attain performance levels comparable with the new proposed

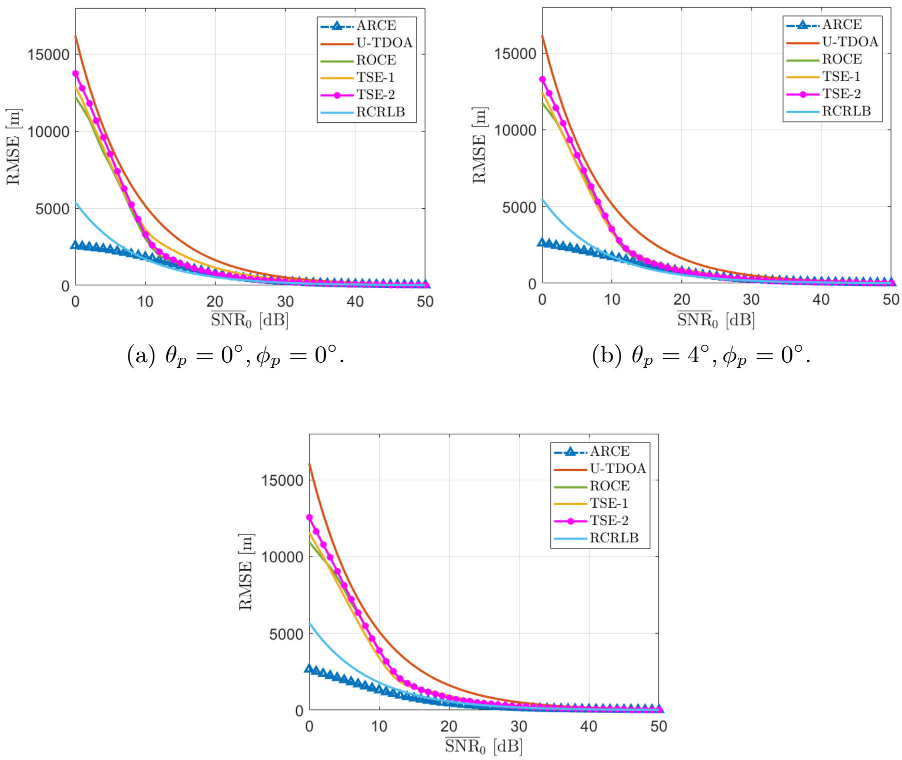

(a) $\theta_p = 0°, \phi_p = 0°$.

(b) $\theta_p = 4°, \phi_p = 0°$.

(c) $\theta_p = 6.9°, \phi_p = 4.9°$

Figure 3.4. RMSE versus $\overline{\mathrm{SNR}}_0$, when $\bar{\theta} = 7°$, $\bar{\phi} = 5°$, and the radiolocation system comprises $N = 4$ receive-only sensors.

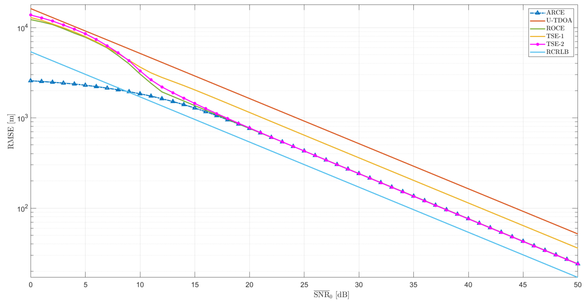

Figure 3.5. RMSE in algorithmic scale versus $\overline{\mathrm{SNR}}_0$, when $\bar{\theta} = 7°$, $\bar{\phi} = 5°$, $\theta_p = 0°$, $\phi_p = 0°$, and the radiolocation system comprises $N = 4$ receive-only sensors.

localization algorithm for ever greater values of $\overline{\mathrm{SNR}}_0$ as the target distance from the antenna's pointing direction increases.

This behaviour is not surprising since the beampattern extent constraint is more valuable when the target is closer and closer to the main-lobe boundary. These insights are confirmed by the plots in Fig. 3.4(c) pinpointing that the proposed estimator achieves its best performance when $(\theta_p, \phi_p) = (6.9°, 4.9°)$.

As a further confirmation of the effectiveness of the devised localization procedure, the square RAMSE — where the average is with respect to the target position is analyzed — in Table 3.1, for different values of $\overline{\mathrm{SNR}}_0$ i.e., $\overline{\mathrm{SNR}}_0 \in \{0, 5, 10, 15\}$ dB, and target range $r = 20$ km. A uniform 2D grid of points is considered for the target angular locations, where both the azimuth and the elevation are discretized in ten angular locations, i.e., $\theta_p = \{\Delta_\theta i,\ i = 0, \ldots, 9\}$ and $\phi_p = \{\Delta_\phi i,\ i = 0, \ldots, 9\}$, with $\Delta_\theta = 6.9°/9$ and $\Delta_\phi = 4.9°/9$. The ARCE performance in terms of RAMSE is uniformly superior over the counterparts, with relevant gains, especially at low SNR.

To assess the computational complexity of ARCE, U-TDOA, ROCE, TSE-1, and TSE-2, Tables 3.2, 3.3, and 3.4 report the average times (with respect to Monte Carlo trials) required by the mentioned strategies to calculate the target position estimate. Different scenarios are analyzed, i.e., $(\theta_p, \phi_p) \in \{(0°, 0°), (4°, 0°), (6.9°, 4.9°)\}$ and

Table 3.1. RAMSE values, $\bar{\theta} = 7°$, $\bar{\phi} = 5°$, and $N = 4$.

$\overline{\mathrm{SNR}}_0$	ARCE	U-TDOA	ROCE	TSE-1	TSE-2
0 dB	2.6×10^3 m	1.6×10^4 m	1.2×10^4 m	1.2×10^4 m	1.3×10^4 m
5 dB	2.2×10^3 m	9.1×10^3 m	7.8×10^3 m	7.7×10^3 m	8.3×10^3 m
10 dB	1.6×10^3 m	5.1×10^3 m	3.5×10^3 m	3.4×10^3 m	3.6×10^3 m
15 dB	1.1×10^3 m	2.9×10^3 m	1.4×10^3 m	1.5×10^3 m	1.5×10^3 m

Table 3.2. Average execution times, $\theta_p = 0°$, $\phi_p = 0°$, $\bar{\theta} = 7°$, $\bar{\phi} = 5°$, and $N = 4$.

$\overline{\mathrm{SNR}}_0$	ARCE	U-TDOA	ROCE	TSE-1	TSE-2
0 dB	4.1 ms	0.063 ms	1.3 ms	0.64 ms	0.25 ms
5 dB	4.3 ms	0.087 ms	1.3 ms	0.39 ms	0.19 ms
10 dB	8.0 ms	0.070 ms	2.0 ms	0.72 ms	0.30 ms
15 dB	3.5 ms	0.30 ms	1.3 ms	0.32 ms	0.16 ms

$\overline{\mathrm{SNR}}_0 \in \{0, 5, 10, 15\}$ dB.

As expected, the computational time of ARCE is larger than that of U-TDOA and ROCE methods (being U-TDOA and ROCE optimization problems easier to solve). Furthermore, ARCE requires a larger execution time also with respect to TSE-1 and TSE-2; this is mainly due to the non-optimized MATLAB implementation of the bisection algorithms, which is well-known to perform inefficiently in presence of loops.

The computational time of the overall rooting process can sensibly be improved adopting a parallelized implementation, over the different search intervals. The analysis of the aforementioned efficient strategy will be carried out in a future work. With the current implementation it is worthwhile to stress that often the ARCE computational time is comparable with ROCE, in the sense that in the worst case ARCE is 10 ms and ROCE is 2 ms, while in the best case ARCE is 2.9 ms and ROCE is 1.1 ms. However, the difference in terms of accuracy can easily reach one order of magnitude in favor of ARCE at low SNR.

In Figs. 3.6 the RMSE is analyzed assuming the scenario of Figs. 3.4

Table 3.3. Average execution times, $\theta_p = 4°$, $\phi_p = 0°$, $\bar{\theta} = 7°$, $\bar{\phi} = 5°$, and $N = 4$.

$\overline{\mathrm{SNR}}_0$	ARCE	U-TDOA	ROCE	TSE-1	TSE-2
0 dB	6.3 ms	0.21 ms	1.6 ms	0.58	0.18 ms
5 dB	10 ms	0.22 ms	1.6 ms	0.86 ms	0.26 ms
10 dB	6.2 ms	0.19 ms	1.4 ms	0.47 ms	0.23 ms
15 dB	7.1 ms	0.23 ms	1.5 ms	0.63 ms	0.27 ms

Table 3.4. Average execution times, $\theta_p = 6.9°$, $\phi_p = 4.9°$, $\bar{\theta} = 7°$, $\bar{\phi} = 5°$, and $N = 4$.

$\overline{\mathrm{SNR}}_0$	ARCE	U-TDOA	ROCE	TSE-1	TSE-2
0 dB	5.1 ms	0.092 ms	1.2 ms	0.73 ms	0.54 ms
5 dB	6.3 ms	0.098 ms	1.1 ms	0.91 ms	0.49 ms
10 dB	3.2 ms	0.11 ms	1.1 ms	0.44 ms	0.35 ms
15 dB	2.9 ms	0.32 ms	1.7 ms	0.41 ms	0.22 ms

and an additional receive unit located at $\boldsymbol{p}_{r_5} = [760, 860, 477]^T$ m. Inspection of the figures corroborates the merits of the proposed algorithm with respect to the counterparts. As expected, all the considered procedures provide better estimates than the case of Figs. 3.4 with $N = 4$. To gather further insights about the impact of the number of receivers on the proposed technique, in Fig. 3.7 the RMSE of the devised localization method is displayed versus the $\overline{\mathrm{SNR}}_0$, for $N = 4$ and $N = 5$. As expected, the results in Fig. 3.7 highlight that the presence of the additional receiver can grant a performance improvement ranging between 100 and 400 meters, for $\overline{\mathrm{SNR}}_0$ values from 0 to 20 dB.

The case of a wider main-lobe width is considered in Fig. 3.8, where $\bar{\theta} = 10°$ and $\bar{\phi} = 7°$. The performance in terms of RMSE for the ARCE estimator is plotted versus the elevation angle ϕ_p, for three values of the target azimuth. The curves show that the proposed algorithm provides more accurate estimates when $\theta_p = 9.9°$, as compared with $\theta_p = 0°$ and $\theta_p = 4°$. It is worth mentioning that the performance improves as ϕ_p increases regardless of θ_p. This behavior

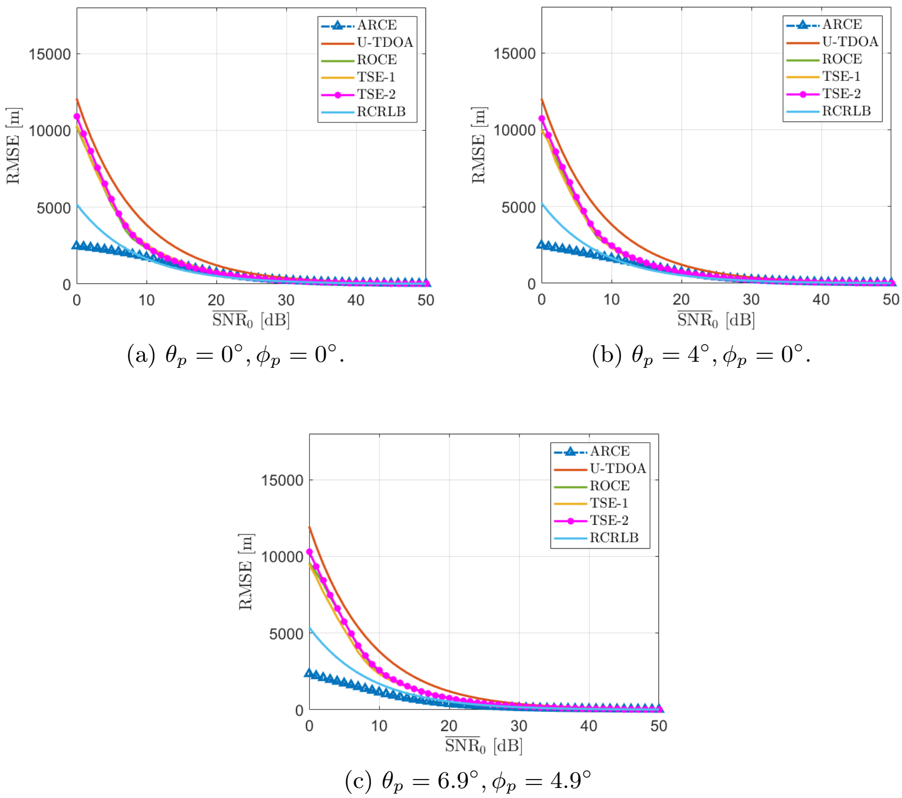

(a) $\theta_p = 0°, \phi_p = 0°$.

(b) $\theta_p = 4°, \phi_p = 0°$.

(c) $\theta_p = 6.9°, \phi_p = 4.9°$

Figure 3.6. RMSE versus $\overline{\mathrm{SNR}}_0$, when $\bar{\theta} = 7°$, $\bar{\phi} = 5°$, and the radiolocation system comprises $N = 5$ receive-only sensors.

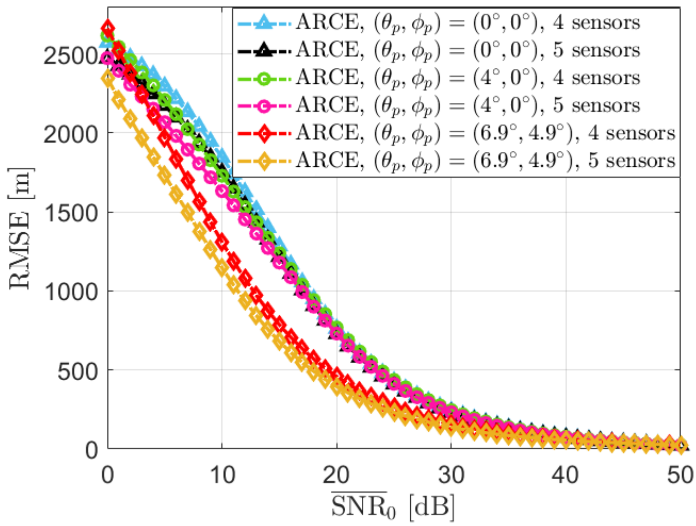

Figure 3.7. RMSE versus $\overline{\mathrm{SNR}}_0$, when $\bar{\theta} = 7°$, $\bar{\phi} = 5°$, and the radiolocation system comprises $N = 4$ and $N = 5$ receive-only sensors.

confirms that the estimation error decreases when the target is closer to the boundary of the angular region.

In Fig. 3.9 the localization capabilities are analyzed when the radar antenna pointing direction rotates in the $x - y$ plane, assuming $\overline{\mathrm{SNR}}_0 = 10$ dB. The target is supposed fixed and centered in the radar beam, regardless of the pointing direction. This case study allows to evaluate one of the main skills of interest that such a multistatic radar network presents, i.e., the geometric diversity provided by the system, which depends on the spatial configuration of the receiver nodes with respect to the active radar main beam direction.

The curves in Fig. 3.9 pinpoint that ARCE strategy is sensibly more accurate and robust than the alternative methods, especially in comparison with TSE-1. Indeed, the improvement is observed for all the rotation angles.

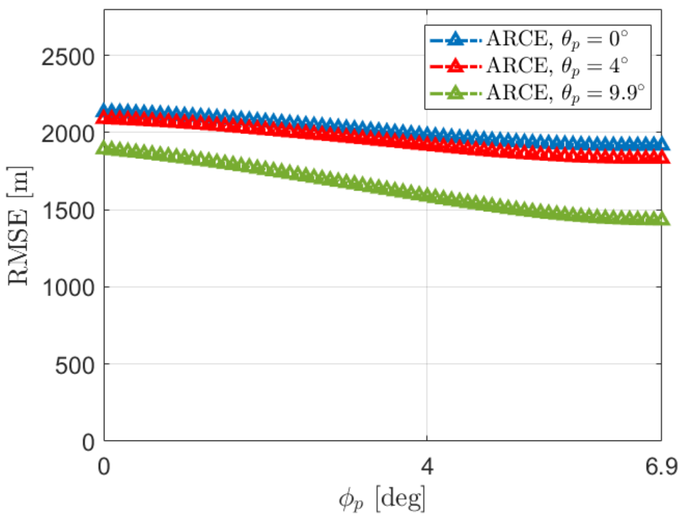

Figure 3.8. RMSE versus ϕ_p, for $\overline{\mathrm{SNR}}_0 = 10$ dB, when $\bar{\theta} = 10°$, $\bar{\phi} = 7°$, and the radiolocation system comprises $N = 4$ receive-only sensors.

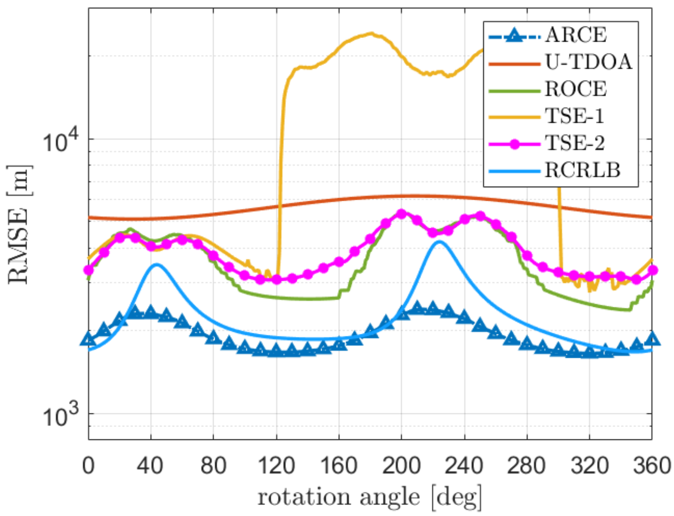

Figure 3.9. RMSE versus radar pointing direction, for $\overline{\mathrm{SNR}}_0 = 10$ dB, when $\bar{\theta} = 10°$, $\bar{\phi} = 7°$, and the radiolocation system comprises $N = 4$ receive-only sensors.

Chapter 4

Multitarget Localization and Tracking for Multiplatform Radar Network

This chapter illustrates a solution to combine the ARCE [69] localization method described in Chapter 3 and the SPA-based MTT approach of [55, 56]. Specifically, a particle enrichment process using ARCE localization estimate is introduced within the SPA-based MTT in order to have a more effective sampling of the target state space. Angular constraints are forced such that the localization process exploits the available information about both the antenna beamwidth of the transmitter and the virtual beamwidth obtained from the target predicted uncertainty. Hence, the particle enrichment process replaces a subset of predicted particles with a new set of particles drawn from a distribution whose parameters depend on the ARCE localization estimate.

Experiments[1] are presented to analyze the proposed algorithm in comparison with the conventional baseline SPA-based MTT and the stand-alone ARCE localization, in a 3D sensing scenario.

[1] I would like to acknowledge Dr. Giovanni Soldi and Dr. Domenico Gaglione from the NATO STO Centre for Maritime Research and Experimentation (CMRE), La Spezia, Italy, for the fruitful collaboration in the achievement of the results in this chapter.

4.1 MTT Algorithms for MPRNs

4.1.1 Objective and Challenges

MTT algorithms aim at sequentially estimating — across multiple time scans — the *states*, i.e., positions and velocities, of multiple targets by exploiting both the measurements generated by multiple sensors and an *a priori* knowledge on the target dynamics. Let us denote with $\boldsymbol{s}_{k,1}, \ldots, \boldsymbol{s}_{k,L}$ the unknown states of L targets at time k, where $\boldsymbol{s}_{k,\ell} \triangleq [\boldsymbol{p}_{k,\ell}^T, \boldsymbol{v}_{k,\ell}^T]^T$, and $\boldsymbol{p}_{k,\ell}$ and $\boldsymbol{v}_{k,\ell}$ are 3D position and 3D velocity, respectively, of the ℓ-th target.[2] An MPRN comprising a single transmitter $\boldsymbol{p}_{t_k}$ and S receivers $\boldsymbol{p}_{r_k}^{(i)}$ with the receiver labeled $i = 1$ co-located with the transmitter is considered. Unlike the previous chapter though, here the presence of multiple measurements at each receiver is accounted. Specifically, receiver i produces $M_k^{(i)} \geqslant 0$ range measurements at time k, due to both the presence of multiple targets and clutter. At time k, each target ℓ either does not generate any measurement at receiver i, i.e., it is missed detected by receiver i, or it can generate the m-th measurement $\rho_{k,m}^{(i)}$ at receiver i, i.e., it is detected by receiver i, with probability $P_{\mathrm{d}}^{(i)}$. If the m-th measurement $\rho_{k,m}^{(i)}$ at receiver i is generated by the ℓ-th target then it is modeled as

$$\rho_{k,m}^{(i)} = \|\boldsymbol{p}_{k,\ell} - \boldsymbol{p}_{t_k}\| + \|\boldsymbol{p}_{k,\ell} - \boldsymbol{p}_{r_k}^{(i)}\| + n_{k,m}^{(i)}, \tag{4.1}$$

where $w_{k,m}^{(i)}$ are zero-mean (usually Gaussian distributed) random variables independent across k, i, and m. It is worth noting that the measurement only depends on the target's position $\boldsymbol{p}_{k,\ell}$ and not on its velocity $\boldsymbol{v}_{k,\ell}$, which remain unobserved and can only be inferred if the target's dynamics is taken into account.

The presence of multiple targets and the availability of multiple measurements — some of which might be clutter-generated (i.e., false alarms) — is the cause of the MOU problem, i.e., the unknown

[2] Higher order kinematics might be included in the target state, i.e., acceleration and jerk, depending on the modeling of the target dynamics.

association of measurements with targets, whose complexity scales exponentially with the number of targets, sensors, and measurements. Indeed, even considering a single sensor with no false alarm, and assuming that each target may generate *at most* one measurement,[3] known as point-target assumption [76, Sec. 2.3], the number of possible associations between the L targets and the $M_k^{(i)}$ measurements is $L!/(L-M_k^{(i)})!$. As an example, consider a case with $L = 4$ targets and $M_k^{(i)} = 2$ measurements: the number of possible associations is 12. Adding one more target and one more measurement, the number of associations becomes 60. Clearly, the number of associations also increases if measurements may stem from false alarms [77].

Up to this point the number of targets, L, has been assumed time-invariant, either known or unknown. For many tracking scenarios, however, this assumption does not hold. Indeed, targets may enter the field-of-view of the sensors or, in other words, *appear* in the tracking scenario; because of this, not-associated measurements are not necessarily false alarms, but they might be raised by newly observed targets. Likewise, targets may leave the coverage area, or *disappear* from the tracking scenario, thus not generating any more measurements at the sensors. In these cases, the number of targets L_k needs to be modeled as time-variant and, if unknown, can be estimated alongside the target states. Several approaches can be used to handle these appearance and disappearance phases, known as track formation or initialization, and track termination [76, Sec. 3.3].

4.1.2 SPA-based Multisensor MTT Algorithm

The issue of computational complexity and scalability of state-of-the-art MTT methods is well addressed by a recent and innovative particle-based Bayesian MTT approach, which relies on the use of a factor graph and the SPA [55, 56, 78–81]. The factor graph is used to represent the statistical dependencies among the random variables of the MTT model, while the Bayesian inference is efficiently

[3] In general, when a target does not produce any measurement at a given receiver, it is considered *missed detected* at that receiver.

and reliably approximated by the SPA. This technique is able to exploit conditional independence properties of random variables to achieve a drastic reduction of the computational complexity, handling efficiently both the data association and the fusion of measurements from multiple receivers — even heterogeneous [81]. In this respect, the SPA enables an efficient calculation of association probabilities for *soft*[4] target-measurement associations. For this reason the SPA-based MTT method is particularly suitable for large-scale MPRNs tracking scenarios involving a large number of targets, receivers, and measurements, and enabling its use on resource-limited devices.

To account for the estimation of both the number of targets and their states, the state of each target $\boldsymbol{s}_{k,\ell}$ is augmented by a Bernoulli random variable $r_{k,\ell}$ that is equal to 1 if the target is present, and 0 otherwise; consequently, L_k represents the number of *potential* or tentative targets. The Bayesian inference about the presence and the state of potential target ℓ at time k is then based on the joint posterior pdf $f(\boldsymbol{s}_{k,\ell}, r_{k,\ell}|\boldsymbol{\rho}_{1:k})$, where $\boldsymbol{\rho}_{1:k}$ is the vector comprising all the measurements from all the receivers since the initial time up to the current time k. Specifically, the existence of potential target ℓ is confirmed if the marginal posterior probability mass function (pmf) $p(r_{k,\ell} = 1|\boldsymbol{\rho}_{1:k})$ is above a prefixed threshold[5] P_{th} [82, Ch. 2], and an estimate of the potential target's state is obtained from the marginal posterior pdf $f(\boldsymbol{s}_{k,\ell}|r_{k,\ell} = 1, \boldsymbol{\rho}_{1:k})$ through, for example, the minimum mean square error estimator. Note that these marginal posterior pdf/pmf can be obtained from the joint posterior pdf above by simple elementary operations, including marginalization. The SPA-based MTT algorithm computes an approximated version of the joint posterior pdf — called *belief* — for all the potential targets

[4]A single-sensor MTT algorithm that uses a *soft* data association technique does not select a specific measurement to update a target's state; it rather updates the target's state by averaging over all possible target-measurement combinations suitably weighted by their association probabilities. Conversely, with a *hard* data association technique a single-sensor MTT algorithm updates a target's state with a single measurement, selected as the one maximizing the association probability [76, Sec. 2.4].

[5]The *estimated* number of targets is the cardinality of the set $\{\ell : p(r_{k,\ell} = 1|\boldsymbol{\rho}_{1:k}) > P_{\text{th}}\}$.

by employing an iterative version of the SPA on a suitably devised factor graph [56]; for future reference, the belief approximating the joint posterior pdf for potential target ℓ at time k is referred to as $\tilde{f}(\boldsymbol{s}_{k,\ell}, r_{k,\ell})$. The complexity of the SPA-based MTT algorithm scales only quadratically in the number of potential targets, linearly in the number of transmitter-receiver pairs, and linearly in the number of measurements per receiver, and outperforms previously proposed methods in terms of accuracy [55,56,80]. Finally, since the SPA-based MTT method uses a particle-based implementation, it is potentially suitable for arbitrary non-linear and non-Gaussian problems [55, 56, 78–81].

In the following section combination of the ARCE localization method described in Chapter 3 with the SPA-based MTT approach is illustrated.

4.2 Combination of the ARCE Localization with the SPA-based MTT Algorithm

The SPA-based MTT algorithm has shown its advantages in terms of both accuracy and computational complexity compared to alternative approaches. Nonetheless, its computational burden can rapidly grow in a 3D scenario, because of the high number of particles required to effectively sample the 6D potential target state space. The use of a limited number of particles is thus desired, which, however, can lead to particle degeneracy and impoverishment,[6] and more generally to an inaccurate representation of the pdfs/beliefs. This is particularly relevant in the range-only sensing context considered in this work, when initializing the state of a newly observed target from a bistatic measurement at the single receiver node.

Indeed, the lack of any angle information requires the prior `pdf` of the potential target state, in particular the component related to the

[6] *Degeneracy* occurs when, over time, most of the weight of the entire set of particles is concentrated on few particles, whereas the remaining particles have a negligible weight. This effect is generally addressed through resampling, which however might cause particle *impoverishment*, that is, a reduction of particle diversity [83].

3D position, to cover a large volume, potentially the entire focaloid induced by the bistatic range measurement as well as transmitter and receiver positions;[7] clearly, the resulting prior pdf cannot be reliable represented by a small number of particles. Moreover, both an inaccurate prior distribution choice and its rough representation can propagate via the target dynamic over time, degrading the overall tracking performance.

Inspired by the rationale behind the ARCE localization, here the aim is to capitalize on some prior angular information, related to the potential target position, in order to mitigate the negative effects caused by the use of a limited number of particles, and thus improve the tracking performance. The angular side information can be acquired either through physical considerations, e.g., the antenna beamwidth of the transmitter as in the plain ARCE strategy, or leveraging the knowledge about the predicted distribution of the potential target state. Thus, a particles enrichment process within the SPA-based MTT algorithm that enables a smarter sampling of the potential target state space is proposed; this process is driven by the ARCE location estimate, which is substantially memoryless, i.e., unaffected by the past, and mainly depends on the measurements available at current time.

Fig. 4.1 shows the steps of the proposed ARCE-enhanced SPA-based MTT algorithm. The beliefs computed at the previous time scan $k-1$, representative of the potential targets observed so far, are predicted to current time k by means of a kinematic model. Meanwhile, new potential target states are initialized so that newly observed targets, i.e., targets recently appeared, are promptly tracked. Ideally, this initialization should involve the measurements collected by all the receivers at current time k, procedure that demands a high computational cost.

As an example, let us consider $S = 2$ receivers each with a single measurement, that is, $M_k^{(i)} = 1$ for $i = 1, 2$. Both measurements can be false alarms or be generated by the same newly observed

[7] A *focaloid* is a shell bounded by two confocal ellipsoids; it reduces to a *spherical shell* when transmitter and receiver are co-located.

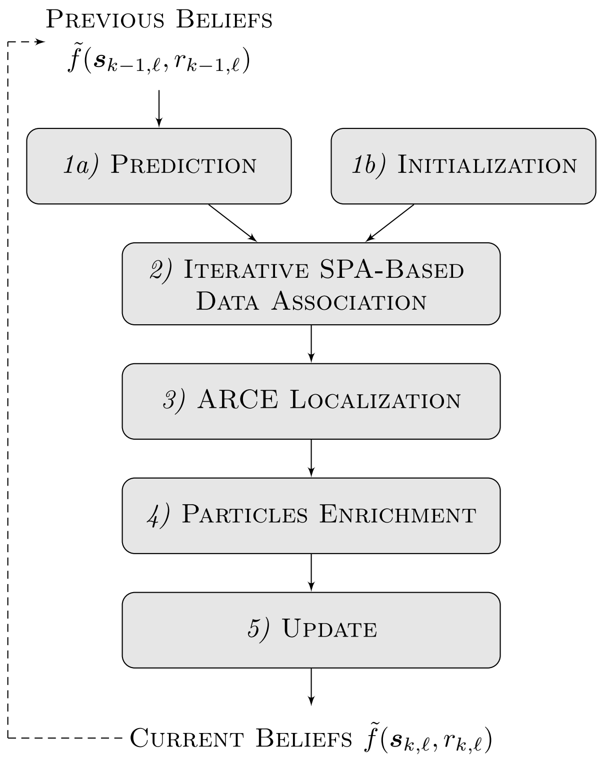

Figure 4.1. Block diagram reporting the steps of the proposed ARCE-enhanced SPA-based MTT algorithm performed at time k.

target; or each measurement can be generated by different newly observed targets; or the measurement from the first receiver can be generated by a newly observed target while the other be a false alarm, and vice versa. As seen, even in this simple case with only two measurements from two receivers, the initialization step should account for five different scenarios. Therefore, in order to limit the complexity, only measurements from one of the receivers are considered for the initialization step; specifically, the $M_k^{(1)}$ measurements collected by the monostatic active radar (i.e., the receiver labeled $i = 1$ co-located with the transmitter), since this sensor is more reliable, in terms of detectability, compared to the other passive receivers. Then, the iterative SPA-based data association procedure computes the *soft* association probabilities for each potential target-measurement combination. These association probabilities are used as they are in the update step, according to the common SPA-based MTT framework [56], and are transformed into *hard* potential target-measurement association in order to cluster the measurements and accomplish single-snapshot ARCE localization based of each group.

The ARCE localization algorithm leverages also some prior angular information to compute a potential target's position estimate. Two approaches are herein pursued, based on how this information is acquired. The *non-adaptive* (NAD) approach uses the physical beamwidth and looking direction of the active radar antenna to establish the angular constraints; hence, these constraints are time-invariant and equal for all the potential targets. The *adaptive* (AD) counterpart exploits an appropriate *virtual beam* to define bespoke angular constraints in the ARCE process. This virtual beam is unique for each potential target, and is given by the intersection of the active antenna beam and a tailored beam: the latter points towards the potential target's predicted position, and its beamwidth is proportional to the uncertainty of such predicted position.

The last two steps refer to the particles enrichment, used to obtain a smarter sampling of the potential target state space based on the ARCE localization estimates, and the update step used to eventually obtain the beliefs at current time. Hereafter, a detailed description of each step performed at time k is provided.

4.2.1 Prediction and Initialization

The input to the prediction step is the set of L_{k-1} previous beliefs $\tilde{f}(\boldsymbol{s}_{k-1,\ell}, r_{k-1,\ell})$, $\ell \in \{1, \ldots, L_{k-1}\}$, representing the joint posterior pdfs $f(\boldsymbol{s}_{k-1,\ell}, r_{k-1,\ell}|\boldsymbol{\rho}_{1:k-1})$ computed at time $k-1$. Following the derivation in [55, Sec. VI], the previous belief of potential target ℓ for $r_{k-1,\ell} = 1$, i.e., $\tilde{f}(\boldsymbol{s}_{k-1,\ell}, r_{k-1,\ell} = 1)$, is represented by a set of N_p weighted particles[8] $\{\boldsymbol{s}^{(p)}_{k-1|k-1,\ell}, \omega^{(p)}_{k-1|k-1,\ell}\}_{p=1}^{N_\mathrm{p}}$, whose weights, contrary to conventional particle filtering [84], do not sum to one. Indeed, it is straightforward to verify that $p^{\mathrm{e}}_{k-1|k-1,\ell} \triangleq \sum_{p=1}^{N_\mathrm{p}} \omega^{(p)}_{k-1|k-1,\ell}$ is approximately equal to $p(r_{k-1,\ell} = 1|\boldsymbol{\rho}_{1:k-1})$, i.e., the posterior probability of existence of potential target ℓ at time $k-1$. During the prediction step, this set of weighted particles is converted into a new set of weighted particles $\{\boldsymbol{s}^{(p)}_{k|k-1,\ell}, \omega^{(p)}_{k|k-1,\ell}\}_{p=1}^{N_\mathrm{p}}$, that approximates the joint predicted pdf $f(\boldsymbol{s}_{k,\ell}, r_{k,\ell}|\boldsymbol{\rho}_{1:k-1})$. Specifically, $\omega^{(p)}_{k|k-1,\ell} = p^{\mathrm{s}}\omega^{(p)}_{k-1|k-1,\ell}$, where p^{s} is the target surviving probability. Besides, such a particles evolution is achieved by utilizing an appropriate kinematic model, described by the transition pdf $f(\boldsymbol{s}_{k,\ell}|\boldsymbol{s}_{k-1,\ell})$.

Meanwhile, as mentioned above, new potential target states are initialized to account for newly observed targets. Let us recall that, in order to limit the computational cost, only the $M_k^{(1)}$ measurements produced by the monostatic active radar are used in the initialization step; precisely, a set of weighted particles $\{\boldsymbol{s}^{(p)}_{k|k-1,m'}, \omega^{(p)}_{k|k-1,m'}\}_{p=1}^{N_\mathrm{p}}$, with $m' = L_{k-1} + m$, is added[9] for each measurement $m \in \{1, \dots, M_k^{(1)}\}$. The 3D position component of each particle, i.e., $\boldsymbol{p}^{(p)}_{k|k-1,m'}$, is drawn from a distribution — usually Gaussian, according to the measurement model in equations (4.1) — with mean the range measurement $\rho^{(1)}_{k,m}$ converted into Cartesian coordinates assuming an angle uniformly distributed within the transmitter's antenna beam, and standard deviation in accordance to the noise $w^{(1)}_{k,m}$ in equations (4.1); the 3D velocity component, i.e., $\boldsymbol{v}^{(p)}_{k|k-1,m'}$, is drawn from a Gaussian distribution independent of k, m', and p, with mean zero and scalar covariance matrix whose non-zero element is related to the target's maximum speed, according to the one-point initialization provided in [76, Sec. 3.2.2]. Finally, homogeneous particle weights are set,

[8]The notation $i|j$ as subscript indicates a random variable/vector evaluated at time i given the measurements from the initial time up to time j.

[9]The subscript $k|k-1$ is kept for consistency with the notation used for the predicted sets of particles. Clearly, new potential targets are independent of the previous time scan $k-1$.

i.e., $\omega^{(p)}_{k|k-1,m'} = \frac{p^{\mathrm{b}}}{N_{\mathrm{p}}}$, with $p^{\mathrm{b}} \ll 1$ the assumed birth probability. It is worth noting that by using this mechanism, the number of potential targets — i.e., of particle sets — grows indefinitely over time; indeed, following the initialization, the number of potential targets at time k becomes $L_k \triangleq L_{k-1} + M^{(1)}_k$. Therefore, in order to keep a tractable computational complexity, a pruning step is performed at each time scan k, before prediction and initialization, in order to remove all potential targets whose probability of existence is below a prefixed threshold [56, 78].

4.2.2 Iterative SPA-Based Data Association

The sets of weighted particles obtained at the previous step, and all measurements collected by all receivers at time k are used to compute the soft association probabilities for each potential target-measurement combination according to the SPA-based data association algorithm as described in [56, 80]. These soft association probabilities are used as they are in the update step, whereas they are transformed into hard potential target-measurement association so as to cluster the measurements into groups to be used in the next ARCE localization step. The hard potential target-measurement associations are obtained by applying a maximum-a-posteriori criterion to the approximated measurement-oriented data association pmfs, computed as described in [56, Sec. VI-B].

4.2.3 ARCE Localization

During this step an estimate of each potential target position, denoted by $\boldsymbol{p}^{\mathrm{ARCE}}_{k,\ell}$, is obtained using the ARCE localization algorithm. As widely explained in Chapter 3, in order to compute $\boldsymbol{p}^{\mathrm{ARCE}}_{k,\ell}$ the ARCE localization algorithm requires as input a set of bistatic-range measurements associated to potential target ℓ, as well as specific angular constraints. The set of measurements is obtained through the hard potential target-measurement associations computed at the previous step. The angular constraints are selected according to two different approaches. When using the NAD – non-adaptive -

approach, the angular constraints just reflect the physical beam of the transmitter antenna; therefore, they are the same for all the potential targets. The AD – adaptive - approach defines different angular constraints for each potential target ℓ according to a bespoke virtual beam, obtained as the intersection of the physical beam of the transmitter antenna and a tailored beam. This tailored beam is steered towards the predicted potential target position obtained as the weighted sum (according to $\omega^{(p)}_{k|k-1,\ell}$) of the particles $\boldsymbol{p}^{(p)}_{k|k-1,\ell}$.

To compute the width of the tailored beam in azimuth ($x-y$ plane) and elevation ($x-z$ plane), first the particles $\boldsymbol{p}^{(p)}_{k|k-1,\ell}$ are converted from Cartesian to spherical coordinates; then, the standard deviations of azimuth and elevation, denoted by $\sigma^{\mathrm{az}}_{k,\ell}$ and $\sigma^{\mathrm{el}}_{k,\ell}$, respectively, are computed to measure the potential target spreading along the principal planes. Finally, the widths in azimuth and elevation are set to, respectively, $d^{\mathrm{az}}_{k,\ell} = 2\tilde{C}\sigma^{\mathrm{az}}_{k,\ell}$ and $d^{\mathrm{el}}_{k,\ell} = 2\tilde{C}\sigma^{\mathrm{el}}_{k,\ell}$, where $\tilde{C}$ is a scaling factor to widen ($\tilde{C} > 1$) or narrow ($\tilde{C} < 1$) the tailored beam.

4.2.4 Particles Enrichment

Objective of this step is to provide a more accurate/reliable sampling of the potential target state space, or, equivalently, a more accurate representation of the potential target belief, exploiting the position estimate $\boldsymbol{p}^{\mathrm{ARCE}}_{k,\ell}$ provided by the ARCE.

The idea comes from the consideration that the number of particles — limited to keep a tractable computational complexity – might not be enough to well describe the potential target belief. Moreover, this coarse representation can propagate over time, eventually leading to the particle impoverishment and a performance degradation. Hence, to prevent these impairments, the intuition is to replace the less significant particles representing the predicted potential target position, i.e., $\boldsymbol{p}^{(p)}_{k|k-1,\ell}$, with new particles drawn from a suitable distribution centered in the ARCE localization estimate. The aforementioned distribution, referred to as ARCE-based distribution, is a Gaussian with mean $\boldsymbol{p}^{\mathrm{ARCE}}_{k,\ell}$ and prefixed standard deviation σ^{ARCE} used to model the uncertainty of the estimated ARCE location. A detailed description of the substitution procedure follows.

For each potential target ℓ, let us assume without loss of generality that the weights $\omega^{(p)}_{k|k-1,\ell}$ are ordered from the smallest to the largest, i.e., $\omega^{(p)}_{k|k-1,\ell} \leqslant \omega^{(q)}_{k|k-1,\ell}$ for $p < q$.

Then, let us denote with $\mathscr{P} \triangleq \{1, \ldots, N_\mathrm{g}\}$ the set of indices representing the fraction $1-\alpha_\mathrm{r}$, $\alpha_\mathrm{r} \in (0,1)$, of less significant particles that will be replaced; N_g is therefore the largest possible value in $\{1, \ldots, N_\mathrm{p}\}$ such that the following holds:[10]

$$\frac{\sum_{q=1}^{N_\mathrm{g}} \omega^{(q)}_{k|k-1,\ell}}{\sum_{p=1}^{N_\mathrm{p}} \omega^{(p)}_{k|k-1,\ell}} \leqslant (1-\alpha_\mathrm{r}).$$

The enriched set of weighted particles, denoted by $\{\overline{\boldsymbol{s}}^{(p)}_{k|k-1,\ell}, \overline{\omega}^{(p)}_{k|k-1,\ell}\}_{p=1}^{N_\mathrm{p}}$, is built as follows. The particle $\overline{\boldsymbol{s}}^{(p)}_{k|k-1,\ell}$ is

$$\overline{\boldsymbol{s}}^{(p)}_{k|k-1,\ell} = \begin{cases} \left[\check{\boldsymbol{p}}^{(p)\mathrm{T}}_{k|k-1,\ell}, \boldsymbol{v}^{(p)\mathrm{T}}_{k|k-1,\ell}\right]^\mathrm{T}, & p \in \mathscr{P}, \\ \boldsymbol{s}^{(p)}_{k|k-1,\ell}, & p \notin \mathscr{P}, \end{cases}$$

where $\check{\boldsymbol{p}}^{(p)}_{k|k-1,\ell}$ is drawn from the ARCE-based distribution; note that only the 3D position component of the particle is replaced if $p \in \mathscr{P}$, whereas the 3D velocity component $\boldsymbol{v}^{(p)}_{k|k-1,\ell}$ is kept since the ARCE localization algorithm does not provide any velocity information.

The weight $\overline{\omega}^{(p)}_{k|k-1,\ell}$ is

$$\overline{\omega}^{(p)}_{k|k-1,\ell} = \left(\sum_{d=1}^{N_\mathrm{p}} \omega^{(d)}_{k|k-1,\ell}\right) \times \begin{cases} \dfrac{1-\alpha_\mathrm{r}}{N_\mathrm{g}}, & p \in \mathscr{P}, \\ \dfrac{\alpha_\mathrm{r}\, \omega^{(p)}_{k|k-1,\ell}}{\sum_{q \notin \mathscr{P}} \omega^{(q)}_{k|k-1,\ell}}, & p \notin \mathscr{P}. \end{cases}$$

[10]Note that if the weights are uniform — as for the new potential targets – this procedure is equivalent to a random selection of the particles to replace. Specifically, each particle p is replaced with probability $1-\alpha_\mathrm{r}$ and maintained with probability α_r.

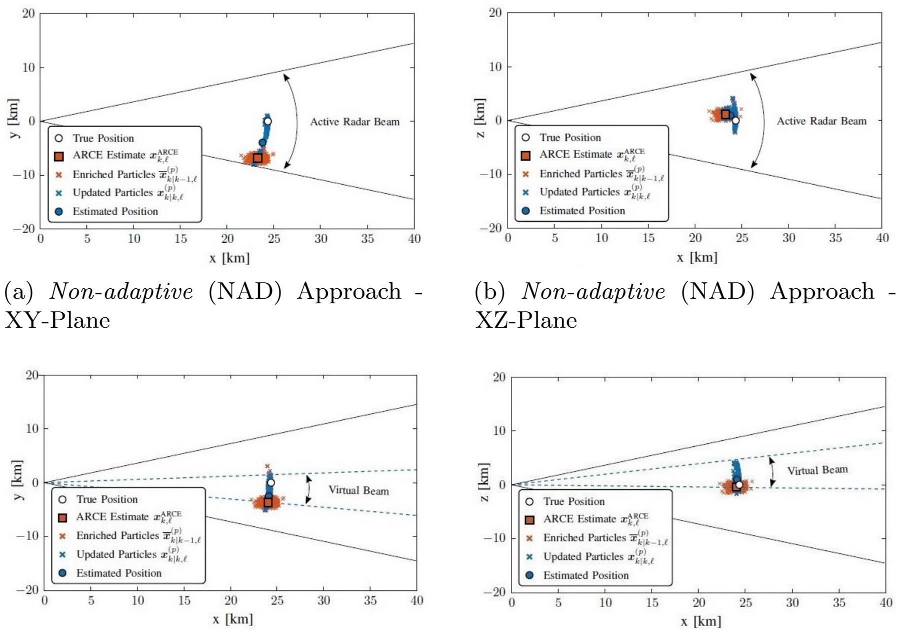

(a) *Non-adaptive* (NAD) Approach - XY-Plane

(b) *Non-adaptive* (NAD) Approach - XZ-Plane

(c) *Adaptive* (AD) Approach - XY-Plane

(d) *Adaptive* (AD) Approach - XZ-Plane

Figure 4.2. Illustrations of the proposed ARCE-enhanced SPA-based MTT algorithm — both the non-adaptive (top plots) and the adaptive (bottom graphs) approaches — in a 3D single target scenario, assuming the active radar located at $[0, 0, 0]^{\mathrm{T}}$ with its antenna pointing towards the x-axis; the plots show the $x - y$ planes (left panels) and the $x - z$ planes (right panels). The non-adaptive approach considers the active radar beam to establish the angular constraints used for the computation of the ARCE estimate; the adaptive approach, instead, utilizes a virtual beam as described in Section 4.2.3.

This construction ensures that *i)* the weights of the substituted particles are uniform and retain a fraction $1 - \alpha_{\mathrm{r}}$ of the total weight of the set; *ii)* the weights of the remaining particles are unchanged except that for a normalization factor that let them retain a fraction α_{r} of the total weight of the set; and *iii)* the sum of all the weights is unchanged, that is, $\sum_{p=1}^{N_{\mathrm{P}}} \omega^{(p)}_{k|k-1,\ell} = \sum_{q=1}^{N_{\mathrm{P}}} \overline{\omega}^{(q)}_{k|k-1,\ell}$.

At the end of this step, the a-priori knowledge of the monostatic active radar beam can be also used to penalize the particles lying outside the constrained region by applying an acceptance/rejection process as described in [85].

4.2.5 Update

According to the implementation of the SPA-based MTT algorithm in [55, Sec. VI], the enriched sets of weighted particles $\{\overline{\boldsymbol{s}}^{(p)}_{k|k-1,\ell}, \overline{\omega}^{(p)}_{k|k-1,\ell}\}_{p=1}^{N_\mathrm{P}}$, $\ell \in \{1, \ldots, L_k\}$, are updated using the measurements collected by all the receivers at current time k and the soft association probabilities computed at the iterative SPA-based data association step. The updated sets of weighted particles, denoted $\{\boldsymbol{s}^{(p)}_{k|k,\ell}, \omega^{(p)}_{k|k,\ell}\}_{p=1}^{N_\mathrm{P}}$, represent the beliefs of the potential targets at current time, i.e., $\tilde{f}(\boldsymbol{s}_{k,\ell}, r_{k,\ell} = 1)$, which in turn approximate the joint posterior pdfs $f(\boldsymbol{s}_{k,\ell}, r_{k,\ell} = 1|\boldsymbol{\rho}_{1:k})$. The potential target ℓ is confirmed if the marginal posterior pmf $p(r_{k,\ell} = 1|\boldsymbol{\rho}_{1:k}) \approx p^\mathrm{e}_{k|k,\ell}$ is above the threshold P_th, and that an estimate of its state is obtained from the marginal posterior pdf $f(\boldsymbol{s}_{k,\ell}|r_{k,\ell} = 1, \boldsymbol{\rho}_{1:k}) \approx \tilde{f}(\boldsymbol{s}_{k,\ell}, r_{k,\ell} = 1)/p^\mathrm{e}_{k|k,\ell}$.

Following the update, a resampling of the particles may be required as to reduce the degeneracy effect [83]; this process results in the weights $\omega^{(p)}_{k|k,\ell}$ to be all equal and whose sum is the posterior probability of existence $p^\mathrm{e}_{k|k,\ell}$.

Figs. 4.2 provide illustrations of the proposed ARCE-enhanced SPA-based MTT algorithm in a 3D single target scenario at a generic time scan k, assuming that the active radar is located at $\boldsymbol{p}_{t_k} = [0, 0, 0]^\mathrm{T}$ and the antenna pointing direction is steered towards the x-axis; the left-hand side plots (panels (a) and (c)) and the right-hand side plots (panels (b) and (d)) show the projections of all the 3D points onto, respectively, the $x - y$ and the $x - z$ planes.

All figures show the true position of the target (white circle), the ARCE estimate (red square), the set of enriched particles computed as described in Section 4.2.4 (red crosses), the set of updated particles obtained as illustrated in Section 4.2.5 (blue crosses), and the final estimated position of the target (blue circle). The top plots refer to the non-adaptive case, that is, when the angular constraints used within the ARCE localization algorithm (see. Section 4.2.3) coincide with the physical beam of the transmitter's antenna.

As expected, the ARCE estimate is within the active radar beam and, especially looking at the $x - z$ plane in Fig. 4.2(b), close to the true target position, allowing a better sampling of the state space in this relevant region. The bottom figures show the same example when the adaptive approach (exploiting a virtual beam) is adopted. The ARCE estimate is now restricted to the virtual beam, designed as described above; this avoids to spread the new N_{g} particles, generated during the particles enrichment step in a region where it is less likely to observe the target, as happens, for example, with the non-adaptive approach in Fig. 4.2(a).

4.3 Experiments

In this section, the performance of the proposed algorithm described in Section 4.2 is assessed in simulations.

4.3.1 Simulation setup

The simulations consider a 3D scenario with a stationary transmitter located at the origin of the reference system (i.e., $\boldsymbol{p}_{t_k} = \boldsymbol{p}_t = [0, 0, 0]^{\mathrm{T}}$ km) and $S = 5$ receivers located, respectively, at $\boldsymbol{p}_r^{(1)} = [0, 0, 0]^{\mathrm{T}}$ km, $\boldsymbol{p}_r^{(2)} = [0.916, 0.941, 0.95]^{\mathrm{T}}$ km, $\boldsymbol{p}_r^{(3)} = [0.973, 0.541, 0.764]^{\mathrm{T}}$ km, $\boldsymbol{p}_r^{(4)} = [0.955, 0.483, 0.191]^{\mathrm{T}}$ km, and $\boldsymbol{p}_r^{(5)} = [0.936, 0.350, 0.477]^{\mathrm{T}}$ km. Note that the transmitter and receiver 1 are co-located (monostatic active radar), i.e., $\boldsymbol{p}_t = \boldsymbol{p}_r^{(1)}$.

Two targets moving radially towards the active radar are simulated. In particular, target 1 is moving close to the antenna's beam edge, while target 2 is moving in the middle of the antenna's beam. Both targets are simulated for 100 time steps with a scan time of 10 s, and their speed is set to 5 m/s.

The monostatic and bistatic measurements generated by the targets are simulated according to equations (4.1) with $n_{k,m}^{(i)} \triangleq n^{(i)}$ being distributed as a Gaussian random variable with mean 0 and standard deviation defined as in equations (3.3) Finally, the frequency bandwidth of the probing waveform is equal to $B = 20$ MHz.

The performance of the baseline SPA-based MTT algorithm performing only target tracking [55, 56] are compared with the proposed method described in Section 4.2. In particular, for the proposed method the NAD and the AD versions (see Section 4.2.3) for three values of $\tilde{C} = 1, 2, 3$ are considered.

The performance of the different methods is measured according the Generalized Optimal Sub-Pattern Assignment (GOSPA) metric [86] that accounts for localization errors for correctly confirmed targets, as well as errors for missed targets and false targets; all the results are averaged over 200 Monte Carlo trials.

An ideal scenario without missed detections and false alarms is simulated, as well as a more challenging scenario, where the detection probabilities of the receivers are lower than 1 and false alarms are present. For the ideal scenario, the performance of the stand-alone ARCE localization algorithm at each time step are considered, too.

4.3.2 Results in ideal scenario

First, the ideal scenario is analyzed, in which the active radar and the receivers do not produce any false alarms and no missed detections are present, that is the detection probability $P_{\mathrm{d}}^{(i)} = P_{\mathrm{d}}$ of each receiver i is equal to 1.

Target 1 and target 2 in two distinct single-target scenarios are considered; both targets start at a range of 30 km. Simulations are performed for three different SNR noise levels at 30 km equal for all receivers and the active radar, i.e., $\mathrm{SNR}_i = \overline{\mathrm{SNR}}$ for $i = 1, \ldots, 5$, with $\overline{\mathrm{SNR}} = 0$ dB, $\overline{\mathrm{SNR}} = -10$, dB and $\overline{\mathrm{SNR}} = -20$ dB.

Figs. 4.3 and 4.4 show, respectively for target 1 and target 2, the comparison between the ARCE localization algorithm, the baseline SPA-based MTT algorithm, and the proposed algorithm ('Prop.') both NAD and AD versions with $\tilde{C} = 1, 2, 3$, in terms of the MGOSPA error, i.e., averaged over the 200 Monte Carlo trials, and for the different values of $\overline{\mathrm{SNR}}$. The number of particles N_{p} is 500, $\alpha_{\mathrm{r}} = 0.7$, $N_{\mathrm{g}} = \lfloor (1 - \alpha_{\mathrm{r}}) N_{\mathrm{p}} \rceil$, and σ_{ARCE} is set to 500 m.

It is possible to observe that the ARCE method performs worse than both the proposed and the baseline techniques. Moreover, the gap among the performances of the different methods reduces as the level of $\overline{\mathrm{SNR}}$ increases. The proposed methods are those performing generally better: specifically, the NAD version for $\overline{\mathrm{SNR}} = 0$ dB and $\overline{\mathrm{SNR}} = -10$ dB, and the AD versions for $\overline{\mathrm{SNR}} = -20$ dB with $\tilde{C} = 3$ and $\tilde{C} = 1$ for target 1 and target 2, respectively.

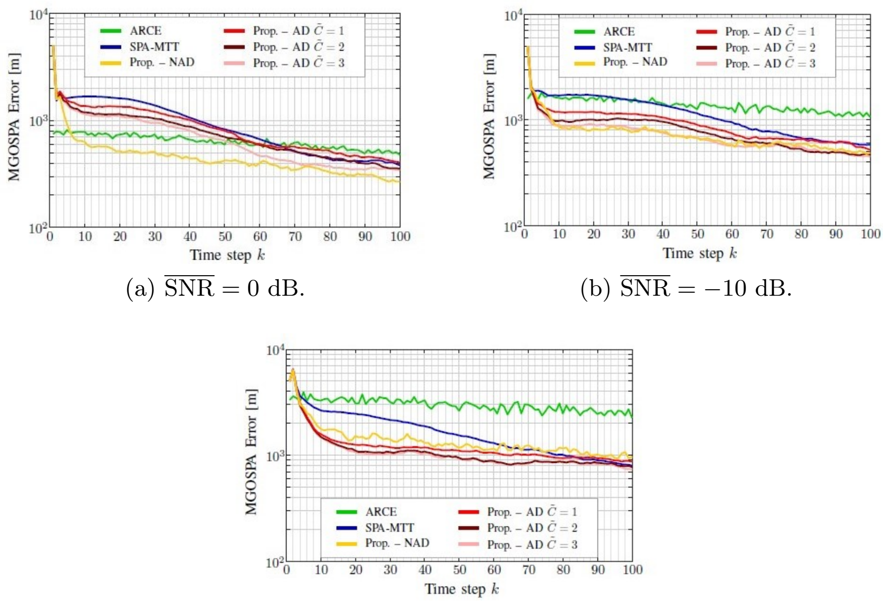

(a) $\overline{\mathrm{SNR}} = 0$ dB.

(b) $\overline{\mathrm{SNR}} = -10$ dB.

(c) $\overline{\mathrm{SNR}} = -20$ dB.

Figure 4.3. Comparison between the ARCE localization algorithm, the baseline SPA-based MTT algorithm, and the proposed algorithm (‘Prop.’) — both NAD and AD — in an ideal scenario ($P_\mathrm{d} = 1$ and no false alarms) with target 1 moving close to the antenna’s beam edge, in terms of MGOSPA error and on varying $\overline{\mathrm{SNR}}$.

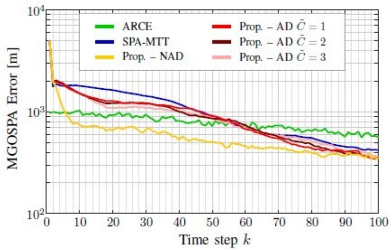

(a) $\overline{\mathrm{SNR}} = 0$ dB.

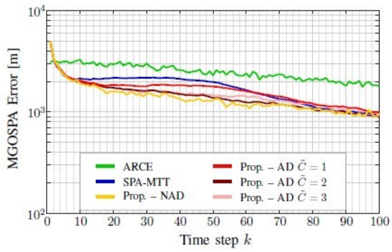

(b) $\overline{\mathrm{SNR}} = -10$ dB.

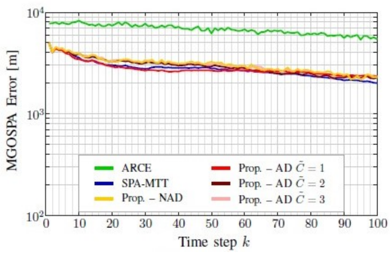

(c) $\overline{\mathrm{SNR}} = -20$ dB.

Figure 4.4. Comparison between the ARCE localization algorithm, the baseline SPA-based MTT algorithm, and the proposed algorithm ('Prop.') — both NAD and AD — in an ideal scenario ($P_\mathrm{d} = 1$ and no false alarms) with target 2 moving in the middle of the antenna's beam, in terms of MGOSPA error and on varying $\overline{\mathrm{SNR}}$.

In order to appreciate the main advantage of using ARCE in the proposed method, the performance of the SPA-based MTT and the proposed method for a varying number of particles are compared.

Figs. 4.5 show a comparison between the baseline SPA-based MTT algorithm and the proposed algorithm ('Prop.') — AD with $\tilde{C} = 3$ — for $\overline{\mathrm{SNR}} = -10$ dB, in terms of MGOSPA averaged over two distinct time intervals, i.e., 'interval A' from time step 10 to time step 40 (continuous lines), and 'interval B' from time step 41 to time step 100 (dashed lines), and varying the number of particles N_p. Performance of the ARCE algorithm are reported for reference, even if it is independent of the number of particles.

Fig. 4.5(a) shows the results for target 1 (moving close to the antenna's beam edge), while the Fig. 4.5(b) shows the results for target 2 (moving in the middle of antenna's beam). In both cases, the largest improvement of the proposed algorithm against the SPA-based MTT algorithm is achieved for a lower number of particles, i.e., $N_\mathrm{p} = 500$ or $N_\mathrm{p} = 1000$, and for interval A, as shown by the blue and red continuous lines. For interval B the gap in the performances between the SPA-based MTT and the proposed method is reduced, as shown by the red and blue dashed lines.

As the number of particles N_p increases up to 2500, the performances of the SPA-based MTT and the proposed method tend to converge. This behavior suggests that the ARCE estimates provide useful hints for an effective sampling of the space in particular when targets are initialized (i.e., within time interval A) and for a low number of particles. For a larger number of particles, the sampling of the space is inherently more effective, making the impact of the ARCE estimates less significant. Overall, the use of a lower number of particles is desirable especially when a large number of targets needs to be tracked.

4.3.3 Results in non-ideal scenario

A multitarget scenario with both target 1 and target 2, clutter-generated measurements, and missed detections is now analyzed. In this scenario, target 1 starts at a range of 35 km, while target 2 at

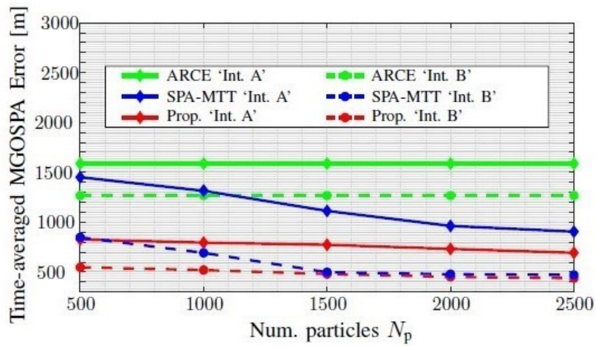

(a) Target 1 moving close to the antenna's beam edge.

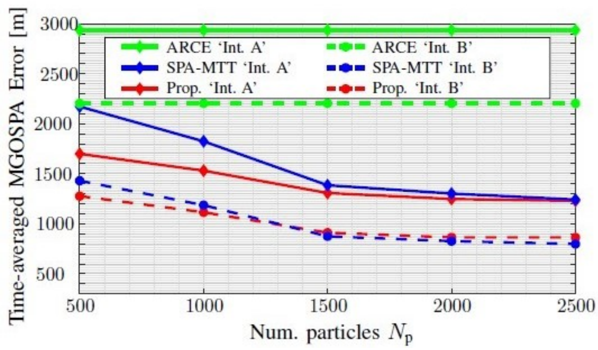

(b) Target 2 moving in the middle of the antenna's beam.

Figure 4.5. Comparison between the ARCE localization algorithm, the baseline SPA-based MTT algorithm, and the proposed algorithm ('Prop.') — AD with $\tilde{C} = 3$ — in an ideal scenario ($P_d = 1$ and no false alarms), for $\overline{\text{SNR}} = -10$ dB, in terms of MGOSPA averaged over time interval A (step 10 to step 40, continuous lines) and time interval B (step 41 to step 100, dashed lines) and varying the number of particles N_p.

a range of 30 km. The number of false alarms for each receiver i is modeled according to a Poisson distribution with mean 1, while the detection probability $P_\mathrm{d}^{(i)}$ is equal to 0.9 for the active radar $i = 1$, and 0.7 for the other receivers $i = 2, \ldots, 5$.

The performances of the baseline and the proposed algorithm, both NAD and AD versions with $\tilde{C} = 1, 2, 3$, are shown in Figs. 4.6 in terms of MGOSPA error and for varying $\overline{\mathrm{SNR}}$. As before, it is set $N_\mathrm{p} = 500$, $\alpha_\mathrm{r} = 0.7$, $N_\mathrm{g} = \lfloor (1 - \alpha_\mathrm{r}) N_\mathrm{p} \rceil$, and $\sigma_\mathrm{ARCE} = 500$ m. It is worth highlighting that the proposed NAD version and AD version with $\tilde{C} = 3$ still perform better than the baseline algorithm, especially with an $\overline{\mathrm{SNR}}$ equal to 0 dB and -10 dB.

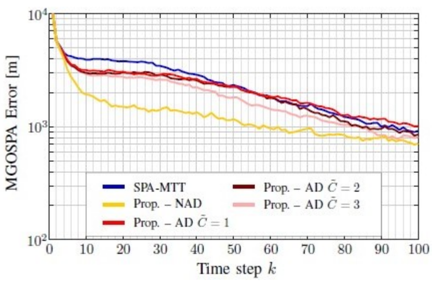

(a) $\overline{\mathrm{SNR}} = 0$ dB.

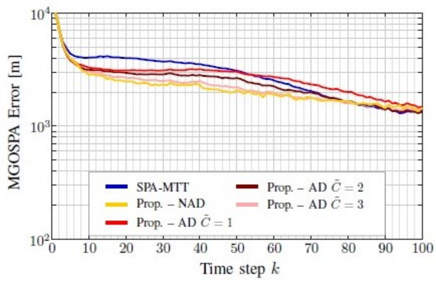

(b) $\overline{\mathrm{SNR}} = -10$ dB.

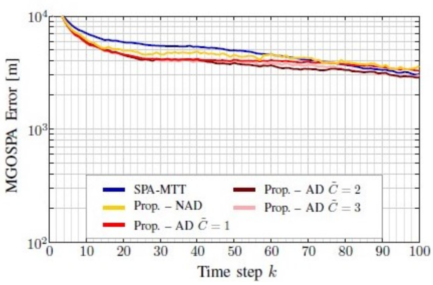

(c) $\overline{\mathrm{SNR}} = -20$ dB.

Figure 4.6. Comparison between the the baseline SPA-based MTT algorithm and the proposed algorithm ('Prop.') — both NAD and AD — in a non-ideal scenario with two targets moving within the antenna's beam, in terms of MGOSPA error and on varying $\overline{\mathrm{SNR}}$.

Chapter 5

Conclusions

In this thesis, advanced target localization algorithms for several sensing systems of interest are developed. In order to boost the performance in terms of estimation accuracy, a constrained optimization approach is exploited.

A 2D localization algorithm for PBR system capitalizing signals emitted by multiple illuminators of opportunity and measurements collected by a co-located active radar is considered in Chapter 2. The algorithm, i.e., AACLS, is designed resorting to the constrained LS framework. Specifically, angular and range constraints accounting for both a-priori information on the PBR receive antenna main-beam size and the uncertainty characterizing active radar data have been forced on the localization process. Hence the problem has been formulated as a constrained LS estimation. The resulting non-convex optimization problem is efficiently solved invoking the KKT optimality conditions. Then, an efficient solution technique is derived which searches the target position estimate among a number of candidate in closed-form, whose evaluation just rely on the computation of elementary functions. The analyses, in terms of RMSE, reveal the improvement of the proposed technique when compared with some counterparts available in the open literature. In particular, the proposed strategy outperforms the ACLS algorithm, which considers only the PBR angular information, demonstrating the effectiveness of a holistic passive/active radar localization procedure which properly exploits the active radar information. The analyses have also shown that the PBR main-beam size not always affects the localization, in fact AACLS is totally blind to the PBR angular extent constraint when the state-space limitation induced by active side-information is the most stringent. Moreover the effectiveness of the proposed strategy is demonstrated also for a dynamic scenario, where a surveillance system equipped with a PBR exploits the measurements at each scanning period provided by a co-located active rotating radar. In fact, it is shown that staring the passive radar in a specific area of tactical interest the localization reliability is assured also in the time instants where no active information is available, namely the PBR appropriately works as a gap-filler. This is an important achievement in particular when the localization of fast and manoeuvring targets is addressed.

In Chapter 3, a novel strategy for 3D target positioning, i.e., ARCE, is developed for a MPRN composed of a master transmit-receive node and multiple receive sensors. The monostatic radiation pattern features have been wisely exploited in the proposed positioning process restricting the angular location of any illuminated target. Hence, leveraging monostatic and bistatic range measurements, the Cartesian coordinates of the target have been estimated as the global optimal solution to a constrained non-convex LS problem. Then, the KKT optimality conditions are leveraged to obtain an efficient method for position estimation in quasi-closed-form. In particular, by means of an ad-hoc partition of the feasible set, a finite number of candidate optimal solutions has been identified, whose evaluation just rely on the computation of elementary functions and of the roots of specific polynomial equations. For this last task a smart rooting method has been designed capitalizing the structure of the involved equations and the bisection method. Remarkably, the overall target localization process demands a computational complexity proportional to the squared number of receive units. The performance of the proposed algorithm has been assessed in terms of RMSE also in comparison with some competitors available in the open literature. For the considered case studies, the new method achieves interesting accuracy gains over the counterparts, especially for weak target returns. Besides, it exhibits performance levels close to the RCRLB benchmark and even better for small values of $\overline{\mathrm{SNR}}_0$, further corroborating its effectiveness.

Finally, in Chapter 4 a solution to combine the ARCE algorithm with the scalable SPA-based MTT approach is proposed in order to boost the accuracy of the overall surveillance system. In particular, SPA-based MTT technique is enhanced by a particles generation process which exploits the ARCE estimate. The localization process accounts for the available information about the antenna beamwidth of the transmitter and the virtual beamwidth obtained from the target predicted uncertainty through angular constraints. Hence, a new set of particles drawn from a distribution whose parameters depend on the target location estimate is generated. Experimental results in a simulated 3D scenario have shown that the proposed solution is able to achieve superior performance than the baseline SPA-based MTT.

Future research may regard experimental validation of the proposed algorithms on measured data, as well as the extention of the developed framework to a MPRN comprising multiple transmitters and in scenarios including multipath environments.

Appendix A

Appendix of Chapter 2

This Appendix contains all the technical details relating to Chapter 2. Specifically, it deals with the regularity of the feasible points for Problem $\mathcal{P}$ along with the proof of Proposition 2.2.1.

A.1 Proof of Proposition 2.2.1

Lemma A.1.1. *Any feasible point $\bar{\boldsymbol{x}}$ to (2.15), is regular for the optimization Problem $\mathcal{P}$.*

Proof. Let $\bar{\boldsymbol{x}} = [\bar{x}_1, \bar{x}_2, \bar{x}_3]^T$ be a feasible point to $\mathcal{P}$. Before proceeding further, being $R_1^a > 0$ and γ a finite positive value, note that $\bar{x}_1 > 0$, which implies that the inequality constraint (2.17d) is inactive, at any feasible point. In fact, if $\bar{x}_1 = 0$, $\bar{x}_3 = 0$, which is impossible due to the constraint (2.17b). As a result, $\bar{\boldsymbol{x}} = [0, 0, 0]^T$ cannot be a feasible point, and hereafter the inequality constraint (2.17d) is assumed inactive, i.e., $\bar{x}_1 > 0$. To study the regularity of a feasible point $\bar{\boldsymbol{x}}$, the following cases should be distinguished:

1. constraints (2.17b) and (2.17c) are simultaneously inactive. The gradient of $\bar{\boldsymbol{x}}^T\bar{\boldsymbol{x}}$ is

   $$\nabla \tilde{\boldsymbol{p}}^T \boldsymbol{B} \tilde{\boldsymbol{p}}\big|_{\tilde{\boldsymbol{p}}=\bar{\boldsymbol{x}}} = 2[\bar{x}_1, \bar{x}_2, -\bar{x}_3]^T \neq 0$$

   implying the regularity of $\bar{\boldsymbol{x}}$.

2. $\bar{x}_3 = c_1$ (or $\bar{x}_3 = R_1^a$) and constraints (2.17c) are inactive. The gradients
$$\nabla \tilde{\boldsymbol{p}}^T \boldsymbol{B} \tilde{\boldsymbol{p}}\big|_{\tilde{\boldsymbol{p}}=\bar{\boldsymbol{x}}} = 2[\bar{x}_1, \bar{x}_2, -c_1]^T$$
$$(\text{or } \ \nabla \tilde{\boldsymbol{p}}^T \boldsymbol{B} \tilde{\boldsymbol{p}}\big|_{\tilde{\boldsymbol{p}}=\bar{\boldsymbol{x}}} = 2[\bar{x}_1, \bar{x}_2, -R_1^a]^T)$$
and
$$\nabla \tilde{p}_3 = [0, 0, 1]^T$$
are linearly independent and hence $\bar{\boldsymbol{x}}$ is regular.

3. $\bar{x}_2 = \bar{x}_1\gamma$ (or $\bar{x}_2 = -\bar{x}_1\gamma$) and (2.17b) are inactive. The gradients
$$\nabla \tilde{\boldsymbol{p}}^T \boldsymbol{B} \tilde{\boldsymbol{p}}\big|_{\tilde{\boldsymbol{p}}=\bar{\boldsymbol{x}}} = 2[\bar{x}_1, \gamma\bar{x}_1, -\bar{x}_3]^T$$
$$(\text{or } \ \nabla \tilde{\boldsymbol{p}}^T \boldsymbol{B} \tilde{\boldsymbol{p}}\big|_{\tilde{\boldsymbol{p}}=\bar{\boldsymbol{x}}} = 2[\bar{x}_1, -\gamma\bar{x}_1, -\bar{x}_3]^T)$$
and
$$\nabla(\tilde{p}_2 - \tilde{p}_1\gamma) = [-\gamma, 1, 0]^T$$
$$(\text{or } \nabla(-\tilde{p}_2 - \tilde{p}_1\gamma) = [-\gamma, -1, 0]^T)$$
are linearly independent and hence $\bar{\boldsymbol{x}}$ is regular.

4. $\bar{x}_3 = c_1$ and $\bar{x}_2 = \bar{x}_1\gamma$ (or $\tilde{x}_2 = -\bar{x}_1\gamma$). The gradients
$$\nabla \tilde{\boldsymbol{p}}^T \boldsymbol{B} \tilde{\boldsymbol{p}}\big|_{\tilde{\boldsymbol{p}}=\bar{\boldsymbol{x}}} = 2[\bar{x}_1, \gamma\bar{x}_1, -c_1]^T$$
$$(\text{or } \ \nabla \tilde{\boldsymbol{p}}^T \boldsymbol{B} \tilde{\boldsymbol{p}}\big|_{\tilde{\boldsymbol{p}}=\bar{\boldsymbol{x}}} = 2[\bar{x}_1, -\gamma\bar{x}_1, -c_1]^T),$$
$$\nabla \tilde{p}_3 = [0, 0, 1]^T,$$
and
$$\nabla(\tilde{p}_2 - \tilde{p}_1\gamma) = [-\gamma, 1, 0]^T$$
$$(\text{or } \nabla(-\tilde{p}_2 - \tilde{p}_1\gamma) = [-\gamma, -1, 0]^T)$$
are linearly independent implying the regularity of $\bar{\boldsymbol{x}}$.

5. For $\bar{x}_3 = R_1^a$ and $\bar{x}_2 = \bar{x}_1\gamma$ (or $\bar{x}_2 = -\bar{x}_1\gamma$) the same results as

in (4) are obtained, with R_1^a instead of c_1.

Following the same line of reasoning, it can be also shown that the feasible points for the restricted versions of $\mathcal{P}$, obtained considering the different regions of the feasible set, of interest fulfill the regularity condition. □

Proof of Proposition 2.2.1

As a first step toward the closed-form target position estimate, note that Weierstrass theorem ensures the existence of a global minimizer to $\mathcal{P}$, being the objective function continuous and the constraint set compact. Furthermore, all the feasible points of $\mathcal{P}$ are regular, (as shown in Lemma A.1.1), and both the objective and the constraint functions are twice continuously differentiable. Hence, the key idea of the subsequent proof is to establish candidate optimal solutions, searching for KKT-points [71, Proposition 3.3.1] (or directly optimal solutions), within the subsets induced by specific problem constraints. In this respect, different cases, related to diverse portions of the feasible set, are examined in the sequel. Note that, $\tilde{p}_1 > 0$ for any feasible point being $R_1^a > 0$ and $\bar{\theta} \leq \pi/2$.

a) Assume all the inequality constraints inactive, candidate optimal solutions to $\mathcal{P}$ can be found among the regular points of

$$\mathcal{P}_1 \begin{cases} \min\limits_{\tilde{\boldsymbol{p}}} & \|\tilde{\boldsymbol{H}}\tilde{\boldsymbol{p}} - \boldsymbol{g}\|^2 \\ \text{s.t.} & \tilde{\boldsymbol{p}}^T \boldsymbol{B} \tilde{\boldsymbol{p}} = 0 \end{cases},$$

which satisfy the necessary first- and second-order optimality conditions [71], [70], [87, Theorem 3.1], as well as the inequality constraints

$$\begin{cases} R_1^a < \tilde{p}_3^* < c_1 \\ -\gamma \tilde{p}_1^* < \tilde{p}_2^* < \gamma \tilde{p}_1^* \\ \tilde{p}_1^* > 0 \end{cases}.$$

This set of inequalities account for the specific feasible set of Problem (2.17) and differs from that involved in the ACLS counterpart, where the target feasible positions describe a convex set. These solutions[1] are among the points [62]

$$\tilde{\boldsymbol{x}}^*(\eta_h) = \left(\tilde{\boldsymbol{H}}^T \tilde{\boldsymbol{H}} + \eta_h \boldsymbol{B}\right)^{-1} \tilde{\boldsymbol{H}}^T \boldsymbol{g}$$

with $\eta_h,\ h \in \bar{I}_1 \subseteq \{1, \dots, 4\}$, the real-valued roots of the fourth-order equation

$$\tilde{\boldsymbol{x}}^*(\eta_h)^T \boldsymbol{B} \tilde{\boldsymbol{x}}^*(\eta_h) = 0,$$

which belong to

$$\left(-\frac{1}{\lambda_2\left(\boldsymbol{B}, \tilde{\boldsymbol{H}}^T \tilde{\boldsymbol{H}}\right)}, +\infty\right) - \left\{-\frac{1}{\lambda_1\left(\boldsymbol{B}, \tilde{\boldsymbol{H}}^T \tilde{\boldsymbol{H}}\right)}, -\frac{1}{\lambda_3\left(\boldsymbol{B}, \tilde{\boldsymbol{H}}^T \tilde{\boldsymbol{H}}\right)}\right\}.$$

As a consequence, there are at most four candidate optimal points to $\mathcal{P}$ for case a).

b) If $\tilde{p}_3 = c_1$, then $\mathcal{P}$ is equivalent to

$$\mathcal{P}_2 \begin{cases} \min\limits_{\tilde{\boldsymbol{q}}} & \|\tilde{\boldsymbol{H}}_1 \tilde{\boldsymbol{q}} - \boldsymbol{g} + \tilde{\boldsymbol{h}}_3 c_1\|^2 \\ \text{s.t.} & \tilde{\boldsymbol{q}}^T \tilde{\boldsymbol{q}} = c_1^2 \\ & -\gamma \tilde{q}_1 \leq \tilde{q}_2 \leq \gamma \tilde{q}_1 \\ & \tilde{q}_1 \geq 0 \end{cases},$$

where $\tilde{\boldsymbol{q}} = [\tilde{q}_1, \tilde{q}_2]^T$ and $\tilde{\boldsymbol{p}} = [\tilde{\boldsymbol{q}}^T, c_1]^T$. Assuming $-\gamma \tilde{p}_1 < \tilde{p}_2 <$

[1] If the matrix $(\tilde{\boldsymbol{H}}^T \tilde{\boldsymbol{H}} + \eta_h \boldsymbol{B})$ is singular, assuming $\lambda_1\left(\boldsymbol{B}, \tilde{\boldsymbol{H}}^T \tilde{\boldsymbol{H}}\right) \neq \lambda_2\left(\boldsymbol{B}, \tilde{\boldsymbol{H}}^T \tilde{\boldsymbol{H}}\right) \neq \lambda_3\left(\boldsymbol{B}, \tilde{\boldsymbol{H}}^T \tilde{\boldsymbol{H}}\right)$, a different technique can be used to solve the KKT equations. Nevertheless, in more than ten thousand trials the above singularity condition can never lead to candidate optimal solutions.

$\gamma\tilde{p}_1$ and $\tilde{p}_1 > 0$, candidate optimal solutions to $\mathcal{P}_2$ can be found among the feasible points of

$$\mathcal{P}_3 \begin{cases} \min\limits_{\tilde{\boldsymbol{q}}} & \left\|\tilde{\boldsymbol{H}}_1\tilde{\boldsymbol{q}} - \boldsymbol{g} + \tilde{\boldsymbol{h}}_3 c_1\right\|^2 \\ \text{s.t.} & \tilde{\boldsymbol{q}}^T\tilde{\boldsymbol{q}} = c_1^2 \end{cases},$$

which comply with the necessary first- and second-order optimality conditions and satisfy

$$\begin{cases} -\gamma\tilde{p}_1 < \tilde{p}_2 < \gamma\tilde{p}_1 \\ \tilde{p}_1 > 0 \end{cases}. \tag{A.1}$$

These solutions can be obtained from the points[2]

$$\tilde{\boldsymbol{q}}^*(\beta_h) = \left(\tilde{\boldsymbol{H}}_1^T\tilde{\boldsymbol{H}}_1 + \beta_h\boldsymbol{I}\right)^{-1}\tilde{\boldsymbol{H}}_1^T\left(\boldsymbol{g} - \tilde{\boldsymbol{h}}_3 c_1\right)$$

with $\beta_h,\ h \in \bar{I}_2 \subseteq \{1,\ldots,4\}$, the real-valued roots to the fourth order equation

$$\tilde{\boldsymbol{q}}^{*^T}(\beta_h)\tilde{\boldsymbol{q}}^*(\beta_h) = c_1^2$$

such that $\beta_h > -\lambda_{\max}\left(\tilde{\boldsymbol{H}}_1^T\tilde{\boldsymbol{H}}_1\right)$ and $\beta_h \neq -\lambda_{\min}\left(\tilde{\boldsymbol{H}}_1^T\tilde{\boldsymbol{H}}_1\right)$. As a consequence, there are at most four candidate optimal points to $\mathcal{P}$ for case b) obtained appending to $\tilde{\boldsymbol{q}}^*(\beta_h)$ the last component c_1, i.e., $\tilde{\boldsymbol{x}}^*(\beta_h) = [\tilde{q}_1^*(\beta_h), \tilde{q}_2^*(\beta_h), c_1]^T,\ h \in I_2 \subseteq \bar{I}_2$.

c) If $\tilde{p}_3 = R_1^a$ as well as $-\gamma\tilde{p}_1 < \tilde{p}_2 < \gamma\tilde{p}_1$ and $\tilde{p}_1 > 0$, following the same line of reasoning as for case b), the candidate optimal solutions are given by the points $\tilde{\boldsymbol{x}}^*(\zeta_h) = [\tilde{q}_1^*(\beta_h), \tilde{q}_2^*(\beta_h), R_1^a]^T$, with $\tilde{\boldsymbol{q}}^*(\zeta_h) = \left(\tilde{\boldsymbol{H}}_1^T\tilde{\boldsymbol{H}}_1 + \zeta_h\boldsymbol{I}\right)^{-1}\tilde{\boldsymbol{H}}_1^T\left(\boldsymbol{g} - \tilde{\boldsymbol{h}}_3 R_1^a\right)$ fulfilling (A.1), where $\tilde{\boldsymbol{q}} = [\tilde{q}_1, \tilde{q}_2]^T \in \mathbb{R}^2$ and $\zeta_h,\ h \in \bar{I}_3 \subseteq \{1,\ldots,4\}$ the real-valued roots to the fourth order equation $\tilde{\boldsymbol{q}}^{*^T}(\zeta_h)\tilde{\boldsymbol{q}}^*(\zeta_h) = R_1^{a2}$ such that

[2] A situation similar to footnote 1 occurs for the case $\beta_h = -\lambda_{\min}(\tilde{H}_1^T\tilde{H}_1)$ and $\beta_h = -\lambda_{\max}(\tilde{H}_1^T\tilde{H}_1)$.

$\zeta_h > -\lambda_{\max}\left(\tilde{\boldsymbol{H}}_1^T\tilde{\boldsymbol{H}}_1\right)$ and $\zeta_h \neq -\lambda_{\min}\left(\tilde{\boldsymbol{H}}_1^T\tilde{\boldsymbol{H}}_1\right)$. It is worth pointing out that this range constraint, which is not present in [62], provides other four possible candidate optimal solutions that are not contemplated in the ACLS strategy. In particular, these points replace $\tilde{\boldsymbol{x}}^* = \mathbf{0}$.

d) If $\tilde{p}_2 = (-1)^{i+1}\gamma\tilde{p}_1, i = 1, 2$, the candidate solutions are the two points

$$\boldsymbol{x}_{4_i}^* = \alpha_i^* \left[1,\ (-1)^{i+1}\gamma,\ \sqrt{1+\gamma^2}\right]^T,\ i = 1, 2,$$

with

$$\alpha_i^* = \min\left(\max\left(\frac{R_1^a}{\sqrt{1+\gamma^2}}, \frac{\boldsymbol{v}_i^T\boldsymbol{g}}{||\boldsymbol{v}_i||^2}\right), \frac{c_1}{\sqrt{1+\gamma^2}}\right) \tag{A.2}$$

the optimal solution to

$$\mathcal{P}\begin{cases} \min\limits_{\alpha_i} & \|\boldsymbol{v}_i\alpha_i - \boldsymbol{g}\|^2 \\ \text{s.t.} & \frac{R_1^a}{\sqrt{1+\gamma^2}} \leq \alpha_i \leq \frac{c_1}{\sqrt{1+\gamma^2}} \end{cases},$$

where $\boldsymbol{v}_i = \tilde{\boldsymbol{H}}\left[1, (-1)^{i+1}\gamma, \sqrt{1+\gamma^2}\right]^T$. Note that, unlike [62], the lowest value of (A.2) is strictly greater than zero, to comply with the target positions feasible set of Problem (2.17).

Appendix **B**

Appendix of Chapter 3

This Appendix contains all the technical details relating to Chapter 3. Specifically, it comprises two parts. Part B.1 deals with the regularity of the feasible points for Problem $\mathcal{P}$ along with the proof of Proposition 3.2.1. Part B.2 carries out the design of computationally efficient techniques to identify candidate optimal solutions of the problem at hand.

B.1 Proof of Proposition 3.2.1

Lemma B.1.1. *Any feasible point $\bar{\boldsymbol{x}}$ to (3.8) is regular for the optimization Problem $\mathcal{P}$.*

Proof. Let $\bar{\boldsymbol{x}} = [\bar{x}_1, \bar{x}_2, \bar{x}_3]^T$ be a feasible point to $\mathcal{P}$. Note that $\bar{x}_1 > 0$, i.e., the inequality constraint (3.8d) is inactive. In fact, due to the constraint (3.8a), $\bar{\boldsymbol{x}} = [0, 0, 0]^T$ cannot be a feasible point. To study the regularity of $\bar{\boldsymbol{x}}$, the following situations should be distinguished:

1. constraints (3.8b) and (3.8c) are simultaneously inactive. The gradient of $\bar{\boldsymbol{x}}^T\bar{\boldsymbol{x}}$ is

   $$\nabla \boldsymbol{p}^T\boldsymbol{p}\big|_{\boldsymbol{p}=\bar{\boldsymbol{x}}} = 2[\bar{x}_1, \bar{x}_2, \bar{x}_3]^T \neq \mathbf{0}$$

   implying the regularity of $\bar{\boldsymbol{x}}$.

2. $\bar{x}_2 = \gamma_a \bar{x}_1$ (or $\bar{x}_2 = -\gamma_a \bar{x}_1$) and constraints (3.8c) are inactive. The gradients

$$\nabla \boldsymbol{p}^T \boldsymbol{p}\big|_{\boldsymbol{p}=\bar{\boldsymbol{x}}} = 2[\bar{x}_1, \gamma_a \bar{x}_1, \bar{x}_3]^T$$

$$(\text{or } \ \nabla \boldsymbol{p}^T \boldsymbol{p}\big|_{\boldsymbol{p}=\bar{\boldsymbol{x}}} = 2[\bar{x}_1, -\gamma_a \bar{x}_1, \bar{x}_3]^T)$$

and

$$\nabla (p_2 - \gamma_a p_1) = [-\gamma_a, 1, 0]^T$$
$$(\text{or } \nabla (-p_2 - \gamma_a p_1) = [-\gamma_a, -1, 0]^T)$$

are linearly independent and hence $\bar{\boldsymbol{x}}$ is regular.

3. $\bar{x}_3 = \gamma_e \bar{x}_1$ (or $\bar{x}_3 = -\gamma_e \bar{x}_1$) and constraints (3.8b) are inactive. The gradients

$$\nabla \boldsymbol{p}^T \boldsymbol{p}\big|_{\boldsymbol{p}=\bar{\boldsymbol{x}}} = 2[\bar{x}_1, \bar{x}_2, \gamma_e \bar{x}_1]^T$$

$$(\text{or } \ \nabla \boldsymbol{p}^T \boldsymbol{p}\big|_{\boldsymbol{p}=\bar{\boldsymbol{x}}} = 2[\bar{x}_1, \bar{x}_2, -\gamma_e \bar{x}_1]^T)$$

and

$$\nabla (p_3 - \gamma_e p_1) = [-\gamma_e, 0, 1]^T$$
$$(\text{or } \nabla (-p_3 - \gamma_e p_1) = [-\gamma_e, 0, -1]^T)$$

are linearly independent and hence $\bar{\boldsymbol{x}}$ is regular.

4. $\bar{x}_3 = \gamma_e \bar{x}_1$ and $\bar{x}_2 = \gamma_a \bar{x}_1$ (or $\bar{x}_2 = -\gamma_a \bar{x}_1$). The gradients

$$\nabla \boldsymbol{p}^T \boldsymbol{p}\big|_{\boldsymbol{p}=\bar{\boldsymbol{x}}} = 2[\bar{x}_1, \gamma_a \bar{x}_1, \gamma_e \bar{x}_1]^T$$

$$(\text{or } \ \nabla \boldsymbol{p}^T \boldsymbol{p}\big|_{\boldsymbol{p}=\bar{\boldsymbol{x}}} = 2[\bar{x}_1, -\gamma_a \bar{x}_1, \gamma_e \bar{x}_1]^T),$$

$$\nabla (p_3 - \gamma_e p_1) = [-\gamma_e, 0, 1]^T$$

and

$$\nabla (p_2 - \gamma_a p_1) = [-\gamma_a, 1, 0]^T$$
$$(\text{or } \nabla (-p_2 - \gamma_a p_1) = [-\gamma_a, -1, 0]^T)$$

are linearly independent implying the regularity of $\bar{\boldsymbol{x}}$.

5. $\bar{x}_3 = -\gamma_e \bar{x}_1$ and $\bar{x}_2 = \gamma_a \bar{x}_1$ (or $\bar{x}_2 = -\gamma_a \bar{x}_1$). The gradients

$$\nabla \boldsymbol{p}^T \boldsymbol{p}\big|_{\boldsymbol{p}=\bar{\boldsymbol{x}}} = 2[\bar{x}_1, \gamma_a \bar{x}_1, -\gamma_e \bar{x}_1]^T$$

$$(\text{or } \ \nabla \boldsymbol{p}^T \boldsymbol{p}\big|_{\boldsymbol{p}=\bar{\boldsymbol{x}}} = 2[\bar{x}_1, -\gamma_a \bar{x}_1, -\gamma_e \bar{x}_1]^T),$$

$$\nabla\left(-p_3 - \gamma_e p_1\right) = [-\gamma_e, 0, -1]^T$$

and

$$\nabla\left(p_2 - \gamma_a p_1\right) = [-\gamma_a, 1, 0]^T$$
$$(\text{or } \nabla\left(-p_2 - \gamma_a p_1\right) = [-\gamma_a, -1, 0]^T)$$

are linearly independent implying the regularity of $\bar{\boldsymbol{x}}$.

Following the same line of reasoning, it can be also shown that the feasible points of the restricted versions of $\mathcal{P}$, obtained considering the different regions of the feasible set, fulfill the regularity condition. □

Proof of Proposition 3.2.1

Let us first observe that Weierstrass theorem ensures the existence of a global minimizer to $\mathcal{P}$, being the objective function continuous and the constraint set compact. The basic idea behind the proof is to establish candidate optimal solutions among the feasible points of the problem, which are all regular according to Lemma B.1.1. To this end, different regions of the feasible set are explored.

a) Assuming all the inequality constraints inactive, candidate optimal solutions to $\mathcal{P}$ can be found among the regular points of

$$\mathcal{P}_1 \begin{cases} \min\limits_{\boldsymbol{p}} & ||\boldsymbol{H}\boldsymbol{p} - \boldsymbol{g}||^2 \\ \text{s.t.} & ||\boldsymbol{p}||^2 = \bar{b}_0^2 \end{cases},$$

which satisfy the necessary first-order optimality conditions [71], as well as the inequality constraints

$$\begin{cases} -\gamma_a x_p^* < y_p^* < \gamma_a x_p^* \\ -\gamma_e x_p^* < z_p^* < \gamma_e x_p^* \\ x_p^* > 0 \end{cases}.$$

These solutions[1] are among the points

$$\boldsymbol{x}^*(\bar{\lambda}_h) = \left(\boldsymbol{H}^T\boldsymbol{H} + \bar{\lambda}_h\boldsymbol{I}\right)^{-1}\boldsymbol{H}^T\boldsymbol{g} \tag{B.1}$$

with $\bar{\lambda}_h,\ h \in \bar{I}_1 \subseteq \{1,\ldots,6\}$, the real-valued roots of the sixth-order equation

$$\boldsymbol{x}^*(\bar{\lambda})^T\boldsymbol{x}^*(\bar{\lambda}) = \bar{b}_0^2.$$

As a consequence, there are at most six candidate optimal points to $\mathcal{P}$ for case a).

b) If $y_p = (-1)^{i+1}\gamma_a x_p, i = 1,2$, then $\mathcal{P}$ is equivalent to

$$\mathcal{P}_2^i \begin{cases} \min\limits_{\boldsymbol{q}} & ||\boldsymbol{H}_i^a\boldsymbol{q} - \boldsymbol{g}||^2 \\ \text{s.t.} & \boldsymbol{q}^T\boldsymbol{B}^a\boldsymbol{q} = \bar{b}_0^2 \\ & -q_1\gamma_e \le q_2 \le q_1\gamma_e \\ & q_1 \ge 0 \end{cases},$$

where $\boldsymbol{q} = [x_p, z_p]^T$,

$$\boldsymbol{H}_i^a = \boldsymbol{H}\begin{bmatrix} 1 & 0 \\ (-1)^{i+1}\gamma_a & 0 \\ 0 & 1 \end{bmatrix}, i = 1,2,$$

[1] The solutions in (B.1) implicitly assume that $(\boldsymbol{H}^T\boldsymbol{H} + \bar{\lambda}_h\boldsymbol{I})$ is full-rank. However, almost surely the necessary condition $(\boldsymbol{H}^T\boldsymbol{H} + \bar{\lambda}_h\boldsymbol{I})\boldsymbol{p} = \boldsymbol{H}^T\boldsymbol{g}$ when $(\boldsymbol{H}^T\boldsymbol{H} + \bar{\lambda}_h\boldsymbol{I})$ is rank deficient does not admit solution, provided that $\boldsymbol{H}$ is full-column rank.

and

$$\boldsymbol{B}^a = \begin{bmatrix} 1+\gamma_a^2 & 0 \\ 0 & 1 \end{bmatrix}.$$

Assuming $-q_1\gamma_e < q_2 < q_1\gamma_e$ and $q_1 > 0$, candidate optimal solutions to $\mathcal{P}_2$ can be found among the feasible points of

$$\mathcal{P}_3^i \begin{cases} \min\limits_{\boldsymbol{q}} & ||\boldsymbol{H}_i^a \boldsymbol{q} - \boldsymbol{g}||^2 \\ \text{s.t.} & \boldsymbol{q}^T \boldsymbol{B}^a \boldsymbol{q} = \bar{b}_0^2 \end{cases},$$

which comply with the necessary optimality conditions and satisfy $-q_1\gamma_e < q_2 < q_1\gamma_e$ and $q_1 > 0$. These solutions can be obtained from the points[2]

$$\boldsymbol{q}^*(\beta_h^i) = \left(\boldsymbol{H}_i^{aT}\boldsymbol{H}_i^a + \beta_h^i \boldsymbol{B}^a\right)^{-1} \boldsymbol{H}_i^{aT}\boldsymbol{g}$$

with $\beta_h^i, h \in \bar{I}_2^i \subseteq \{1, ..., 4\}$, the real-valued roots to the fourth-order equation

$$\boldsymbol{q}^{*T}(\beta_h^i)\boldsymbol{B}^a\boldsymbol{q}^*(\beta_h^i) = \bar{b}_0^2.$$

As a consequence, there are at most eight candidate optimal points to $\mathcal{P}$ for case b) with inequalities strictly satisfied, obtained as $[q_1^*(\beta_h^i), (-1)^{i+1}\gamma_a q_1^*(\beta_h^i), q_2^*(\beta_h^i)]^T, i = 1, 2,\ h \in I_2^i \subseteq \bar{I}_2^i$.

c) If $z_p = (-1)^{i+1}\gamma_e x_p, i = 1, 2$, and $y_p \neq (-1)^{j+1}\gamma_a x_p, j = 1, 2$, the same technique as in case b) is used.

d) If $y_p = (-1)^{i+1}\gamma_a x_p$ and $z_p = (-1)^{j+1}\gamma_e x_p, (i, j) \in \{1, 2\}^2$, the candidate solutions are the four points

$$\boldsymbol{x}_{4_{i,j}}^* = \frac{\bar{b}_0}{\sqrt{1+\gamma_a^2+\gamma_e^2}}[1, (-1)^{i+1}\gamma_a, (-1)^{j+1}\gamma_e]^T,$$

$$(i, j) \in \{1, 2\}^2.$$

[2] A situation similar to footnote 1 occurs, i.e., almost surely candidate optimal solutions demand $\boldsymbol{H}_i^{aT}\boldsymbol{H}_i^a + \beta_h^i \boldsymbol{B}^a$ to be full-rank.

B.2 Efficient Techniques to Identify Candidate Solutions

To solve the considered 3D localization problem, an efficient procedure is required to identify the real-valued solutions to the equations (3.9), (3.11), and (3.13). To this end, let us focus on equation (3.9) and let $\boldsymbol{U}\text{diag}(\lambda)\boldsymbol{U}^T$ be the eigenvalue decomposition of $\boldsymbol{C} = \boldsymbol{H}^T\boldsymbol{H}$, with $\boldsymbol{U} \in \mathbb{C}^{3,3}$ containing orthonormal eigenvectors of $\boldsymbol{C}$ and $\lambda = [\lambda_1, \lambda_2, \lambda_3]^T \in \mathbb{C}^3$ collecting the corresponding eigenvalues arranged in decreasing order; after some manipulations, (3.9) can be rewritten as

$$\sum_{j=1}^{3} \frac{|z_j|^2}{(\bar{\lambda} + \lambda_j)^2} = \bar{b}_0^2, \tag{B.2}$$

where z_j is the j-th component of the vector $\boldsymbol{z} = \boldsymbol{U}^T\boldsymbol{H}^T\boldsymbol{g} \in \mathbb{C}^3$ and λ_j is the j-th component of the vector λ. Remarkably, since the eigenvalues and eigenvectors of $\boldsymbol{C}$ can be computed through elementary functions of the entries of $\boldsymbol{H}$, the parameters involved in (B.2) are available in closed-form. Evidently, solving (B.2) is tantamount to determining the roots of

$$\bar{f}(\bar{\lambda}) = \frac{\bar{z}_1^2}{(\bar{\lambda} + \lambda_1)^2} + \frac{\bar{z}_2^2}{(\bar{\lambda} + \lambda_2)^2} + \frac{\bar{z}_3^2}{(\bar{\lambda} + \lambda_3)^2} - 1, \tag{B.3}$$

where $\bar{z}_j = \frac{z_j}{|\bar{b}_0|}, j = 1, 2, 3$. To proceed further, let us observe that $\bar{f}(\bar{\lambda})$ is strictly convex within each of the four intervals $\mathscr{I}_1 = (-\infty, -\lambda_3)$, $\mathscr{I}_2 = (-\lambda_3, -\lambda_2)$, $\mathscr{I}_3 = (-\lambda_2, -\lambda_1)$, and $\mathscr{I}_4 = (-\lambda_1, +\infty)$, being the second-order derivative of $\bar{f}(\bar{\lambda})$ always positive. Besides, $\bar{f}(\bar{\lambda})$ is strictly increasing over $\mathscr{I}_1$ and strictly decreasing over $\mathscr{I}_4$, with $\lim_{\bar{\lambda} \to \mp\infty} \bar{f}(\bar{\lambda}) = -1$. Leveraging the above results, it follows that:

- There exists a unique root of (B.3) within $\mathscr{I}_1$ and another one (still unique) over $\mathscr{I}_4$;
- With reference to the intervals $\mathscr{I}_2$ and $\mathscr{I}_3$, the existence of roots depends on the minimum value v_i^* of (B.3) within $\mathscr{I}_2$ and

$\mathscr{I}_3$, respectively. In particular, if $v_i^* > 0$ then (B.3) does not admit roots belonging to $\mathscr{I}_2$ (or $\mathscr{I}_3$), otherwise there exist two roots if $v_i^* < 0$ and a unique one if $v_i^* = 0$.

Hence, the unique roots in $\mathscr{I}_1$ and $\mathscr{I}_4$, can be computed via the bisection algorithm [88]. As to the intervals $\mathscr{I}_2$ and $\mathscr{I}_3$, a two-step strategy is now illustrated. At the first stage, the global minimum solution $\bar{\lambda}_i^*$, over $\mathscr{I}_i, i = 2, 3$, and the corresponding objective value v_i^* are determined resorting to the bisection method applied over $\mathscr{I}_i, i = 2, 3$, to the first-order derivative of $\bar{f}(\bar{\lambda})$, i.e,

$$\bar{f}'(\bar{\lambda}) = -2\left(\frac{\bar{z}_1^2}{(\bar{\lambda}+\lambda_1)^3} + \frac{\bar{z}_2^2}{(\bar{\lambda}+\lambda_2)^3} + \frac{\bar{z}_3^2}{(\bar{\lambda}+\lambda_3)^3}\right).$$

Then, the possible roots of (B.3) are searched. Specifically, if $v_i^* < 0$ two distinct roots exist, $\bar{\lambda}_{i,1} < \bar{\lambda}_{i,2}$ say, which are obtained carrying out the bisection method to the function $\bar{f}(\bar{\lambda})$ over the intervals $(-\lambda_3, \bar{\lambda}_i^*)$ and $(\bar{\lambda}_i^*, -\lambda_2)$ (or $(-\lambda_2, \bar{\lambda}_i^*)$ and $(\bar{\lambda}_i^*, -\lambda_1)$), respectively. Otherwise, the root is either $\bar{\lambda}_i^*$ or does not exist, if $v_i^* > 0$.

Before proceeding further, two important remarks are in order.

Remark 1. Denoting by ϵ the desired accuracy level for the bisection method, $\bar{\lambda}_i^*$ and v_i^* may differ from the bisection output $\hat{\bar{\lambda}}_i^*$ and the corresponding objective value $\hat{v}_i^*$ at most by $\epsilon/2$ and $|\bar{f}'(\hat{\bar{\lambda}}_i^*)|\epsilon/2$, respectively. Now, if $\hat{v}_i^* - |\bar{f}'(\hat{\bar{\lambda}}_i^*)|\epsilon/2 > 0$, the absence of roots is guaranteed. Otherwise, even if $\hat{v}_i^* > 0$, possible roots may exist, whose ϵ-approximation can be evaluated leveraging $\hat{\bar{\lambda}}_i^*$. Indeed, depending on the sign of $\bar{f}'(\hat{\bar{\lambda}}_i^*)$, the potential roots (if existing) must belong to either $[\hat{\bar{\lambda}}_i^* - \epsilon/2, \hat{\bar{\lambda}}_i^*]$ or $[\hat{\bar{\lambda}}_i^*, \hat{\bar{\lambda}}_i^* + \epsilon/2]$. As a result, either pairs $(\hat{\bar{\lambda}}_i^* - \epsilon/2, \hat{\bar{\lambda}}_i^*)$ or $(\hat{\bar{\lambda}}_i^*, \hat{\bar{\lambda}}_i^* + \epsilon/2)$ can be used to compute candidate optimal solutions with a desired accuracy, which will be automatically discarded, during the screening of the candidates, if the roots do not exist.

Remark 2. According to the proposed strategy, it is required to execute, in general, three times the bisection method, once at the first stage and twice at the second. However, it is possible to avoid the first stage and determine the two potential roots with at most two bisection cycles, conceiving a bisection-like method: at each iteration, it jointly accounts for the sign of the derivative in correspondence of the two extremes of the current bisection interval as well as the objective value at the center of the mentioned interval, to update the extremes.

Following the same guideline, the solutions of equations (3.11) and (3.13) can be obtained. It is also worth observing that (3.11) and (3.13) could be, in principle, solved in closed-form. However, numerical errors have been experienced demanding the development of the aforementioned numerically robust solution method.

In the next subsection, details on the bisection initialization are illustrated.

Bisection Initialization

Without loss generality, let us focus on equation (3.9). To this end, let us first consider the root search over $\mathscr{I}_1$. Being

$$\bar{f}(\bar{\lambda}) \leq \frac{\|\bar{\boldsymbol{z}}\|^2}{(\bar{\lambda}+\lambda_3)^2} - 1, \quad \bar{\lambda} \leq -\lambda_3$$

and

$$\bar{f}(\bar{\lambda}) \geq \frac{\bar{z}_3^2}{(\bar{\lambda}+\lambda_3)^2} - 1, \quad \bar{\lambda} \leq -\lambda_3$$

with $\bar{\boldsymbol{z}} = [\bar{z}_1, \bar{z}_2, \bar{z}_3]^T$, it follows that the root $\bar{\lambda}_3 \in \mathscr{I}_1$ of (3.9) complies with

$$\bar{\lambda}_3 \in [-\lambda_3 - \|\bar{\boldsymbol{z}}\|, -\lambda_3 - |\bar{z}_3|].$$

As a consequence, the bisection method can be initialized with the search interval $[-\lambda_3 - \|\bar{\boldsymbol{z}}\|, -\lambda_3 - |\bar{z}_3|]$. Leveraging a similar line of reasoning, it stems that $[-\lambda_1 - \|\bar{\boldsymbol{z}}\|, -\lambda_1 - |\bar{z}_1|]$ can be used to initialize the bisection method over the interval $\mathscr{I}_4$.

As to the roots lying within $\mathscr{I}_2$ (analogous reasoning applies for $\mathscr{I}_3$) the initialization at the first stage can be set as $[-\lambda_3, -(\lambda_3 + \lambda_2)/2]$, if $\bar{f}'(-(\lambda_3 + \lambda_2)/2) > 0$ or $[-(\lambda_3 + \lambda_2)/2, -\lambda_2]$, if $\bar{f}'(-(\lambda_3 + \lambda_2)/2) < 0$. The second step, as already said, substantially employs $[-\lambda_3, \bar{\lambda}_i^*]$ and $[\bar{\lambda}_i^*, -\lambda_2]$ to initialize the two bisections.

Bibliography

[1] R. Karlsson and F. Gustafsson, "The Future of Automotive Localization Algorithms: Available, Reliable, and Scalable Localization: Anywhere and Anytime," *IEEE Signal Processing Magazine*, vol. 34, no. 2, pp. 60–69, Mar. 2017.

[2] D. Dardari, A. Conti, C. Buratti, and R. Verdone, "Mathematical Evaluation of Environmental Monitoring Estimation Error through Energy-Efficient Wireless Sensor Networks," *IEEE Transactions on Mobile Computing*, vol. 6, no. 7, pp. 790–802, July 2007.

[3] S. M. George, W. Zhou, H. Chenji, M. Won, Y. O. Lee, A. Pazarloglou, R. Stoleru, and P. Barooah, "DistressNet: A Wireless Ad Hoc and Sensor Network Architecture for Situation Management in Disaster Response," *IEEE Communications Magazine*, vol. 48, no. 3, pp. 128–136, Mar. 2010.

[4] J. Ko, T. Gao, R. Rothman, and A. Terzis, "Wireless Sensing Systems in Clinical Environments: Improving the Efficiency of the Patient Monitoring Process," *IEEE Engineering in Medicine and Biology Magazine*, vol. 29, no. 2, pp. 103–109, Mar. 2010.

[5] L. Evans, "Maps as Deep: Reading the Code of Location-Based Social Networks," *IEEE Technology and Society Magazine*, vol. 33, no. 1, pp. 73–80, 2014.

[6] Z. Cheng, Y. Wang, and Y. Shen, "Direct Position Determination of Multiple Targets via Reduced-dimension Beamspace," in *2017 IEEE International Conference on Communications Workshops (ICC Workshops)*, May 2017, pp. 1030–1035.

[7] M. F. Keskin, S. Gezici, and O. Arikan, "Direct and Two-Step Positioning in Visible Light Systems," *IEEE Transactions on Communications*, vol. 66, no. 1, pp. 239–254, Jan. 2018.

[8] H. Soganci, S. Gezici, and H. V. Poor, “Accurate Positioning in Ultra-Wideband Systems,” *IEEE Wireless Communications*, vol. 18, no. 2, pp. 19–27, Apr. 2011.

[9] T. Le and N. Ono, “Closed-Form and Near Closed-Form Solutions for TOA-Based Joint Source and Sensor Localization,” *IEEE Transactions on Signal Processing*, vol. 64, no. 18, pp. 4751–4766, 2016.

[10] H. Shen, Z. Ding, S. Dasgupta, and C. Zhao, “Multiple Source Localization in Wireless Sensor Networks Based on Time of Arrival Measurement,” *IEEE Transactions on Signal Processing*, vol. 62, no. 8, pp. 1938–1949, 2014.

[11] Y. T. Chan and K. C. Ho, “A Simple and Efficient Estimator for Hyperbolic Location,” *IEEE Transactions on Signal Processing*, vol. 42, no. 8, pp. 1905–1915, Aug. 1994.

[12] K. C. Ho, “Bias Reduction for an Explicit Solution of Source Localization Using TDOA,” *IEEE Transactions on Signal Processing*, vol. 60, no. 5, pp. 2101–2114, May 2012.

[13] N. Salman, M. Ghogho, and A. H. Kemp., “Optimized Low Complexity Sensor Node Positioning in Wireless Sensor Networks,” *IEEE Sensors Journal*, vol. 14, no. 1, pp. 39–46, Jan. 2014.

[14] H. Shao, X. P. Zhang, and Z. Wang, “Efficient Closed-Form Algorithms for AOA Based Self-Localization of Sensor Nodes Using Auxiliary Variables,” *IEEE Transactions on Signal Processing*, vol. 62, no. 10, pp. 2580–2594, 2014.

[15] K. C. Ho and W. Xuu, “An Accurate Algebraic Solution for Moving Source Location Using TDOA and FDOA Measurements,” *IEEE Transactions on Signal Processing*, vol. 52, no. 9, pp. 2453–2463, Sept. 2004.

[16] S. Tomic, M. Beko, and R. Dinis, “3-D Target Localization in Wireless Sensor Networks Using RSS and AoA Measurements,” *IEEE Transactions on Vehicular Technology*, vol. 66, no. 4, pp. 3197–3210, Apr. 2017.

[17] Y. Li, G. Qi, and A. Sheng, “Performance Metric on the Best Achievable Accuracy for Hybrid TOA/AOA Target Localization,” *IEEE Communications Letters*, vol. 22, no. 7, pp. 1474–1477, July 2018.

[18] J. Luo, X. Zhang, and Z. Wang, “A New Passive Source Localization Method Using AOA-GROA-TDOA in Wireless Sensor Array Networks and its Cramér-Rao Bound analysis,” in *2013 IEEE International Conference on Acoustics, Speech and Signal Processing*, 2013, pp. 4031–4035.

[19] P. Tarrío, A. M. Bernardos, X. Wang, and J. R. Casar, “Dynamic Channel Model LMS Updating for RSS-Based Localization,” in *Proceedings of the 6th International Conference on Hybrid Artificial Intelligent Systems - Volume Part II*, ser. HAIS’11. Berlin, Heidelberg: Springer-Verlag, 2011, p. 127–135.

[20] S. Stein., “Algorithms for Ambiguity Function Processing,” *IEEE Transactions on Acoustics, Speech, and Signal Processing*, vol. 29, no. 3, pp. 588–599, June 1981.

[21] N. Bulusu, J. Heidemann, and D. Estrin, “GPS-Less Low-Cost Outdoor Localization for Very Small Devices,” *IEEE Personal Communications*, vol. 7, no. 5, pp. 28–34, Oct. 2000.

[22] N. Patwari, J. N. Ash, S. Kyperountas, R. L. M. A. O. Hero, and N. S. Correal, “Locating the Nodes: Cooperative Localization in Wireless Sensor Networks,” *IEEE Signal Processing Magazine*, vol. 22, no. 4, pp. 54–69, July 2005.

[23] D. Musicki, R. Kaune, and W. Koch, “Mobile Emitter Geolocation and Tracking Using TDOA and FDOA Measurements,” *IEEE Transactions on Signal Processing*, vol. 58, no. 3, pp. 1863–1874, Mar. 2010.

[24] A. Quazi, “An Overview on the Time Delay Estimate in Active and Passive Systems for Target Localization,” *IEEE Transactions on Acoustics, Speech, and Signal Processing*, vol. 29, no. 3, pp. 527–533, June 1981.

[25] H. Griffiths, “Passive bistatic radar,” in *Academic Press Library in Signal Processing*, N. D. Sidiropoulos, F. Gini, R. Chellappa, and S. Theodoridis, Eds. Elsevier, 2014, ch. 16, pp. 813–855.

[26] A. Zaimbashi, M. Derakhtian, and A. Sheikhi, “GLRT-Based CFAR Detection in Passive Bistatic Radar,” *IEEE Transactions on Aerospace and Electronic Systems*, vol. 49, no. 1, pp. 134–159, Jan. 2013.

[27] H. D. Griffiths and C. J. Baker, *An Introduction to Passive Radar.* Artech House, Feb. 2017.

[28] R. Klemm, U. Nickel, C. Gierull, P. Lombardo, H. Griffiths, and W. Koch, *Novel Radar Techniques and Applications.* SciTech Publishing, 2017, vol. 1.

[29] W. L. Melvin and J. A. Scheer, *Principles of Modern Radar: Radar Applications.* Schitech Publishing, Jan. 2014.

[30] J. Shen, A. Molisch, and J. Salmi, “Accurate Passive Location Estimation Using TOA Measurements,” *IEEE Transactions on Wireless Communications*, vol. 11, no. 6, pp. 2182–2192, June 2012.

[31] B. T. Fang, "Simple Solutions for Hyperbolic and Related Position Fixes," *IEEE transactions on aerospace and electronic systems*, vol. 26, no. 5, pp. 748–753, Sept. 1990.

[32] L. Rui and K. C. Ho, "Elliptic Localization: Performance Study and Optimum Receiver Placement," *IEEE Transactions on Signal Processing*, vol. 62, no. 18, pp. 4673–4688, Sept. 2014.

[33] J. Liang, Y. Chen, H. C. So, and Y. Jing, "Circular/hyperbolic/elliptic Localization via Euclidean Norm Elimination," *Signal Processing*, vol. 148, pp. 102–113, 2018.

[34] Y. Zhao, Y. Zhao, and C. Zhao, "A Novel Algebraic Solution for Moving Target Localization in Multi-Transmitter Multi-Receiver Passive Radar," *Signal Processing*, vol. 143, pp. 303–310, Feb. 2018.

[35] Y. Zhou, C. Law, Y. Guan, and F. Chin, "Indoor Elliptical Localization based on Asynchronous UWB Range Measurement," *IEEE Transactions on Instrumentation and Measurements*, vol. 60, no. 1, pp. 248–257, Jan. 2011.

[36] P. Falcone, F. Colone, A. Macera, and P. Lombardo, "Localization and Tracking of Moving Targets with WiFi-based Passive Radar," in *2012 IEEE Radar Conference*, 2012, pp. 0705–0709.

[37] D. W. O'Hagan, S. R. Doughty, and M. R. Inggs, "Multistatic Radar Systems," in *Academic Press Library in Signal Processing, Volume 7*, R. Chellappa and S. Theodoridis, Eds. Academic Press, 2018, pp. 253–275.

[38] Z. Geng, "Evolution of Netted Radar Systems," *IEEE Access*, vol. 8, pp. 124 961–124 977, 2020.

[39] Y. Gao, H. Li, and B. Himed, "Joint Transmit and Receive Beamforming for Hybrid Active–Passive Radar," *IEEE Signal Processing Letters*, vol. 24, no. 6, pp. 779–783, June 2017.

[40] F. Wang and H. Li, "Joint Waveform and Receiver Design for Co-Channel Hybrid Active-Passive Sensing With Timing Uncertainty," *IEEE Transactions on Signal Processing*, vol. 68, pp. 466–477, 2020.

[41] D. W. O'Hagan, M. Ummenhofer, H. Kuschel, , and J. Heckenbach, "A Passive/Active Dual Mode Radar Concept," in *2013 14th International Radar Symposium (IRS)*, vol. 1, June 2013.

[42] H. Kuschel, J. Heckenbach, and J. Schell, "Deployable Multiband Passive/Active Radar for Air Defense (DMPAR)," *IEEE Aerospace and Electronic Systems Magazine*, vol. 28, no. 9, pp. 37–45, Sept. 2013.

[43] T. Brenner, L. Lamentowski, and W. Dyszynski, “Analysis of Chosen Results Based on Trials with Distributed and Collocated Passive-Active Radars,” in *2018 International Conference on Radar (RADAR)*, Brisbane, Australia, 2018.

[44] V. Stejskal, H. Kuschel, T. Brenner, L. Lamentowski, I. Norheim-Næss, P. Samczynski, and J. Kulpa, “DETOUR trials: The mission and its results,” in *2017 18th International Radar Symposium (IRS)*, 2017.

[45] N. Fiorenza, “NATO Demonstrates Fusion of Active and Passive Radar Detection in Military Network,” 2019, [Accessed 22 October 2022]. [Online]. Available: https://www.janes.com/defence-news/news-detail/nato-demonstrates-fusion-of-active-and-passive-radar-detection-in-military-network

[46] Chairs of NATO SET 242: K. Kulpa, D. Cristallini, Chairs of NATO SET 258: P. Samczynski, I. Norheim-Naess, “Joint NATO SET 242 and SET 258 Trials APART GAS 2019,” 2019.

[47] M. R. Inggs, C. Tong, D. O’Hagan, U. Bönigert, U. Siegenthaler, C. Schupbach, and H. Pratisto, “Noise Jamming of a FM Band Commensal Radar,” in *2015 IEEE Radar Conference*, pp. 493–498, 27–30 Oct. 2015.

[48] J. Li and P. Stoica, *MIMO Radar Signal Processing*. J. Wiley & Sons, Hoboken, NJ, 2009.

[49] N. J. Willis and H. D. Griffiths, *Advances in Bistatic Radar*. Raleigh, NC, USA: SciTech Publishing, 2007.

[50] H. D. Griffiths and C. J. Baker, “Towards the Intelligent Adaptive Radar Network,” in *IEEE Radar Conference 2013*, Ottawa, pp. 1–5, 30 Apr.–2 May 2013.

[51] M. Malanowski and K. Kulpa, “Two Methods for Target Localization in Multistatic Passive Radar,” *IEEE Transactions on Aerospace and Electronic Systems*, vol. 48, no. 1, pp. 572–580, Jan. 2012.

[52] J. Wen, J. Li, C. Yang, C. Chen, and H. Chen, “Localization Scheme of Multistatic Radars System Based on the Information of Measured Signal,” *2014 Ninth International Conference on Broadband and Wireless Computing, Communication and Applications*, pp. 462–466, Nov. 2014.

[53] H. Yang and J. Chun, “An Improved Algebraic Solution for Moving Target Localization in Noncoherent MIMO Radar Systems,” *IEEE Transactions on Signal Processing*, vol. 64, no. 1, pp. 258–270, Jan. 2016.

[54] L. Wanchun, T. Qiu, H. Chengfeng, and L. Yingxiang, “Location Algorithms for Moving Target in Non-Coherent Distributed Multiple-Input Multiple-Output Radar Systems,” *IET Signal Processing*, vol. 11, no. 5, pp. 503–514, July 2017.

[55] F. Meyer, P. Braca, P. Willett, and F. Hlawatsch, “A scalable algorithm for tracking an unknown number of targets using multiple sensors,” *IEEE Trans. Signal Process.*, vol. 65, no. 13, pp. 3478–3493, Jul. 2017.

[56] F. Meyer, T. Kropfreiter, J. L. Williams, R. A. Lau, F. Hlawatsch, P. Braca, and M. Z. Win, “Message passing algorithms for scalable multitarget tracking,” *Proc. IEEE*, vol. 106, no. 2, pp. 221–259, Feb. 2018.

[57] A. Marino, A. Aubry, A. De Maio, and P. Braca, “2D Constrained PBR Localization Via Active Radar Designation,” in *2020 IEEE Radar Conference (RadarConf20)*, pp. 1–6, 21–25 Sept. 2020.

[58] A. Aubry, P. Braca, A. De Maio, and A. Marino, “2D PBR localization complying with constraints forced by active radar measurements,” *IEEE Trans. Aerosp. Electron. Syst.*, vol. 57, no. 5, pp. 2647–2660, Oct. 2021.

[59] F. Colone, P. Falcone, C. Bongioanni, and P. Lombardo, “WiFi-Based Passive Bistatic Radar: Data Processing Schemes and Experimental Results,” *IEEE Transactions on Aerospace and Electronic Systems*, vol. 48, no. 2, pp. 1061–1079, Apr. 2012.

[60] V. Anastasio, A. Farina, F. Colone, and P. Lombardo, “Cramer - Rao Lower Bound with Pd $<$ 1 for Target Localisation Accuracy in Multistatic Passive Radar,” *IET Radar, Sonar and Navigation*, vol. 8, no. 7, pp. 767–775, Aug. 2014.

[61] M. A. Richards, J. A. Scheer, and W. A. Holm, *Principles of Modern Radar: Basic Principles.* Schitech Publishing, Jan. 2010.

[62] A. Aubry, V. Carotenuto, A. De Maio, and L. Pallotta, “Localization in 2D PBR With Multiple Transmitters of Opportunity: A Constrained Least Squares Approach,” *IEEE Transactions on Signal Processing*, vol. 68, pp. 634–646, Jan. 2020.

[63] S. L. Shmakov, “A Universal Method of Solving Quartic Equations,” *International Journal of Pure and Applied Mathematics*, vol. 71, no. 2, pp. 251–259, 2011.

[64] D. J. Torrieri, “Statistical theory of passive location systems,” *IEEE Trans. Aerosp. Electron. Syst.*, vol. 20, no. 2, pp. 183–198, Mar. 1984.

[65] Wikipedia contributors, "An/sps-49 — Wikipedia, the free encyclopedia," 2018, [Online; accessed 27-February-2020]. [Online]. Available: https://en.wikipedia.org/wiki/AN/SPS-49

[66] A. Aubry, P. Braca, A. De Maio, and A. Marino, "2D PBR Localization Complying with Constraints Forced by Active Radar Measurements," *IEEE Transactions on Aerospace and Electronic Systems*, pp. 1–1, 2021.

[67] A. Marino, A. Aubry, A. D. Maio, and P. Braca, "3D Localization for Multiplatform Radar Networks with Deployable Nodes," in *2021 Signal Processing Symposium (SPSympo)*, 2021, pp. 183–188.

[68] A. Marino, A. Aubry, A. D. Maio, P. Braca, D. Gaglione, and P. Willett, "Constrained Target Localization for Multiplatform Radar Systems," in *MILCOM 2021 - 2021 IEEE Military Communications Conference (MILCOM)*, 2021, pp. 635–640.

[69] A. Aubry, P. Braca, A. De Maio, and A. Marino, "Enhanced target localization with deployable multiplatform radar nodes based on non-convex constrained least squares optimization," *IEEE Trans. Signal Process.*, 2022.

[70] J. More, "Generalizations of the Trust Region Subproblem," *Optim. Methods Softw.*, vol. 2, pp. 189–209, Aug. 1993.

[71] D. Bertsekas, *Nonlinear Programming.* Athena Scientific, 2016.

[72] A. Beck, P. Stoica, and J. Li, "Exact and Approximate Solutions of Source Localization Problems," *IEEE Transactions on Signal Processing*, vol. 56, no. 5, pp. 1770–1778, May 2008.

[73] J. Gorman and A. Hero, "Lower bounds for parametric estimation with constraints," *IEEE Transactions on Information Theory*, vol. 36, no. 6, pp. 1285–1301, Nov. 1990.

[74] H. L. V. Trees, *Optimum Array Processing: Part IV of Detection, Estimation, and Modulation Theory.* Hoboken, NJ, USA: Wiley: John Wiley & Sons, 2004.

[75] Y. Zhang and K. C. Ho, "Multistatic Localization in the Absence of Transmitter Position," *IEEE Transactions on Signal Processing*, vol. 67, no. 18, pp. 4745–4760, Sept. 2019.

[76] Y. Bar-Shalom, P. K. Willett, and X. Tian, *Tracking and Data Fusion: A Handbook of Algorithms.* Storrs, CT, USA: YBS Publishing, 2011.

[77] J. Dezert and Y. Bar-Shalom, "Computational complexity of JPDA: Worst case analysis," Office National d'Etudes et de Recherches Aérospatiales (ONERA), Tech. Rep. TN-2021-04-21, Apr. 2021.

[78] M. Brambilla, D. Gaglione, G. Soldi, R. Mendrzik, G. Ferri, K. Lepage, M. Nicoli, P. Willett, P. Braca, and M. Win, "Cooperative Localization and Multitarget Tracking in Agent Networks with the Sum-Product Algorithm," *IEEE Open Journal of Signal Processing*, pp. 1–1, 2022.

[79] G. Soldi, F. Meyer, P. Braca, and F. Hlawatsch, "Self-tuning algorithms for multisensor-multitarget tracking using belief propagation," *IEEE Transactions on Signal Processing*, vol. 67, no. 15, pp. 3922–3937, Aug. 2019.

[80] D. Gaglione, G. Soldi, F. Meyer, F. Hlawatsch, P. Braca, A. Farina, and M. Z. Win, "Bayesian information fusion and multitarget tracking for maritime situational awareness," *IET Radar, Sonar Navig.*, vol. 14, p. 1845–1857, Dec. 2020.

[81] D. Gaglione, P. Braca, G. Soldi, F. Meyer, F. Hlawatsch, and M. Z. Win, "Fusion of sensor measurements and target-provided information in multitarget tracking," *IEEE Trans. Signal Process.*, vol. 70, pp. 322–336, 2022.

[82] H. V. Poor, *An Introduction to Signal Detection and Estimation*, 2nd ed. New York, NY, USA: Springer, 1994.

[83] T. Li, M. Bolic, and P. M. Djuric, "Resampling methods for particle filtering: Classification, implementation, and strategies," *IEEE Signal Process. Mag.*, vol. 32, no. 3, pp. 70–86, Apr. 2015.

[84] M. S. Arulampalam, S. Maskell, N. Gordon, and T. Clapp, "A tutorial on particle filters for online nonlinear/non-Gaussian Bayesian tracking," *IEEE Trans. Signal Process.*, vol. 50, no. 2, pp. 174–188, Feb. 2002.

[85] X. Shao, B. Huang, and J. M. Lee, "Constrained Bayesian state estimation – A comparative study and a new particle filter based approach," *Journal of Process Control*, vol. 20, no. 2, pp. 143–157, 2010.

[86] A. S. Rahmathullah, Á. F. García-Fernández, and L. Svensson, "Generalized optimal sub-pattern assignment metric," in *Proc. FUSION-17*, Xi'an, China, Jul. 2017, pp. 1–8.

[87] A. Beck, P. Stoica, and J. Li, "Exact and Approximate Solutions of Source Localization Problems," *IEEE Transactions on Signal Processing*, vol. 56, no. 5, pp. 1770–1778, 2008.

[88] J. P. T. Mo, S.C.P. Cheung, and R. Das, "Basic Numerical Techniques," in *Demystifying Numerical Models.* J. P. T. Mo, S.C.P. Cheung, and R. Das, Butterworth-Heinemann, ch. 2, pp. 5–31, 2019.

Author's Publications and Honors

[P1] L. Lan, A. Marino, A. Aubry, A. D. Maio, G. Liao and J. Xu,
Design of adaptive detectors for FDA-MIMO radar,
IEEE 11th Sensor Array and Multichannel Signal Processing Workshop (SAM),
2020, pp. 1-5, doi: 10.1109/SAM48682.2020.9104289.

[P2] L. Lan, A. Marino, A. Aubry, A. De Maio, G. Liao and J. Xu,
Design of GLR-Based Detectors for FDA-MIMO radar,
IEEE 7th International Workshop on Metrology for AeroSpace (MetroAeroSpace),
2020, pp. 17-21, doi: 10.1109/MetroAeroSpace48742.2020.9160020.

[P3] A. Marino, A. Aubry, A. De Maio and P. Braca,
2D Constrained PBR Localization Via Active Radar Designation,
IEEE Radar Conference (RadarConf20),
2020, pp. 1-6, doi: 10.1109/RadarConf2043947.2020.9266695.

[P4] A. Aubry, P. Braca, A. De Maio and A. Marino,
2-D PBR Localization Complying With Constraints Forced by Active Radar Measurements,
IEEE Transactions on Aerospace and Electronic Systems,
vol. 57, no. 5, pp. 2647-2660, 2021, doi: 10.1109/TAES.2021.3067612.

[P5] L. Lan, A. Marino, A. Aubry, A. De Maio, G. Liao, J. Xu, and Y. Zhang,
GLRT-Based Adaptive Target Detection in FDA-MIMO Radar,
IEEE Transactions on Aerospace and Electronic Systems,
vol. 57, no. 1, pp. 597-613, 2021, doi: 10.1109/TAES.2020.3028485.

[P6] A. Marino, A. Aubry, A. De Maio and P. Braca
3D Localization for Multiplatform Radar Networks with Deployable Nodes,
Signal Processing Symposium (SPSympo),
2021, pp. 183-188, doi: 10.1109/SPSympo51155.2020.9593537.

[P7] A. Marino, A. Aubry, A. De Maio, P. Braca, D. Gaglione and P. Willett,
Constrained Target Localization for Multiplatform Radar Systems,
IEEE Military Communications Conference (MILCOM),
2021, pp. 635-640, doi: 10.1109/MILCOM52596.2021.9653089.

[P8] A. Aubry, P. Braca, A. De Maio and A. Marino,
Enhanced Target Localization With Deployable Multiplatform Radar Nodes Based on Non-Convex Constrained Least Squares Optimization,
IEEE Transactions on Signal Processing,
vol. 70, pp. 1282-1294, 2022, doi: 10.1109/TSP.2022.3147037.

Angela Marino ranked **third in the Student Contest of the 1st International Virtual School on Radar Signal Processing**, held at the University of Electronic Science and Technology of China (UESTC), 22-23 December 2020, for the contribution:

A. Marino, A. Aubry, A. De Maio and P. Braca, "2D Constrained PBR Localization Via Active Radar Designation," 1st International Virtual School on Radar Signal Processing University of Electronic Science and Technology of China (UESTC), 22-23 December 2020.

Angela Marino was the recipient of the **first prize at the Young Scientist Contest Award of the Signal Processing Symposium** (SPSympo) 2021, 21-23 September 2021, Lodz, Poland, with the contribution:

A. Marino, A. Aubry, A. De Maio and P. Braca, "3D Localization for Multiplatform Radar Networks with Deployable Nodes," 2021 Signal Processing Symposium (SPSympo), 2021.